Exploring high precision VLBI astrometry of hydroxyl and water masers to study late stellar evolution

PhD Thesis (Astronomy)

by Gabor Orosz
Graduate School of Science and Engineering
Kagoshima University, Japan

Supervised by Hiroshi Imai, PhD, Associate Professor
Department of Physics and Astronomy, Kagoshima University, Japan

Kagoshima University
2017

Abstract

This PhD thesis has two main topics: technical studies of VLBI astrometry at L-band and astrometric measurements of OH and H_2O masers to study late stellar evolution. The technical studies focus on mitigating spatial systematic errors caused by the ionosphere, the bane of VLBI measurements at low-frequencies, which hinder the astrometric applicability of one of the best stellar tracers, 1.6 GHz OH masers. We need to figure out how to do precise astrometry of OH masers; doing this would make it possible to measure accurate distances to evolved stars with heavy dust shells and high mass loss rates, the lack of which impeded on the better understanding of stellar evolution for far too long.

This work provides an overview of relative VLBI astrometry from the point of view of error analysis, then goes on to demonstrate new calibration and analysis methods to achieve high precision astrometry at L-band. Some OH maser parallaxes are also measured in the process, but their application to study stellar evolution is ongoing. Additionally, the first results related to H_2O masers in the fast outflows of water fountain stars are also presented, with a focus on better understanding the evolutionary process between evolved stars and planetary nebulae.

Preface

I am turning 30 in 115 days, which means that I can start the next decade of my life as an astronomer. Until now, I could not call myself one without feeling guilty inside – although in the last few years, since I moved to Kagoshima, I started doing so when someone asked me about my work. I always said "I am a radio astronomer and I study how old stars live and die", in my broken Japanese usually. Although a PhD is just a piece of paper, not something that defines me, it will be a piece of paper that I can use to get people pay me to do more astronomy – and I think that will make me a professional astronomer.

Twelve years ago I was thinking about becoming an archeologist, something I wanted to be for the most part of my teenage years. I liked history, not physics. I played Age of Empires II with my friends and had debates about how Hannibal messed up the Second Punic War – he should have first taken Corsica with the elephants! But I did not end up as an archeologist, and I graduated first as a civil engineer (I really wanted to become a roller coasters designer at one point), then as a geodesist. And now I am an astronomer. Now to think of it, I certainly reached a point where I cannot really call myself an engineer any longer (even though I have a paper that says I can), but can call myself an astronomer (even though I technically do not have any paper yet that says I can). Papers. When I passed my defense, my friend told me that now I can let myself become stupider, as I do not have to prove to anyone anymore that I know astronomy. We will see, maybe this astronomy business will prove to be temporary, too. I have been really into dolphin linguistics recently.

I was raised in a researcher family. My mom, my dad, my brother, all doctors of various sorts. So perhaps that influenced me to become a researcher, it was certainly the norm when I was growing up. Outside of my family, the first influence towards this profession came from Lajos Völgyesi, my teacher in geophysics at University. I then later met Sándor Frey, who nudged me through my first conference in Porto and my first research article to Astronomy & Astrophysics. Getting that paper accepted was such a rush, and I was already in Japan at that point. In Japan I then met Hiroshi Imai, my supervisor and mentor for the coming years who put much more faith in me than I deserved, and my training as a VLBI astrometrist began at Kagoshima University. During my PhD years I had three additional friends and mentors, who made me the astronomer I am today: Ross Burns, Richard Dodson and Maria Rioja. To all of you, my friends, colleagues, family, my gratitude is eternal.

I was fortunate enough to be able to travel a lot during my PhD years, and meet lots of people who influenced or helped me in some way. I could visit and experience wonderful places, the snow covered peaks of Yatsugatake in Nagano, the blistering heat of Perth, or the amazing bibimbap place in Jeonju, just to name a few. Or having a hot dog atop the Pyramid of the Sun in Teotihuacán with Daniel Tafoya, also a good friend and colleague who invited me over to

Mexico for work, while staying with his family for a month. Anyhow, the point is that I had a truly amazing experience over the years in Kagoshima, one that I will miss greatly.

Kagoshima. When I got the MEXT scholarship from the Japanese government – which provided the financial stability that made it possible to never have to think about money while here – and went to the Japanese Embassy in Budapest for the following reception, everyone working there was from the Tokyo area. It turned out that none of them had ever been to Kagoshima before – or as a matter of fact to Kyushu, besides Fukuoka – and the only thing they could tell me about the place was that there is an active volcano, lots of onsens and shochu made from sweet potatoes. All turned out to be true, all turned out to be defining experiences. I will miss Kagoshima amazingly, wearing my ash-storm goggles while cycling, wandering around in the never ending heat and rain of summer searching for a new ramenya, sitting in the cold pool of Nakamura onsen as my heart slows down making ripples on the surface, having a nice talk with Nakagawa-san while looking at Sakurajima, going to the lively parties of the Handa family, hanging out with Michael or having beer and ice cream with Ross at Joyfull. All this and much more. This has been my second home, I hope I can be back one day.

The important message is that much more happened in these last four years than the PhD thesis you are holding right now. I have learnt how to live and enjoy my life in a new place surrounded by unknowns, and I made many new friends in the process. I have also learnt how to conduct independent research and how to collaborate with others in big international teams, skills that were the most difficult to acquire. As for my PhD research presented in this thesis: I can only hope that some of the work I have done here will prove to be valuable to humanity at some point in the future. At least the process was valuable to me.

To everyone who believed in me, who helped me, who got me funding, who pushed me constantly forward, who visited me here in this remote southern Japanese space station:

My thesis is dedicated to all of you.

Gabor Orosz
Happiness Court, Toso, Kagoshima
on the 20th of February, 2017

Declaration

I hereby declare that the work in this thesis was carried out in accordance with the regulations of Kagoshima University. The work is original except where indicated by references in the text. No part of the thesis has been submitted for any other degree or presented to any other university for examination in Japan or abroad.

Sections on the technical aspects of low-frequency astrometry in Chapters 3.2 and 4.1 are largely based on my publications of Rioja et al. (2017) and Orosz et al. (2017b) respectively, while the publication of the results related to stellar evolution and water fountain stars in Chapters 4.2 and 5 is still pending. I gratefully acknowledge the discussions and analyses provided by my colleagues and collaborators.

The research presented in this thesis was conducted from 2013 to 2017 under the main supervision of Prof. Hiroshi Imai at Kagoshima University.

Gabor Orosz
Kagoshima, 2017

Contents

Glossary

2MASS	Two Micron All-Sky Survey, a ground-based infrared astronomical survey
AGB	asymptotic giant branch star
AIPS	Astronomical Image Processing System
AKARI	a Japanese infrared astronomy satellite
ARIS	Astronomical Radio Interferometer Simulator, a VLBI data simulator
ASKAP	Australian SKA Pathfinder
ATCA	Australia Telescope Compact Array
BeSSeL	the Bar and Spiral Structure Legacy survey, a VLBA large project
CH_3OH	methanol molecule or methyl alcohol
COLIBRI	a code for computing the evolution of stars along the TP-AGB phase
CSE	circumstellar envelope
DiFX	a software correlator for VLBI
DUSTY	a radiation transfer code designed for modeling dusty regions
EOP	Earth Orientation Parameters
EVN	European VLBI Network
FFR	fractional flux recovery
GBT	Robert C. Byrd Green Bank Telescope, WV, USA
GPS	Global Positioning System
H_2O	water molecule
HBB	hot-bottom burning
HMSFR	high-mass star-forming region
ICRF	International Celestial Reference Frame
IRAS	Infrared Astronomical Satellite, joint project of USA, UK and the Netherlands
IVS	International VLBI Service for Geodesy and Astrometry
KaVA	KVN and VERA Array
KVN	Korean VLBI Network
LMC	Large Magellanic Cloud

LPV	long period variable star
LSR	local standard of rest
mas	milliarcsecond (μas: microarcsecond or 10^{-3} mas)
MERLIN	Multi-Element Remotely Linked Interferometer, a British interferometer array
MFPR	multifrequency phase referencing
MV	MultiView, a multi-calibrator phase referencing technique
MWG	Milky Way galaxy
NASA	National Aeronautics and Space Administration
NOAA	National Oceanic and Atmospheric Administration
NRAO	National Radio Astronomy Observatory
NRO	Nobeyama Radio Observatory, Japan
NRT	Nançay Radio Telescope
OH	hydroxyl radical, the neutral form of the hydroxide ion
OH/IR	OH maser emitting AGB star with an optically thick CSE
OH138	OH138.0+7.2, one of the OH/IR star targets with a period of 1410 days
PLR	period–luminosity relation
PN	planetary nebula
PR	phase referencing
QSO	quasi–stellar object or quasar
RSG	red supergiant
SED	spectral energy distribution
SFPR	source/frequency phase referencing
SFXC	a software correlator for VLBI
SiO	silicon monoxide
SKA	Square Kilometre Array
SNR	signal-to-noise ratio
SR	semiregular variable star
TEC	Total Electron Content, measured in TEC units where 1 TECU = 10^{16} electrons m^{-2}
TP-AGB	thermally-pulsing asymptotic giant branch star (AGB) star
VERA	VLBI Exploration of Radio Astrometry, a Japanese VLBI array
VLA	Karl G. Jansky Very Large Array
VLBA	Very Long Baseline Array, USA
VLBI	very long baseline interferometry
VSOP	VLBI Space Observatory Programme, a Japanese VLBI satellite
VTEC	Vertical TEC, measured towards the zenith
WF	water fountain star
WISE	Wide-field Infrared Survey Explorer, an American infrared astronomy satellite
WSRT	Westerbork Synthesis Radio Telescope, a Dutch interferometer array

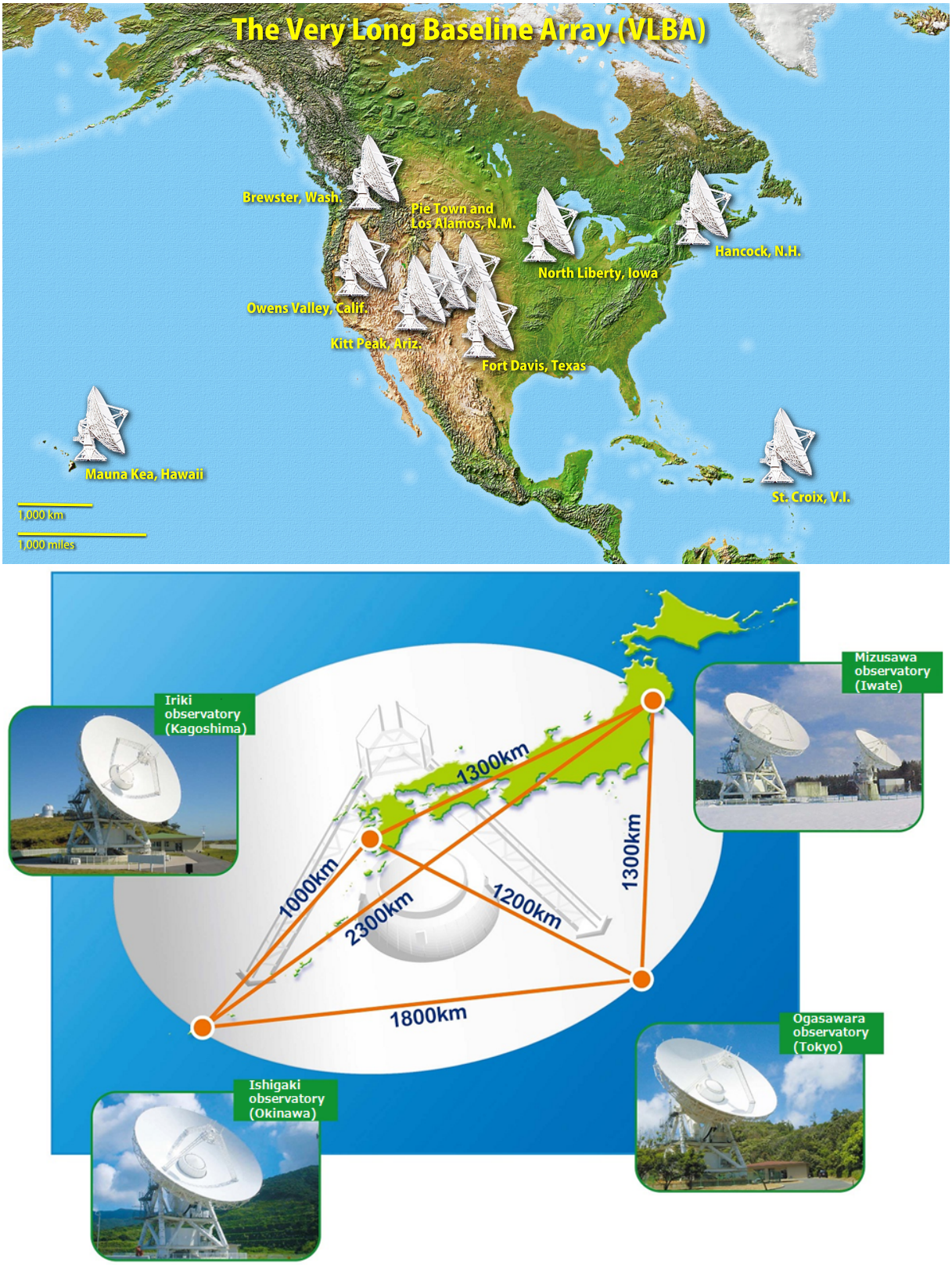

Figure 1. *Top:* The VLBA is a system of ten radio telescopes spanning ~9000 km at the longest baseline. Each identical telescope has a diameter of 25 m and has a frequency coverage of 1.2–96 GHz. Credit: NASA's Goddard Space Flight Center
Bottom: VERA is a system of four radio telescopes spanning ~2300 km at the longest baseline. Each identical telescope has a diameter of 20 m and a unique dual-beam (and dual-frequency) setup, that enables the simultaneous observation of sources up to 2.2° apart (soon simultaneously at 22 and 43 GHz). Credit: National Astronomical Observatory of Japan

List of Figures

List of Tables

1 | Introduction

The late stages in the evolution of stars still hold some interesting questions to answer: is there an evolutionary connection between AGB stars with different pulsation periods, what is the role of metallicity, mass loss, or how do AGB stars evolve into and shape PNe? Astrometry using different maser transitions can help answer these questions. It can provide accurate distances to evolved stars thus helping to get accurate stellar parameters that can put constraints on various models. It is also possible to measure structures and internal motions in the CSE traced by masers, for example by mapping the shocked boundaries and 3D motions of jets in water fountains to better understand how such jets were launched or how they shape their environment.

Whatever might be the specific science case, in order for VLBI astrometry to help answer the questions above, we need to make sure that our measurements are both accurate and precise. Stellar environments, using masers at available VLBI frequencies, can be traced by the 43 GHz SiO lines, the 22 GHz H_2O line and the 1.6 GHz OH lines. The present work focuses mainly on the 1612 MHz OH maser transition, as its use for astrometric studies has been hindered so far due to the difficulty of calibrating astrometric data at such low frequencies. 1612 MHz OH masers also hold great potential as one of the strongest and most widespread stellar tracers, with many thousands of known sources in our Galaxy alone.

The problem so far has been that at low frequencies, astrometry is increasingly dominated by dispersive ionospheric errors, and present calibration methods have had difficulties dealing with the spatial structures of this propagation medium that cause direction-dependent systematic errors in astrometric measurements. This puts a serious limitations on the accuracy on low frequency astrometry and makes OH maser astrometry difficult and unreliable. Therefore, the biggest aim of this PhD thesis is to demonstrate a new VLBI astrometric technique that can better mitigate direction-dependent systematic errors than present techniques, using L-band measurements of continuum and OH maser sources. The technique is called MultiView and it is essentially a multi-calibrator phase referencing solution, using the observed visibility phases to model the ionospheric phase screen around the target source.

Although not novel, another calibration technique called in-beam phase referencing is also explored. In-beam phase referencing relies on finding a reference source in the beam of the target source; the proximity and simultaneous observation of the two sources leads to improved precision in astrometry. As it is the most widespread way to conduct astrometry at low frequencies, I investigate its limits in accuracy and ability to deal with the systematic error residuals using VLBI measurements of 1612 MHz OH masers. In the process, I also try to conduct annual parallax measurements using OH masers, the first attempt in the last 10 years due to the described challenges and intrinsically lower resolution at 1.6 GHz.

Finally, I also show some early results from 22 GHz H_2O maser measurements around water fountain stars. The aim of these observations is to derive the distance to WF sources and measure the characteristics of their jets. VLBI is the only technique that has the angular resolution and astrometric accuracy to directly trace the motion of WF outflows using H_2O masers in the jet-shocked regions, or to measure their physical structure and changes in their morphology. WFs are rare, with only about a dozen known sources, and their astrometric measurements (especially annual parallax and absolute proper motion studies) are even rarer. It is therefore essential to conduct more of these observations if we ever hope to understand WF evolution.

After introducing the theses of my PhD research, Chapter 2 will introduce the concept of masers, which are the main targets of the VLBI astrometric measurements as tracers of stellar environments. We briefly describe the key properties of stellar masers that determine their observational properties, i.e. their pumping, amplification and beaming processes. Chapter 3 introduces the concepts in VLBI astrometry, with a focus on error analysis. All antenna-based and baseline-based phase-delay errors are dealt with in detail, through a discussion on basic and advanced phase referencing techniques. The second half of the chapter introduces and demonstrates MultiView, a new astrometric calibration technique for the ionosphere dominated VLBI frequencies.

Chapter 4 presents results from annual parallax measurements using 1612 MHz OH masers, utilizing in-beam astrometry and a new method for detecting and flagging systematic errors. Some possible scientific uses of the measured OH/IR distances are also explored, such as the calibration of phase-lag distance measurements, understanding the period–luminosity relations in the TP-AGB phase, and using evolved stars as new probes of MWG dynamics. Chapter 5 introduces water fountain sources and their importance in understanding post-AGB stellar evolution and PNe shaping. The first astrometric results are presented from two WFs, including the measurement of an annual parallax less than 0.1 mas, and the spatial and kinematic properties of their molecular jets. In Chapters 4–5, an emphasis is based on understanding the maser structure of both OH and H_2O masers, as proper motion and annual parallax measurements can be seriously hampered by the turbulent and ambiguous motions inside maser clouds. Chapter 6 gives a short summary of the general results and an outlook to future projects continuing this work. See the theses of this dissertation, a list of the specific claims and results of my PhD research, on the next page.

Theses of my PhD research

1. The first successful demonstration of MultiView on real L-band continuum and spectral line VLBI data, which is a direction-dependent calibration technique that uses multiple calibrators to model the 2D phase screen around the target and solve for the residual propagation errors directly in the target line-of-sight. We provide clear evidence on the superiority of this technique compared to traditional methods and achieve complete ionospheric mitigation in our astrometry (see Sect. 3.2). Published in Rioja et al. (2017).

2. The introduction of a new analysis technique to detect antenna-based systematic errors in VLBI measurements. We demonstrate this technique on both continuum and OH maser observations at 1.6 GHz and show the achievable increase in accuracy by flagging out data that was identified to be contaminated by systematic errors (see Sect. 3.2 and 4.1). Published in Orosz et al. (2017a,b).

3. We derive the first parallax to an OH/IR star (OH 138.0+7.2) using 1612 MHz OH masers, which is also presently the smallest and most accurate OH maser parallax. Our results show that OH maser parallax measurements are possible on a sub-mas scale with a precision of $\sim$100μas using in-beam phase referencing and our new systematic error flagging method (see Sect. 4.1). Published in Orosz et al. (2017b).

4. We derive the annual parallax of the water fountain star IRAS 18113–2503, using H_2O masers in a >200 km s^{-1} outflow, which is the smallest stellar parallax yet measured at $\lesssim$100 μas (see Sect. 5.1). Publication still pending.

5. We derive the first VLBI maser maps of the water fountain star IRAS 18043–2116 and measure the internal motions of its outflows. We find our measurements to be in general agreement with a jet-driven ballistic bow shock model, indicating that our masers trace shocked material on the boundary between the high-velocity WF jet and the slowly moving circumstellar shell (see Sect. 5.2). Publication still pending.

2 | Stellar masers

In this chapter we will briefly discuss what masers are, what species are found around AGB and post-AGB stars and what key observational properties they have for astrometry. What makes masers ideal for astrometry is that they are extremely bright, tightly focused (i.e, the emission is compact), coherent and have very narrow frequency profiles, while tracing very specific physical environments. Furthermore, masers are found at frequencies readily observable by large VLBI arrays and are associated with evolutionary phases, where most of the action happens in stellar evolution: when the stars are born and when they are dying. In the following, I will introduce how these maser clouds come to be, where they live around evolved stars, and what to actually watch out for when doing VLBI maser astrometry. However, I will not go into the specific physical details of the various maser species; instead please refer to Elitzur (1992) for a very straightforward introduction on maser physics and to Gray (2012) for the most complete picture we have of masers today. This thesis focuses mainly on ground state OH masers, for which a very good and detailed discussion can be found in Wright (2001) that discusses not just the physical, but also the chemical background of masers.[1] A detailed explanation of AGB stellar masers can also be found in Amiri (2011), concentrating more on their observational aspects as probes of magnetic fields.[2]

2.1 Excitation mechanisms

Astrophysical masers are clouds of molecular gas in a special physical state called population inversion, meaning that there are more molecules in a higher energy level than in a lower energy level. It is called an "inverted" state, because molecules in our "normal" surroundings are more commonly found in thermal equilibrium, where it is impossible to have a higher energy level more populated than a lower one. In principle, the population exchange between any two energy levels of any system is governed by collisional and radiative processes (Elitzur, 1992). Radiative processes can mean spontaneous decays from the upper to the lower energy level, or absorption of some external radiation (a photon with a frequency matching the energy separation of the two levels) and the consequent excitation from a lower to an upper energy level. The opposite can also happen, i.e. a downward (instead of upward) transition caused by an incoming photon with the matching frequency. This sudden downward transition causes the emission of another photon whose properties are identical to the initial seed photon, due to the conservation of energy and momentum. Now here comes the essential part for a maser: as stimulated emission increases the number of photons in a radiation field, and because in an inverted population there

[1] Available online at: http://www.star.bris.ac.uk/mark/

[2] Available online at: https://openaccess.leidenuniv.nl/handle/1887/17981

are more molecules in the upper level than in the lower level, the rate of the stimulated emission will exceed absorption and the system starts amplifying the propagating radiation exponentially.

At this point we have an unsaturated maser, meaning that the radiation grows exponentially along the length of the maser cloud. However, this exponential growth of the intensity can only continue up to a certain extent, and after a point the maser's built in quenching mechanism kicks in. Since the maser effect itself removes molecules from the upper level, the population inversion decreases once the intensity of maser radiation becomes so great as to dominate the population exchange between the maser levels. The intensity reaches a limit and the maser is said to saturate. In a saturated maser the gain is no longer exponential; the intensity growth is linear with distance and depends heavily on the input energy that produced the inverted population in the first place, the so called *pumping* process. The maser intensity is highest during saturated operation because every pumping event produces a maser photon with the maximal intrinsic efficiency allowed by the pump (Elitzur, 1992).

Pumping is the process that forms and maintains inverted populations in molecular clouds. It is an input of energy that can come from either collisional or radiative processes or both. For example, 22 GHz H_2O masers are pumped collisionally and as such can be found in shocked regions and are highly variable, but 1612 MHz OH masers on the other hand are pumped radiatively by the host AGB star and as a result are found in a stable shell where the density and temperature is just right and there is a continuos input of energy. Then there are 43 GHz SiO masers, living so close to the AGB star that they get strong radiation but also get caught up in the stellar pulsations: the result is a complicated mixture of collisional and radiative processes combined.

2.2 Tracers of evolved stellar environments

Astrophysical masers are big and surprisingly rarefied, with sizes of around the Sun with, e.g., $\sim 10^5$ molecules per cubic meter for OH masers, that would be considered a pretty good vacuum under laboratory conditions (Gray, 2012). As the density of these clouds are so low, once thermal equilibrium is violated, population inversion is a priori almost as likely as its reverse; making many astrophysical environments capable to produce the maser effect relatively easily (Elitzur, 1992). Due to the low density, the linear size of the maser cloud has to be around at least stellar sizes to produce the observed gains in a single path. Also, masers are easily excited at such low VLBI frequencies, because of their internal structure of allowed states and energy levels. The allowed energy levels in maser transitions are determined by the shapes of arrangement of the electrons in the molecules, and by the internal motions of the molecules, i.e. their patterns of rotations and vibrations. Rotational transitions require very low energy inputs, meaning that it is easy to pump them and can produce many different lines with only small differences in energy. This makes it the dominant transition type for masers at VLBI frequencies and explains why masers are readily seen in the low energy microwave regime of the electromagnetic spectrum.

The circumstellar envelope of evolved stars can be either oxygen-rich (M-type star), carbon-rich (C-type star), or somewhere in between (S-type star). Masers at VLBI frequencies are only found in O-rich CSEs, so I'm going to concentrate on them. As all the carbon is tied up in

CO, the observed stellar maser molecules – SiO, H_2O and OH – contain oxygen atoms but not carbon. They trace various parts of the CSE, with different excitation and amplification mechanisms (see Sect. 2.1 and Fig. 2.1). From an astrometric point of view, all three maser species are suitable for measuring stellar distances (see Nakagawa et al., 2016, and references therein). However, by far the most common and persistent of these masers are stellar OH masers, with thousands of known sources in the MWG (Engels & Bunzel, 2015; Qiao et al., 2016). They are also more stable than SiO or H_2O masers, as they are in the calmer regions of the CSE and are pumped radiatively. The only problem is that their transition is at 1.6 GHz, which makes the astrometric observations challenging technically.

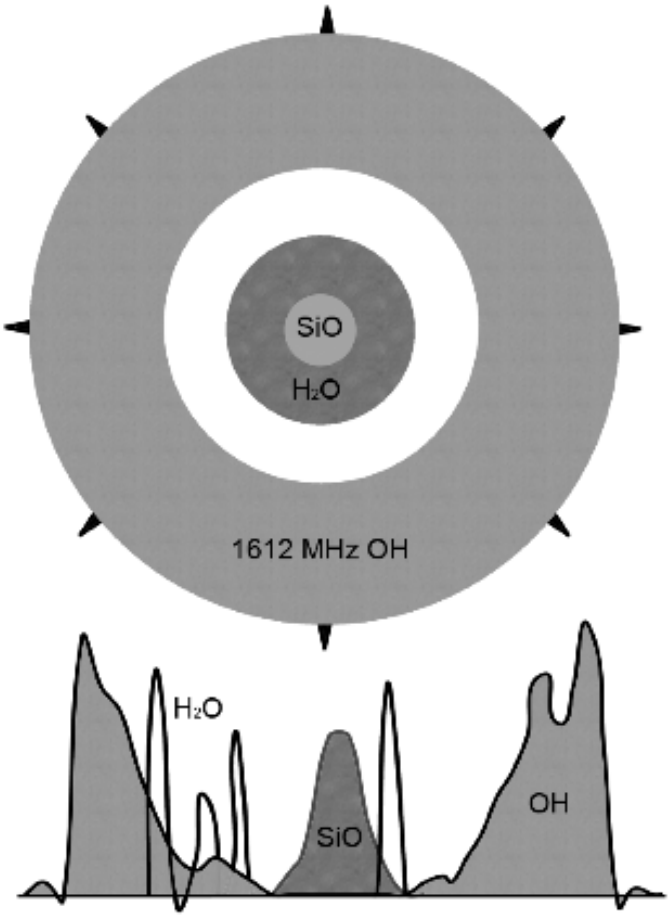

Figure 2.1. A schematic view of the CSE of a typical oxygen-rich AGB star. SiO masers occur close to the photosphere and show single-peaked profiles. H_2O masers occur at intermediate distances and exhibit irregular profiles. The 1612 MHz OH masers emit at the outer part of the CSE and display double-peaked profiles, which correspond to the front and back side of the shell. As all masers are found in shells, the observed velocity profiles depend on the preferred amplificaton and beaming properties of the individual transitions, that in turn depend on the geometry and kinematic model of the circumstellar shells (see Gray, 2012). Figure and explanation from Amiri (2011).

Out of the four OH transitions at 1.6 GHz, the 1612 MHz satellite line seems to be the most promising for astrometry. Main line 1665, 1667 MHz OH masers more commonly trace AGB stars with shorter periods, that are less obscured by their dust shell and are usually Mira variables. However, these stars are well studied and many times observable in infrared, too. On the

other hand, 1612 MHz masers are found in different regions and preferentially trace LPV AGBs, also called OH/IR stars. These stars are many times completely obscured by their heavy dust shell due to high mass loss rates, and are nearing their end on the TP-AGB phase. The distance and proper motion of these stars can only be readily measured using 1612 MHz OH masers.

The other maser species used for astrometry in the thesis is the collisionally pumped 22 GHz H_2O maser, found usually in shocked and turbulent regions. This makes them consistent tracers of WF jets, as they are often found in regions of shocked gas, such as the bow shocks of jets and outflows. Using them we can trace surfaces in the jets, gaining some insight into their morphology and motion. H_2O masers are also good indicators of ejection events in WFs as they are sensitive to passing shock waves, and could be used to study the mass loss of these stars.

2.3 Observational properties

Maser transitions are defined by their *pumping, amplification* and *beaming* mechanisms. Pumping processes determine where masers occur, e.g. close to the photosphere, further away, in circumstellar shells or molecular outflows. Amplification and beaming on the other hand are related to the geometric and kinematic model of the maser clouds and regions, and determine how the maser looks like when observed with a VLBI array. For example turbulent motions in a maser cloud, whether the cloud is spherical or flattened by shocks (Richards, 2012), or the level of saturation all influence the appearance of the maser spots. The kinematic property of their surrounding region also influences whether the masers are preferentially amplified radially or tangentially, and it alters the observed geometric distribution and strengths of the masers due to the differing velocity coherence of the maser paths.

Comparing the SiO and 1612 MHz OH masers provides the clearest example: although both maser species are distributed in a clumpy shell, SiO masers a preferentially seen in ring-like structures around the systemic velocity, whereas 1612 MHz OH masers have double-peaked velocity profiles and appear at the red- and blueshifted caps of the maser shell (see Fig. 2.2). This difference in the apparent distributions is because the SiO region is turbulent and thus amplifies tangentially (as the largest velocity coherence will be where the shell appears the thickest from our line-of-sight), whereas the 1612 MHz OH region expands radially at a constant velocity and thus amplifies radially (as the velocity coherence will be large at the caps where the shell is approaching or receding our line-of-sight, but it will be small at the systemic velocities where the shell moves perpendicular to us). This also means that there are masers for both SiO and OH at other velocities outside their preferentially amplified regions, but their emission will be much weaker due to the decreased velocity coherence.

Moving onto H_2O masers, they are usually unsaturated and pumped by shocks, while 1612 MHz masers are saturated and pumped by infrared photons. As such, some of their VLBI observational properties differ. The gain of an unsaturated H_2O maser will be very sensitive to small path length differences and the image of the maser cloud will be distorted by exponential amplification. This is due to beaming and in practice it means that the maser spots observed with VLBI will be smaller than the actual physical maser clouds. However, as maser clouds are extended in velocity as well, by detecting the same maser cloud in different channels, it is possible to get some idea about the cloud's true shape and extent. For example, in the calm regions of

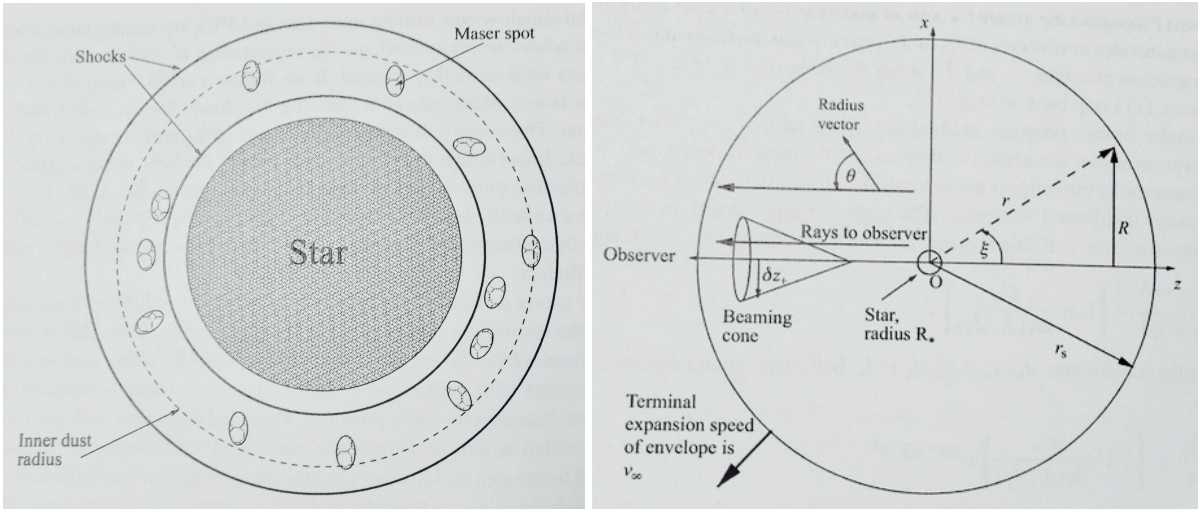

Figure 2.2. A schematic view of the SiO (left) and 1612 MHz OH (right) maser regions around an AGB star, showing the geometry and the important characteristics of the shells. The SiO shell is in the innermost zone of the CSE, while the 1612 MHz OH shell is at the outermost edge. The SiO figure shows a sky plane view, while the observer on the OH figure is to the left. The two figures are on different scales (see more explanation in main text and in Gray, 2012). Figures are from Sect. 3.7 and 6.2 of Gray (2012).

WF stars H_2O maser spots from the same maser cloud cluster around the same location roughly on the level of the VLBI resolution; however in the fast outflows they tend to elongate, i.e. the maser spots in the adjacent velocity channels spread out in a line (see e.g. Imai et al., 2002; Richards et al., 2012). Also, as the maser radiation depends exponentially on both the population inversion and the path length, any variation in these parameters will be reflected exponentially, making the H_2O maser variability much more rapid than the underlying physical processes would be (Gray, 2012).

For maser emission, the geometry and internal velocity gradients of the maser clouds are important factors. In reality, the masers we see might not be single clouds, but several clouds moving in a turbulent motion. This can cause complex patterns in the maser emission; an important factor for astrometry. Also, the intensity of these masers follow the underlying changes in the stellar pulsation (van Langevelde et al., 1990). Also, an important aspect for OH masers is their large size and, as a result, are often not detected on the longer VLBI baselines.

3 | VLBI techniques for astrometry

This chapter introduces VLBI astrometry and investigates the possible systematic errors that can affect the final measurements, errors related to the observed radio sources, the propagation errors caused be the atmosphere, positional and instrumental errors tied to the antennas themselves. I will introduce advanced techniques to deal with these effects, with a special focus on spectral line astrometric measurements. In the second part of the chapter, a new technique (MultiView) is introduced and demonstrated for the first time on real VLBI measurements, which is designed to correct for spatial systematic ionospheric propagation effects. As a caveat, the present chapter is not meant to give a detailed overview on every aspect of VLBI data calibration, such as correlation, mapping or very specific techniques applicable to only certain types of VLBI arrays. For a straightforward and very intuitive introduction to VLBI basics, please have a look at Chapter 3 of Burns (2016).[1] The NRAO's online guidebook is another very good place to start.[2]

3.1 An overview of relative radio astrometry

3.1.1 Measuring time: the basics of VLBI astrometry

As we have seen in the previous chapter, we can use maser sources to study the surroundings of stars, gain insight into their evolution or trace their motion in space. As maser sources are more or less stable and compact, they provide an excellent marker for astrometric measurements. Measuring the motion of masers also allows us to measure the underlying motion of their environments, in our case the proper motion and parallax of the host star. This in itself is nothing new: for countless centuries the primary focus of astronomy was astrometry, and slow but steady progress was made from the mid 1800s in measuring stellar parallaxes using optical measurements. Due to the errors introduced by the constantly changing water vapor in the atmosphere, astrometric uncertainties of ground based observations were only around mas level, which limited measuring parallaxes to the solar neighborhood (Kovalevsky & Seidelmann, 2004). This limitation was lifted with space-based optical telescopes, and e.g. the state of the art Gaia survey is aimed for sub-mas level astrometric accuracy (see Gaia DR1, Lindegren et al., 2016), with measured optical parallaxes on a $\sim 10 \mu$as level (once the mission ends around 2020). Even more impressive is that the Gaia astrometric mission does this by continuously scanning the whole sky and monitoring up to a billion sources in doing so, making it a truly unique astrometric system.

[1] Available online at the Kagoshima University archive: http://hdl.handle.net/10232/26940

[2] J.J. Condon & S.M. Ransom, Essential Radio Astronomy: http://www.cv.nrao.edu/course/astr534/ERA_old.shtml

The astrometric precision of a telescope is limited to some fraction of its diffraction limit, i.e. angular resolution of $\theta_d \approx \lambda/D$, where λ is the observing wavelength and D is the antenna diameter. Observing wavelengths in spectral line radio astrometry are usually in the ∼1–10 cm range, about 10^{-5} times longer than optical wavelengths, so the antenna diameter would have to be increased by 5 orders of magnitude to achieve the same astrometric precision. In practice this would mean antenna diameters hundreds of kilometers across, something that is technically unfeasible. The costs of antennas roughly scale as $\sim D^{2.7}$ (Thompson et al., 2004), however pointing accuracy, surface accuracy, gravity loading or wind loading can impose even more serious limitations to size (Wilson et al., 2009; Cheng, 2009). As a result, the largest fully steerable radio antennas top out at around D≈100 m. Thus the resolution of the largest single radio telescopes, and as a result their astrometric precision, are no better than that of our eyes. Clearly, a different technique is needed to achieve the sub-mas level astrometric precision presented throughout this thesis.

The solution lies in very long baseline interferometry, or VLBI for short, where the resolution of the observing system is greatly enhanced by using accurately time tagged observations of several antennas thousands of kilometers apart. By combining and correlating (multiplying and averaging) the recorded individual signals, a VLBI array can mimic a telescope in size that would be as large as the geographical extent of the individual telescopes in the array, thus achieving sub-mas level angular resolution and astrometric precision approaching the 1 μas level. This makes VLBI the most precise tool for astrometry, although present systems are limited to small (sub-)degree-scale field-of-views (e.g. the VLBA[3] or the VERA array that were used for my PhD research), and fast "Gaia-like" astrometric observations covering the whole visible sky will only be available with next-generation systems, such as the SKA (Paragi et al., 2015).

As opposed to optical observations where the derived astrometry is based on direct angular observations, the fundamental observable of a VLBI array is the difference in the arrival time of wavefronts between antennas (Kaplan, 1998), due to the finite propagation speed of the incoming electro-magnetic waves (the speed of light c). As a first approximation, this τ arrival time between antennas is determined by the location of the antennas relative to the line-of-sight of the source that is perpendicular to the incoming flat wavefront as

$$\tau_{\mathrm{g}} = \frac{\vec{s} \cdot \vec{B}}{c} \ , \tag{3.1}$$

where τ_{g} is called the geometric delay, with the relative positions of the VLBI array antennas to the observed source encoded in the $\vec{s}$ source unit vector and $\vec{B}$ baseline vector (Fig. 3.1). For celestial bodies the wavefront of the incoming radiation is approximated as a plane, i.e. the emitting source is considered to be at an infinite distance. Note however that in reality wavefronts are curved; e.g. on global baselines the additional timing errors from this approximation can reach tens of picoseconds for sources in the MWG (Sekido & Fukushima, 2006), although the effect of the curvature can usually be neglected in delay models used for far-field astrometric measurements of celestial bodies as other residual effects dominate the final error budget.

The astrometric error, i.e. the uncertainty in the source position, can be derived by rearranging

[3] A sidenote on costs: the VLBA, having ten telescopes with diameters of 25 m spread across the US cost ∼$100 million to construct, the same as the largest fully steerable telescope, the GBT, with a diameter of ∼100 m. Annual operating costs run around ∼$10 million for both systems. This means that for the same cost, many smaller antennas can have better sensitivity – for certain spatial scales – and resolution than one large antenna.

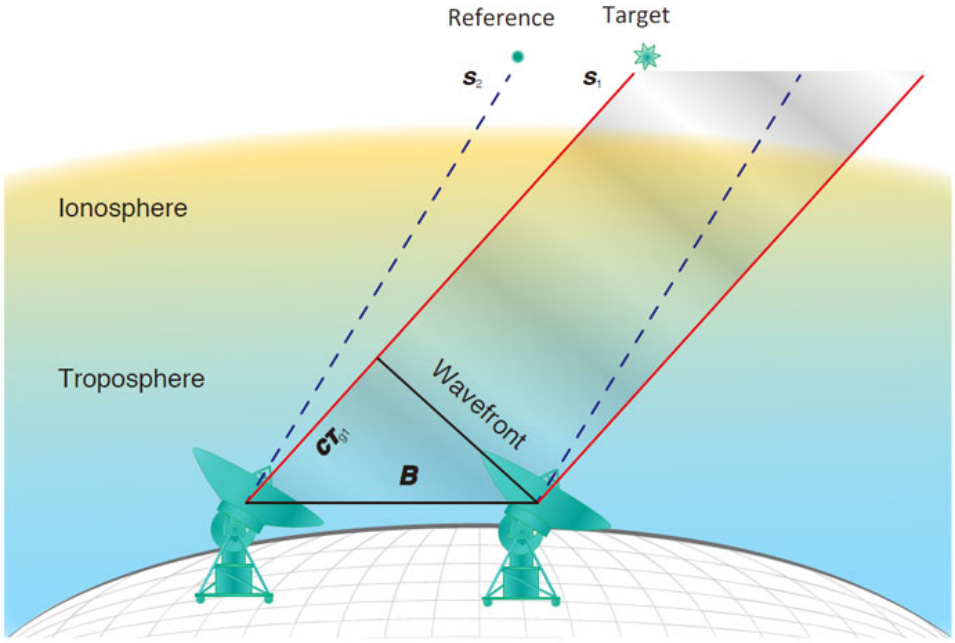

Figure 3.1. Schematic view of delay measurements of a VLBI array from Reid & Honma (2014). The $\vec{s}$ source unit vector and $\vec{B}$ baseline vector are indicated by lines, whereas the τ_g delay is represented in $c\tau_g$ path length. A target source is shown with a reference source, the basic configuration of phase referencing observations to do relative astrometry by canceling out most errors in the delay measurements with the (near-)simultaneous observations of the two sources. The main focus of my thesis is how to deal with the dominant residual errors from the atmosphere when high-precision astrometry is desired. Only two stations are shown for simplicity, but the same principles apply for larger arrays; all VLBI observables can always be broken down into a series of two-antenna delay measurements for any given time.

(3.1) to the $\vec{s}$ source vector, to get

$$\Delta s \approx \frac{c\Delta\tau}{|B|} \quad , \tag{3.2}$$

where Δs is the astrometric error, $\Delta\tau$ is the error in the delay measurement, and the errors in the B baseline length can also be represented by errors in the delay. Thus we can see that the astrometric error of any given VLBI measurement boils down to the errors in our timing measurements, and the role of astrometric data reduction is to somehow compensate for these errors. Our final goal is to derive the right ascension and declination of the source, which can be done by multiple delay measurements using different baseline orientations – achieved by having more antennas and/or using the rotation of the Earth. Note that $\Delta s \propto |B|^{-1}$, thus we successfully worked around the problem of having to have antennas the size of continents for sub-mas resolution; we can instead substitute that with some precise timing observations and multiple small antennas set thousands of kilometers apart. For example, a typical delay error of $\Delta\tau \approx 0.1$ ns on a 6000 km baseline would result in an astrometric error of $\Delta s \approx 1$ mas. As baselines go up to more than 10000 km, absolute astrometric uncertainties on a sub-mas level are routinely attainable, i.e. astrometry based on measuring the delays only on a single source using wide bands and accurate models at the correlator to determine and minimize delay errors. Such absolute delay measurements are used mainly to determine the positions of quasars for radio reference frames (see e.g. ICRF2, Fey et al., 2015), with the most accurate positions being as good as ~0.1 mas thanks to repeated observations by monitoring the same bright sources for decades.

However, in order to measure stellar maser parallaxes usually in the $\lesssim 0.1 - 1$ mas range for sources in the MWG, we have to achieve astrometric precisions of $\sim 0.01 - 0.1$ mas in a single observing session of a few hours, many times on weak and highly variable sources. Fortunately, when measuring maser proper motions and parallaxes, we are only interested in the relative changes in their positions between epochs and not in the absolute motion in a reference frame. We can therefore use relative or differential astrometric techniques, i.e. measuring positions with respect to nearby reference source(s) with well known position(s), to cancel out or mitigate a large number or error residuals that would otherwise dilute the precision of our astrometry (Reid & Honma, 2014).

To understand the principles behind differential astrometric measurements, let us represent the measured τ delay (containing measurement errors) as the sum of the following components:

$$\tau = \tau_{\rm g} + \Delta\tau = \tau_{\rm g} + \Delta\tau_{\rm struc} + \Delta\tau_{\rm tropo} + \Delta\tau_{\rm iono} + \Delta\tau_{\rm bl} + \Delta\tau_{\rm inst} + \Delta\tau_{\rm therm} \ . \tag{3.3}$$

We are interested in determining a term related to $\tau_{\rm g}$, as that carries the information on the source position. All additional terms are error sources that contribute to the $\Delta\tau$ uncertainty in the delay measurements, and are characterized as follows:

$\Delta\tau_{\rm struc}$ **Source structure error.** An unresolved, point-like source does not affect the delay measurements as the measured delays can be associated with a single $\vec{s}$ source vector. However when the observed source is extended, its brightness distribution on the sky can only be described by a combination of multiple point-like components each with a slightly different $\vec{s}$ source vector. These components can blend together in different ways as a function of baseline length and orientation and cause systematic shifts in the measured delays. Source structure error is a baseline-based quantity, i.e. its value depends on the $\vec{B}$ baseline vectors and cannot be tied to individual antennas.

$\Delta\tau_{\rm tropo}$ **Tropospheric error.** The air mass and water vapor content above telescopes add additional delays to radio waves passing through the troposphere. The tropospheric delay error is non-dispersive at radio frequencies and can be separated into a $\Delta\tau_{\rm dtropo}$ dynamic and a $\Delta\tau_{\rm stropo}$static component. Dynamic terms change rapidly and are caused by the turbulent motion of water vapor pockets in the lower troposphere, whereas static terms are due to the temporally stable part of the water vapor content and the actual effect of the air mass above above each observing site (see e.g. Thompson et al., 2004).

$\Delta\tau_{\rm iono}$ **Ionospheric error.** Radio waves propagating through the ionized upper layers of the atmosphere experience dispersive delays that can also be separated into a $\Delta\tau_{\rm diono}$ dynamic and a $\Delta\tau_{\rm siono}$static component. These ionospheric delay errors are related to the electron column density or TEC value of the ionospheric plasma and are mainly affected by the solar radiation and as such have a strong diurnal variation and conditions tied to the solar position and activity (see e.g. Thompson et al., 2004). Rapid TEC variations are caused by waves of various scales propagating through the plasma that can have various causes, such as gravity sound waves in the thermosphere (e.g. Bristow & Greenwald, 1997).

$\Delta\tau_{\rm bl}$ **Baseline error.** Errors in the $\vec{B}$ vector are linked to the position accuracy of the antennas and can represented as delay errors due to the path length errors they introduce. Antenna positions and the additional EOP parameters[4] are determined and constantly updated using repeated geodetic VLBI and GPS measurements and other geodetic techniques. For

[4]See for example the IVS EOP service: http://ivscc.gsfc.nasa.gov/products-data/products.html

precise astrometric VLBI measurements, antenna positions need to be known to a few millimeters. As such, when new antennas or arrays are commissioned, a few years may pass before they can be tied to other antennas with the required accuracy and start regular astrometric operations (e.g. as is the case for KaVA – the combined array of KVN and VERA – at the time of writing this thesis). Baseline delay errors are usually not dominant for terrestrial observations, but can be a challenge to calibrate for ad-hoc arrays (e.g. joint VERA + NRO 45 m observations) or space VLBI baselines due to the orbit determination error of VLBI satellites (see e.g. the VSOP missions, Porcas et al., 2000; Asaki et al., 2007).

$\Delta\tau_{\rm inst}$ **Instrumental error.** Additional delays can be caused by a multitude of sources tied to the front- and backends of VLBI stations, such as the gravity or temperature deformations of antenna structures, observing elevation, changes in the electronics, local oscillators, feeds, cable lengths, and last but not least the stability of the frequency standards controlling the VLBI station clocks. These frequency standards are usually hydrogen maser atomic oscillators stationed at each station that usually drift by ∼1 nsec per day, but this delay error can be well modeled or directly observed and removed during a VLBI session (Reid & Honma, 2014). Other instrumental errors are harder to model, but are relatively stable and can be calibrated with adequate observing setups and/or by using artificial noise sources.

$\Delta\tau_{\rm therm}$ **Thermal noise error.** The limit of precision achievable by any astrometric observation is the thermal noise error, as it is caused by the stochastic motion of the electrons in any electronic device and cannot be calibrated and removed. It is dominated by the receiver noise and is a function of the characteristics of the observing system (SEFD, bandwidth) and the observing conditions (flux density of source, duration of scan). As it is a random process, it does not cause systematic errors in the astrometry and integrating over a longer time and observing brighter sources can decrease its effect and is usually overshadowed by other components in the astrometric error budget.

To mitigate these errors, we observe our target source (whose position we are interested in) together with a reference source of known position at (nearly) the same time and almost at the same position on the sky, measuring the delays τ_1 and τ_2 for the two sources respectively (see Fig. 3.1). We then calculate the $\tau_1 - \tau_2$ difference of the measured delays to get the differential delay terms as

$$\begin{aligned}\tau_1 - \tau_2 &= \left(\tau_{\rm g,1} - \tau_{\rm g,2}\right) + \left(\Delta\tau_1 - \Delta\tau_2\right) = \\ &= \left(\tau_{\rm g,1} - \tau_{\rm g,2}\right) + \left(\Delta\tau_{\rm struc,1} - \Delta\tau_{\rm struc,2}\right) + \\ &+ \left(\Delta\tau_{\rm tropo,1} - \Delta\tau_{\rm tropo,2}\right) + \left(\Delta\tau_{\rm iono,1} - \Delta\tau_{\rm iono,2}\right) + \\ &+ \left(\Delta\tau_{\rm bl,1} - \Delta\tau_{\rm bl,2}\right) + \left(\Delta\tau_{\rm inst,1} - \Delta\tau_{\rm inst,2}\right) + \left(\Delta\tau_{\rm therm,1} - \Delta\tau_{\rm therm,2}\right) \ .\end{aligned} \tag{3.4}$$

The astrometric information is contained in the $\tau_{\rm g,1} - \tau_{\rm g,2}$ differential geometric delay of the target (1) relative to the reference (2) source, which corresponds to the relative position of the target source with respect to the reference source with the known position; hence the name *differential* or *relative* astrometry. The $\Delta\tau_1 - \Delta\tau_2$ delay error differentials can be separated into two main types: baseline-based error terms ($\Delta\tau_{\rm struc}$) and antenna-based error terms ($\Delta\tau_{\rm tropo}, \Delta\tau_{\rm iono}, \Delta\tau_{\rm bl}, \Delta\tau_{\rm inst}, \Delta\tau_{\rm therm}$); see description above for each component. As $\Delta\tau_{\rm struc}$ errors are independent between the target and reference sources and are not related to conditions

around the VLBI stations, the $\Delta\tau_{\mathrm{struc},1} - \Delta\tau_{\mathrm{struc},2}$ delay differential does not reduce the delay errors, and it can even transfer additional error terms to the target in certain cases. However, using so called "closure quantities" with a technique called hybrid mapping (e.g. Linfield, 1986), which is essentially an iterative loop of self-calibration (see Sect. **??**), imaging and deconvolution by using the baseline-based nature of the source structure contributions, we can build up a model of the reference source and estimate $\Delta\tau_{\mathrm{struc},2}$.

The rest of the errors are all antenna-based, i.e. the additional delays are somehow tied to the individual antennas and their receiver systems ($\Delta\tau_{\mathrm{bl}}, \Delta\tau_{\mathrm{inst}}, \Delta\tau_{\mathrm{therm}}$) or to their vicinity ($\Delta\tau_{\mathrm{tropo}}, \Delta\tau_{\mathrm{iono}}$), and are mostly independent between antenna sights due to the large separations between VLBI stations. This is where the power of relative astrometry becomes evident: as antenna-based delay errors originate at the antennas' locations, they are (more-or-less) similar for the line of sights of the target and reference source for small source separations, and as such can be greatly reduced by differencing them.

Based on Reid & Honma (2014) the $\Delta\tau_{\mathrm{bl}}$ baseline error, which comes from the position uncertainty of the antennas, and it can be approximated as

$$\Delta\tau_{\mathrm{bl}} = \frac{\vec{s}\cdot\Delta\vec{B}}{c} \sim \frac{|\Delta B|}{c} \quad , \tag{3.5}$$

because $\vec{s}\cdot\Delta\vec{B}$ is essentially the projection of the baseline error vector on the sky plane and is thus ≤ 1. Using the same logic, the differential baseline error will be

$$\Delta\tau_{\mathrm{bl},1} - \Delta\tau_{\mathrm{bl},2} = \frac{\left(\vec{s_1} - \vec{s_2}\right)\cdot\Delta\vec{B}}{c} \sim \theta_{\mathrm{sep}}\frac{|\Delta B|}{c} \quad , \tag{3.6}$$

where θ_{sep} is the separation angle between the two sources and as such $\vec{s_1} - \vec{s_2} = |s_1||s_2|\cos\theta_{\mathrm{sep}} = sqrt(2 - 2\cos\theta_{\mathrm{sep}} \approx \Theta_{\mathrm{sep}}$ using a second-order small angle approximation for $\cos\theta_{\mathrm{sep}}$ as the sources are close on the sky. Compared to the original delay error of (3.5), we can see that the differencing reduced the error by a factor of θ_{sep}. When observing the two sources at (nearly) the same time, propagation errors ($\Delta\tau_{\mathrm{tropo}}, \Delta\tau_{\mathrm{iono}}$) also scale roughly with θ_{sep}, while the differential instrumental term is either negligible or can be accurately measured. Thermal errors are random and are not reduced by relative astrometry; on the contrary, as $\Delta\tau_{\mathrm{therm}} \propto 1/SNR$, where SNR is the signal-to-noise of the measurement and depends on the flux density of the observed source, it is possible for thermal errors to increase on the target due to differencing if the reference source is weak. However, the dominant error sources in relative radio astrometry are usually uncompensated propagation errors, and a rough estimate on the astrometric error of relative astrometric measurements can be given as

$$\Delta s_{\mathrm{rel}} \approx \theta_{\mathrm{sep}}\frac{c\Delta\tau}{|B|} \quad . \tag{3.7}$$

Comparing (3.7) and (3.2), we can see that the original astrometric error is reduced by θ_{sep} thanks to the relative measurements. Using our previous example of a typical delay error of $\Delta\tau \approx 0.1$ ns on a 6000 km baseline and a possible source separation of $\theta_{\mathrm{sep}} \approx 1^\circ$, we get a relative astrometric error of $\Delta s\mathrm{rel} \approx 0.02$ mas – an increase in accuracy by a factor of 50.

3.1.2 Phase referencing techniques for spectral line astrometry

Up to this point, we were talking about τ delays and $\Delta\tau$ delay errors as the observables of a VLBI array. However, in practice the observed quantities are complex voltage signals that store both the amplitude and phase information of the incoming radio signals (see Fig. 3.2). In principle, the previously mentioned τ delay is the time-of-arrival difference of the radio signals between a pair of antennas, and is measured by comparing the signal with different trial delays until a good match is found. This is called correlation, because in practice these different trial delays are multiplied together with the recorded signal until a maximum is discovered at a given τ delay value, i.e. the signals correlate. This delay, also called "group" delay is measured in time, but we can also represent it and measure it as a "phase" delay

$$\tau_\varphi = \frac{\varphi}{2\pi\nu} \ , \tag{3.8}$$

where φ is the phase of the signal and ν is the observed frequency. The φ phase can be measured much more accurately than the time shift of τ, however determining the number of phase cycles and resolving this ambiguity is difficult and requires very accurate a priori models which cannot be done at the correlator. However as we saw previously with the differential delays in (3.4), we are not really interested in the total value of τ_g for our astrometry, only the $\tau_{\mathrm{g},1} - \tau_{\mathrm{g},2}$ relative term between a target and reference source. With precise relative astrometric techniques, we can cancel out the errors well enough to resolve the issue of ambiguous phase cycles and measure very precisely the relative changes in phase between sources. This differential phase calibration method is called *phase referencing*, and it is the implementation of (3.4) and relative astrometry in practice.

In reality, the observed phases change with time and the target (1) and reference (2) sources are usually not observed simultaneously (refer back to Fig. 3.1). Let's again write down (3.3), but this time using $\varphi(t)$ phases after a priori phases were already subtracted in the correlator, calculated by using the τ "group" delay observables. We get the following residual phases for the two sources:

$$\begin{aligned}\varphi_1(t_1) - \varphi_{\mathrm{apri},1}(t_1) = \varphi_{\mathrm{pos},1}(t_1) + \Delta\varphi_{\mathrm{struc},1}(t_1) + \Delta\varphi_{\mathrm{dtropo},1}(t_1) + \Delta\varphi_{\mathrm{stropo},1}(t_1) + \\ + \Delta\varphi_{\mathrm{diono},1}(t_1) + \Delta\varphi_{\mathrm{siono},1}(t_1) + \Delta\varphi_{\mathrm{bl},1}(t_1) + \Delta\varphi_{\mathrm{inst},1}(t_1) + \Delta\varphi_{\mathrm{therm},1}(t_1)\end{aligned} \tag{3.9}$$

$$\begin{aligned}\varphi_2(t_2) - \varphi_{\mathrm{apri},2}(t_2) = \varphi_{\mathrm{pos},2}(t_2) + \Delta\varphi_{\mathrm{struc},2}(t_2) + \Delta\varphi_{\mathrm{dtropo},2}(t_2) + \Delta\varphi_{\mathrm{stropo},2}(t_2) + \\ + \Delta\varphi_{\mathrm{diono},2}(t_2) + \Delta\varphi_{\mathrm{siono},2}(t_2) + \Delta\varphi_{\mathrm{bl},2}(t_2) + \Delta\varphi_{\mathrm{inst},2}(t_2) + \Delta\varphi_{\mathrm{therm},2}(t_2)\end{aligned} \tag{3.10}$$

where $\varphi_1(t_1)$ and $\varphi_2(t_2)$ are the observed phases for the two sources at slightly different times, $\varphi_{\mathrm{apri},1}(t_1)$ and $\varphi_{\mathrm{apri},2}(t_2)$ are the calculated correlator phase corrections (they most importantly remove the majority of the τ_g geometric delays), and finally $\varphi_{\mathrm{pos},1}(t_1)$ and $\varphi_{\mathrm{pos},2}(t_2)$ are the phase signatures of the remaining geometric terms after the corrections in the correlator and represent the residual offsets relative to the assumed a priori source positions in the correlator model; these are the phase terms we want to preserve with phase referencing as they carry the information of the sources' astrometric positions. All the remaining terms are ones discussed before, but as $\Delta\varphi$ phase errors.

As the two sources usually cannot be observed together due to the limited size of the VLBI beam and the availability of bright enough reference sources, also called as calibrators. Therefore observations alternate between target and reference in short scans (usually in every few minutes)

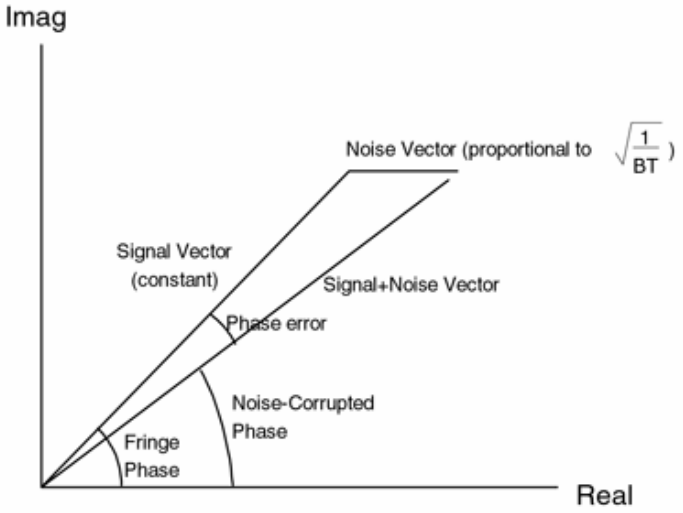

Figure 3.2. The VLBI signal and noise as vectors in the complex plane. The VLBI signal is fundamentally a vector quantity with an amplitude and phase ("signal vector"). The signal vector's phase ("fringe phase") corresponds to the phase-delay difference of the signal arriving at the two antennas of a baseline at a particular time, but in practice the signal vector is ambiguous by many 2π rotations. Assuming that all error sources have been calibrated, the signal vector becomes constant, but gets corrupted by an additive "noise vector" from the thermal noise. The noise vector has a random phase and an amplitude $\propto \sqrt{1/(B \cdot T)}$ where B is the channel bandwidth and T is the observing time. Therefore, the SNR signal-to-noise ratio is $\propto \sqrt{B \cdot T}$. Note that the SNR is roughly the ratio of the lengths of the signal vector to the random noise vector, whereas the average phase error of the signal+noise vector is approximately the ratio of the noise vector to signal vector, i.e. 1/SNR. Figure and explanation taken from Whitney (2000).

and the phases determined for the reference source at t_2 are interpolated to the target scan at t_1. Everything else is done as discussed in the previous section: the reference source's $\Delta\varphi_{\mathrm{struc},2}(t_2)$ structure phase term is determined using hybrid mapping and then subtracted to determine the rest of the antenna-based error terms. This is done by a technique called fringe fitting (Cotton, 1995), and it solves for all additional phase terms including the $\varphi_{\mathrm{pos},2}(t_2)$ positional term, too. However, this is not a problem as we know the position of the reference source from earlier relative or absolute astrometric measurements. Also, reference sources are usually far-away quasars that do not move between observing epochs (their position might wander around tiny amounts from structural changes, but those can be measured with hybrid mapping in each epoch), so they provide a stable reference point to which measure the relative movement of our Galactic maser sources. In any case, we are able to determine the reference source's $\Delta\varphi_{\mathrm{struc},2}(t_2)$ structure phase and $\varphi_{\mathrm{cal},2}(t_1) = \varphi_{\mathrm{pos},2}(t_1) + \Delta\varphi_{\mathrm{dtropo},2}(t_1) + \Delta\varphi_{\mathrm{stropo},2}(t_1) + \Delta\varphi_{\mathrm{diono},2}(t_1) + \Delta\varphi_{\mathrm{siono},2}(t_1) + \Delta\varphi_{\mathrm{bl},2}(t_1) + \Delta\varphi_{\mathrm{inst},2}(t_1) + \Delta\varphi_{\mathrm{therm},2}(t_1)$ additional phase terms bundled together and interpolated to the target scan times. It is then subtracted from the target's phase, i.e. the target is phase referenced using the calibrator, to mitigate or cancel out the target phase errors and tie its position to the reference source. This can be written in the following general form, similar to (3.4), to get the calibrated phase of the target:

$$\varphi_1(t_1) - \varphi_{\mathrm{apri},1}(t_1) - \varphi_{\mathrm{cal},2}(t_1) = \Delta\varphi_{\mathrm{struc},1}(t_1) + \varphi^{1-2}_{\mathrm{pos}}(t_1) + \Delta\varphi^{1-2}_{\mathrm{dtropo}}(t_1) + \Delta\varphi^{1-2}_{\mathrm{stropo}}(t_1) + \\ + \Delta\varphi^{1-2}_{\mathrm{diono}}(t_1) + \Delta\varphi^{1-2}_{\mathrm{siono}}(t_1) + \Delta\varphi^{1-2}_{\mathrm{bl}}(t_1) + \Delta\varphi^{1-2}_{\mathrm{inst}}(t_1) + \Delta\varphi^{1-2}_{\mathrm{therm}}(t_1) \quad , \quad (3.11)$$

where $\varphi^{1-2}(t_1) = \varphi_1(t_1) - \varphi_2(t_1)$ represent the differential phases between the target (1) and the reference source (2) for each component. Here the $\Delta\varphi_{\mathrm{struc},1}(t_1)$ term carries the astrometric information about the source structure, which is usually negligible for maser sources as they are

unresolved (or unresolved components can be found). This term is hard to quantify and should be dealt with on a case-by-case basis, as masers have a highly variable spatial and velocity structures. See the VLBA OH maser data reduction of WX Psc in Sect. 4.1 to see how serious problems can maser structure cause, which can only be dealt with is there are many maser spots to follow around a source. For continuum sources this term is usually not a problem and can be evaluated after imaging the phase referenced target; thus we are going to ignore it for this overview. $\varphi^{1-2}_{\rm pos}(t_1)$ is the phase term introduced by the target's relative offset with respect to the reference source (calibrator), i.e. the position vector we want to measure. The rest of the $\Delta\varphi^{1-2}(t_1)$ terms are the residual phase errors that contribute to the uncertainty of our astrometric measurements and should be minimized.

Although phase referencing if capable of removing a large amount of the phase errors, residual phase errors remain even after the phase corrections using a calibrator. In *conventional phase referencing*, a target is observed with a close-by calibrator by alternating between the two sources in every few minutes. As the two sources are observed with a certain time separation and not on the same line of sight, residual phase errors will remain. As the same receiving system is used, $\Delta\varphi^{1-2}_{\rm inst}(t_1)$ and $\Delta\varphi^{1-2}_{\rm bl}(t_1)$ is negligible while the residual propagation errors depend on the observing frequency: above $\sim$10 GHz the non-dispersive tropospheric phase errors dominate while at lower frequencies the ionospheric errors become the limiting issue (see Fig. 3.3, Peterson et al., 2011). $\Delta\varphi^{1-2}_{\rm dtropo}(t_1)$ terms can be compensated for by faster switching times between target–calibrator scans, or by using special techniques such as SFPR (Rioja & Dodson, 2011) and MFPR (Dodson et al., 2017) that rely on (near) simultaneous observation at several frequencies to remove dynamic tropospheric terms. The $\Delta\varphi^{1-2}_{\rm stropo}(t_1)$ error can be compensated by either using "geodetic blocks" (Reid et al., 2009), i.e. observing many calibrators at a wide range of angles to directly measure the static effect of the air mass above each antenna, or by using external data such as GPS measurements to correct the VLBI data (Honma et al., 2008a). Ionospheric errors are hard to deal with conventional phase referencing, and seriously limit the accuracy below $\sim$5 GHz (see Sect. 3.2). The thermal error depends on the same issues as discussed in the previous chapter and possible phase ambiguities are also ignored, as they always have to be dealt with on a case-by-case basis.

A special case of conventional phase referencing is *in-beam phase referencing*, when the target and calibrator are observed simultaneously in the same field-of-view (see Sect. 4.1 for a comprehensive analysis of in-beam phase referencing at low frequencies). Due to the simultaneous observations there is no need for interpolating the calibrator phases, which greatly mitigates the dynamic error effects. Static effects from the atmosphere still remain due to the slightly different source line-of-sights. The VERA array's *dual beam system* (Honma et al., 2008b) basically mimics in-beam astrometry for larger separations, as it effectively cancels the dynamic tropospheric phase error which is the dominant term at 22 GHz and 43 GHz where VERA operates (Asaki et al., 2007). It however does not deal with the static terms, which is done separately. It also introduces an $\Delta\varphi^{1-2}_{\rm inst}(t_1)$ phase residual as the two beams have to independent receiver systems and electronics: instrumental effects therefore have to be calibrated to avoid serious systematic errors. This is done by using artificial noise sources mounted on the antenna that inject both beams with the same signals, from which the differential instrumental phase offsets between the two beams can be calculated and removed during data reduction.

To deal with ionospheric phase residuals, it is possible to use multiple calibrators around the target and create a virtual calibrator for the line-of-sight of the target source, by assuming that the dominant $\Delta\varphi^{1-2}_{\rm siono}(t_1)$ phase errors change linearly between the calibrator line-of-sights (see

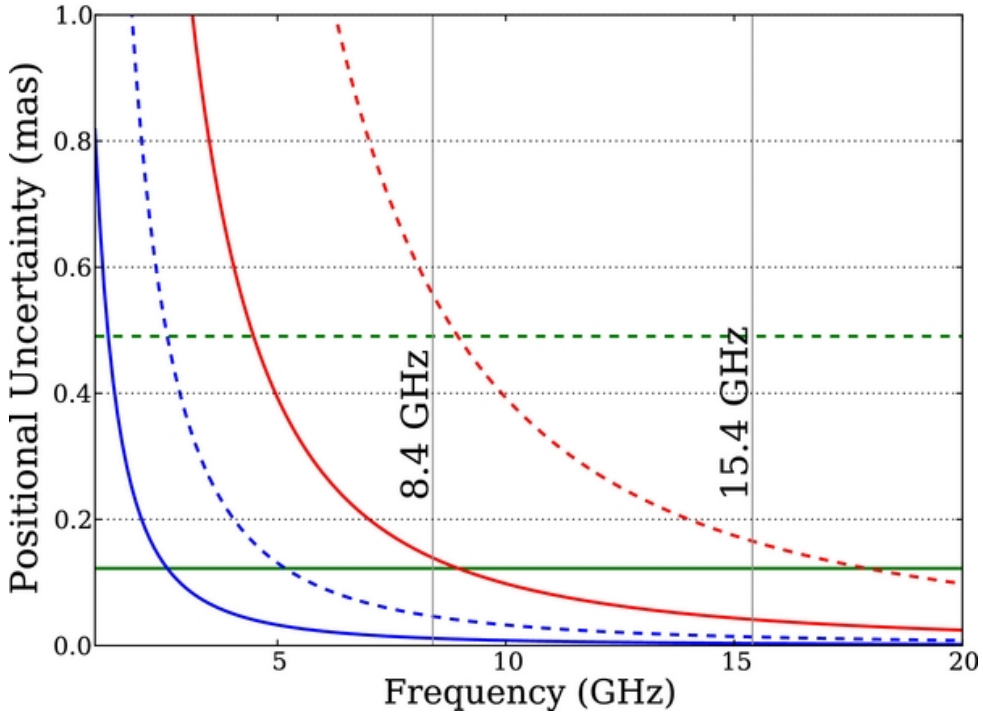

Figure 3.3. Atmospheric errors in VLBI measurements as a function of frequency from Peterson et al. (2011). The solid and dashed lines show position uncertainties for target–calibrator separations of 1°and 4°respectively. Tropospheric delay errors of ± 0.1 ns are shown by green lines, the daytime ionosphere contributions of ± 0.1 ns (∼5 TECU) are shown by red lines, and nighttime ionospheric contributions (∼0.5 TECU) are shown by blue lines. The data is simulated using a 104 km baseline and a 70°zenith angle (defines $\vec{s}$ source unit vector). Position uncertainty is the $\Delta\varphi$ phase error multiplied by the resolution of the array ($\sim \lambda/B$). At 8.4 GHz, the daytime ionospheric contribution is comparable to the tropospheric contribution, while the troposphere dominates higher frequencies and the ionosphere the lower frequencies, since $\Delta\tau_{\text{iono}} \propto \lambda^2$.

Fig. 3.4). This removes the biggest systematic error from the low frequency astrometric error budget. Dynamic terms still remain as all calibrators would need to be observed simultaneously in order to remove their effect. This will be achievable with next-generation radio telescopes, like the SKA; see Sect. 3.2 for the first demonstration of *multi-calibrator phase referencing* using VLBI observations and the residual phase terms directly).

Finally, I want to note that all this chapter focused on phase referencing and trying to not solve for the $\varphi_{\text{pos}}^{1-2}(t_1)$ phase term and thus retain the maser's position relative to the reference source. This is essential when measuring the parallax and absolute proper motion of a maser, however there is an alternative way if we are only interested in the internal proper motions. If there are stable maser spots in a dataset, they can be used as reference sources to calibrate all other maser channels in an image cube, i.e. essentially phase referencing all other spots to the selected reference spot. Of course the positional information of the reference maser spot will be lost, but the motions of the other masers will be very precisely tied to this one spot. So if we choose a spot carefully (e.g. making sure it does not have some huge unknown proper motion, or it is not variable), it is possible to trace the internal motions of the other maser spots between epochs relative to the reference spot. This is a widely used technique in maser astrometric studies (e.g. Chong et al., 2015; Burns et al., 2015; Imai et al., 2013a), and although it relies on some assumptions, it has proven very adaptable especially for sources with bipolar maser outflows

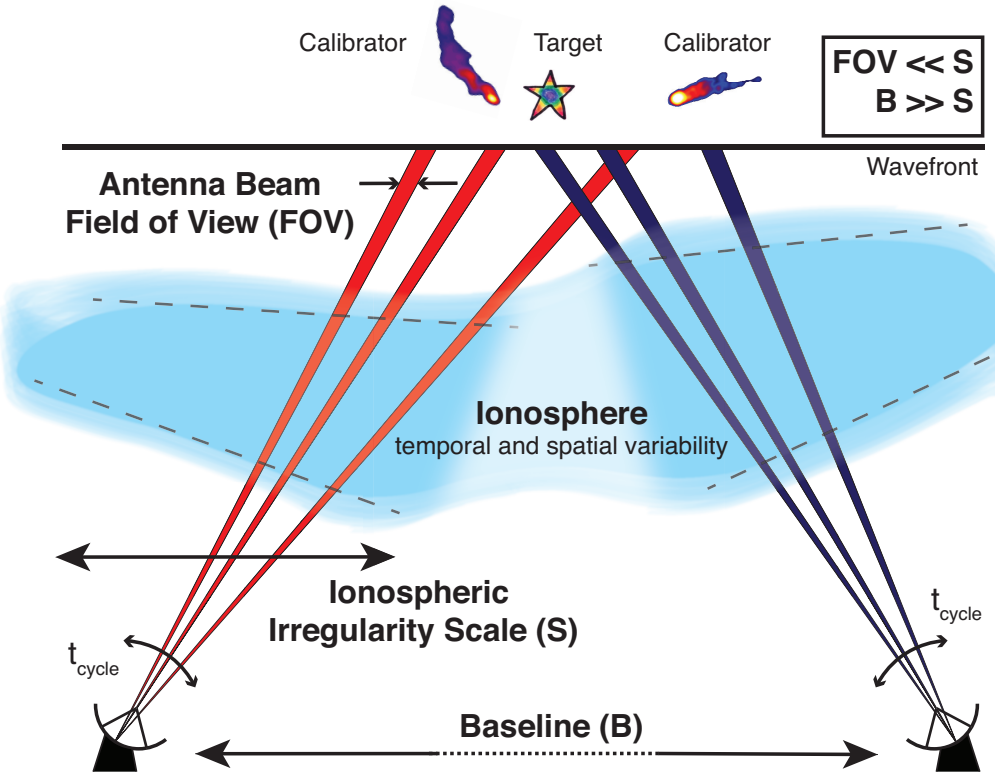

Figure 3.4. The principle of multi-calibrator phase referencing (MultiView). Observing multiple calibrators around the target allows the first order modeling of the ionosphere (dashed lines), thus removing the major error source in low-frequency astrometry. Calibrators can be several degrees away, as long as they trace the same isoplanatic patch (S) above a telescope (adapted from Lonsdale, 2004).

where more stringent constraints can be set (see Sect. 5.2 for more on this technique).

3.2 Calibration at low frequencies: the MultiView technique

VLBI observations hold the potential to achieve the highest astrometric accuracy in astronomy, provided that the fringe phase observable can be calibrated (Alef, 1988). The development of advanced phase referencing PR techniques to compensate for the tropospheric propagation errors have led to routinely achieving μas astrometry at frequencies between approximately 10 and a few tens of GHz using alternating observations of the target and a nearby calibrator, which can be up to a few degrees away (Reid & Brunthaler, 2004; Honma et al., 2008a). The increasingly fast tropospheric fluctuations at higher frequencies set an upper threshold for application of PR techniques at $\sim$43 GHz (with but a single case at 86 GHz, Porcas & Rioja, 2002). More recently, the development of phase calibration techniques using (nearly) simultaneous observations at multiple mm-wavelengths, that is SFPR (Rioja & Dodson, 2011) and MFPR (Dodson et al., 2017), have extended the capability to measure μas astrometry up to mm-wavelengths. This capability for accurate astrometry has resulted in a wide applicability to many scientific problems (Reid & Honma, 2014, and references therein).

Nevertheless the application of these advanced PR techniques to relatively low frequencies $\leq$8 GHz are hindered by the contribution of ionospheric propagation effects, increasingly dom-

inant at lower frequencies, which have a different nature to the tropospheric effects. The unpredictability of the spatial irregularities in the plasma density in the ionosphere introduces differential path variations between the sky directions of the two sources, and propagate into systematic position errors even for small source separations. In addition, at the lowest frequencies, the temporal variations are also an issue. These both are responsible for degrading the positional accuracy achieved with this technique and, eventually, prevent the phase connection process and the use of conventional phase referencing.

Therefore, a new strategy is required to overcome the limitations imposed by the ionospheric propagation medium and to reach the full potential of the instruments working on these spectral regimes, such as the SKA that will have VLBI capability between 0.3 and 14 GHz. In general, observations which involve more than one calibrator have demonstrated advantages for astrometric VLBI at low frequencies (Fomalont & Kopeikin, 2002; Rioja et al., 2002; Doi et al., 2006). The alternative is the unusual configuration when a target and a strong calibrator lie within the field-of-view of the VLBI antennas (i.e. an in-beam calibrator), and thus can be observed simultaneously (Wrobel et al., 2000; Fomalont et al., 1999). A useful variation of this combines the observations of a weak in-beam calibrator source and nodding to a strong more distant calibrator. The observations of the strong calibrator are used to remove the first-order atmospheric effects; then the observations of the weak in-beam source, which is observed along with the target source, provide further adjustments of the spatial and temporal fluctuations, with longer coherence times. The results obtained with this approach are positive, however its widespread application is still limited by sensitivity. Another useful approach is when there are two calibrators aligned with, but on opposite sides of, the target (Fomalont & Kopeikin, 2002). During the observations the telescopes alternate every few minutes between the three sources, and in the analysis successive scans on the calibrators are used for the spatial and temporal interpolation to the enclosed position and scan time of the target source. The rare source configuration required for this approach to work results in limited applicability, and the calibration time overhead is large.

This chapter presents results from the MultiView technique which, by deriving 2D phase screens from observations of three or more calibrators, achieves a superior mitigation of atmospheric errors that results in increased precision astrometry, along with wide applicability by relaxing the constraints on the angular separation up to few degrees, and does not require alignment of sources. The scope of application is for the low frequency regime where the performance of PR is degraded due to the spatial structure of the ionospheric dominant errors. It is a development of the "cluster–cluster" VLBI technique, which allowed simultaneous observations of a target and multiple calibrators around it by replacing single telescopes by sites with multiple elements (Rioja et al., 1997). The ability of the "cluster–cluster" technique to address the ionospheric effects has been demonstrated with joint observations between connected interferometer arrays at 1.6 GHz of a target and three calibrator sources (Rioja et al., 2002, 2009). Despite these benefits its use has been limited by the shortage of compatible observing sites, and the complexity in its implementation.

Finally, this new technique is revisited in the light of the next generation of instruments for low frequency observations that will become operational in the course of the next decade. These have the multi-beam capability as an "in-built" feature, such as the ASKAP in the near future, and SKA in the longer term. I believe that the implementation of MultiView techniques will enhance the performance of VLBI observations, by providing higher precision astrometric measurements of many targets at low frequencies.

3.2.1 Observations

In an effort to demonstrate the improvements by MultiView calibration over conventional techniques, two epochs of observations were conducted with the VLBA separated by one month, on 2015 June 8 (Epoch I, obs. ID: BO047A7) and July 7 (Epoch II, obs. ID: BO047A4), at 1.6 GHz. Both epochs of observations used identical setups with a duration of 4 hours. Table 3.1 lists the source names and coordinates and Fig. 3.5 shows the distribution in the sky.

Source	Alias	Right Ascension (h m s)	Declination (° ′ ″)	σ_{RA} (mas)	σ_{DEC} (mas)	S $_{1.6\,\mathrm{GHz}}$ (Jy b^{-1})
J0121+1149	C1	01 21 41.595044	+11 49 50.41304	0.10	0.10	2.1
J0113+1324	C2	01 13 54.510365	+13 24 52.47783	0.26	0.38	0.08
J0042+1009	C3	00 42 44.371738	+10 09 49.20750	0.15	0.17	0.17
J0106+1300	C4	01 06 33.356509	+13 00 02.60390	0.14	0.19	0.07
OH128.6–50.1	OH	01 06 25.98	+12 35 53.0			0.11

Table 3.1. All observed sources: four quasars and one OH maser line source (also known as WX Psc). Columns 1 and 2 are the source names and aliases used through this paper, respectively. Columns 3 and 4 are the Right Ascension and Declination coordinates used at the correlator. Columns 5 and 6 are the corresponding position errors, if available. Column 7 is the peak brightness at 1.6 GHz measured from our observations. For quasars, all quantities are from the VLBA Radio Fundamental Catalog (L. Petrov, solution rfc2015b available at astrogeo.org). For the OH maser, position comes from the SIMBAD Astronomical Database (Wenger et al., 2000).

The observations consisted of alternated scans switching between all the sources with a duty cycle of ∼5 minutes. The two sources in the centre of the distribution, the OH maser source and the quasar C4, were observed simultaneously because they lie within the primary beam of the VLBA antennas. They are the targets of the analyses presented in this chapter, allowing the MultiView calibration to be tested for both a maser line and quasar continuum observations simultaneously. The sessions were long enough to ensure sufficient (u, v) coverage and sensitivity, spending ∼40% of the time on the OH–C4 pair with alternating 30–90 s scans on the C1, C2 and C3 calibrators. Both epochs were observed at a similar time range around early morning, 12:06:00−16:06:00 UT for Epoch I and 11:12:00−15:12:00 UT for Epoch II, when the variations in the ionosphere and its effects on astrometry are expected to be the largest.

The 2-bit quantized signals were recorded in dual circular polarization with 256 Mbps using 4 intermediate frequency (IF) bands, each with a bandwidth of 8 MHz. The IFs were spread out over 300 MHz, centered around the four ground-state OH maser lines of 1612, 1665, 1667, 1720 MHz and the H I line at 1420 MHz. Each band had a channel spacing of 1.95 kHz, corresponding to a velocity resolution of 0.36 km s^{-1}. All bands were correlated in a single run, using two phase centers for the observations of the OH–C4 pair. For the OH maser source, only the 1612 MHz transition provided useful astrometric data.

3.2.2 Astrometric Data Analyses

A comparative astrometric study was carried out using different calibration techniques and angular separations, summarized in Table 3.3, on the same observations. The analyses comprise

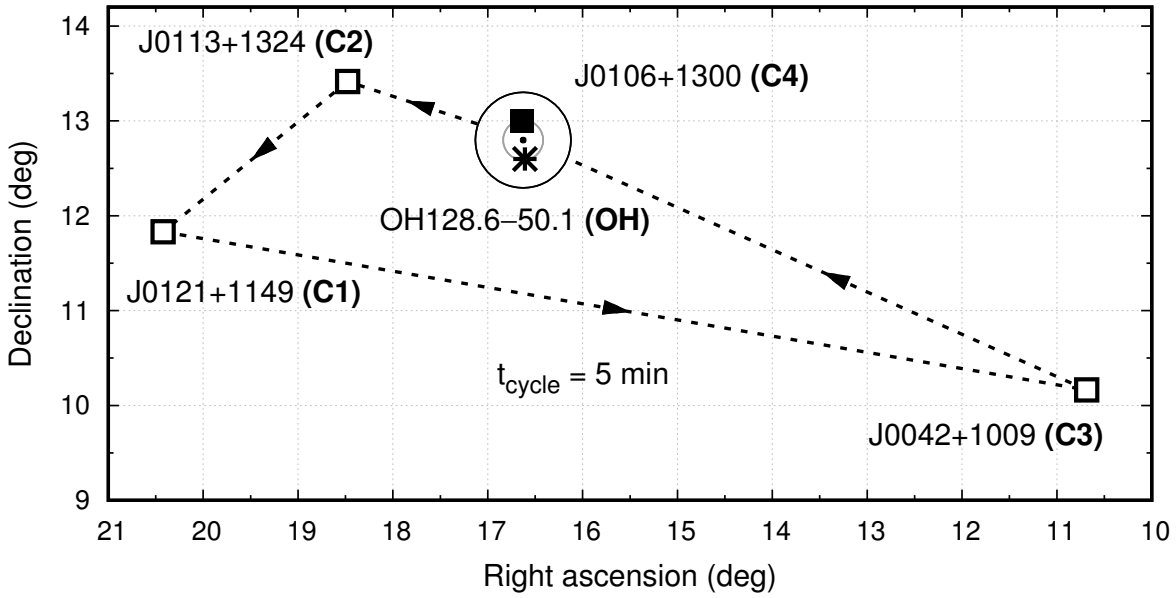

Figure 3.5. Sky distribution of the sources observed with the VLBA at 1.6 GHz. Table 3.1 lists the source coordinates. Dashed lines and arrows mark the source switching order during the observations with 5-min duty cycles. Star and solid symbols mark the simultaneously observed OH–C4 pair, with the VLBA antennas pointed halfway between the two. The two concentric circles represent the half-power beamwidth and full beamwidth of the antennas. Both OH and C4 are targets in the astrometric analysis (see Table 3.3). C1 was used as the fringe-finder.

conventional PR techniques using pairs of sources (i.e. one calibrator and one target source) with angular separations of $\sim 0.^{\circ}4$ (i.e. in-beam), 2°, 4° and 6°, and MV techniques using four sources (i.e. three calibrators and one target sources). The targets are the quasar C4 and the OH maser source, while the calibrators are quasars in all cases. We use the alternating quasar-only observations for the comparison between PR with a range of angular separations and MV techniques, using C4 as the target; using the OH maser source as target, we compare in-beam PR with C4 as reference, $0.^{\circ}4$ away, to MV using three calibrators 2°, 4°, and 6° away. Note that the MV observations in this paper involve source switching. The repeatability of the astrometric measurements between the two epochs (i.e. inter-epoch differences) is the chosen figure of merit for our comparative study of the calibration strategies. For the quasars-only analysis, the repeatabilities are a direct indication of the uncompensated ionospheric errors remaining after calibration, given that no source position changes are expected. For the OH maser analysis, the apparent source motion due to the proper motion and parallax needs to be accounted for first, even over a 1 month timeline. Section 3.2.2 will cover the astrometric error analysis.

The PR analyses were carried out following standard procedures in the AIPS software(Greisen, 2003). The MV analyses (Fig. 3.6) were carried out following the same procedures in AIPS but with additional steps to incorporate direction dependent effects, as described in Sect. 3.2.2. Also, self calibration maps have been made of all sources using conventional hybrid mapping techniques in VLBI using AIPS and Difmap (Shepherd, 1997); these have been used to remove the source structure contribution, to provide reference points for the astrometric analysis and to asses the quality of the calibration strategies using the fractional flux recovery quantity (see

Sect. 3.2.2).

Basis of MultiView Direction Dependent Phase Calibration

The MV calibration strategy corrects for the direction dependent nature of the ionospheric phase errors by using simultaneous or near-simultaneous observations of multiple calibrators around the target. Then the antenna phases, estimated along the directions of all calibrators, are interpolated using bilinear interpolation, to provide corrections along the line of sight of the target observations. This is realized by a weighted linear combination of the complex antenna gains, representing the relative source distribution in the sky, as shown in Fig. 3.5 for the case of interest to this demonstration. This is equivalent to the treatment of the propagation medium as a wedge-like spatial structure, up to several degrees in size, above each antenna (Fomalont & Kopeikin, 2002; Rioja et al., 2002). The temporal structure of the propagation medium effects is best calibrated using simultaneous observations of the calibrators and the target sources in MV observations. However when this observing configuration is not possible one can use alternating observations of the sources, as long as the duty cycle is less than the atmospheric coherence time.

Therefore, in MV the target position is tied to the assumed positions of the multiple calibrators weighted as in the analysis (see Table 3.2). That is, to a virtual point in the sky whose location depends on the source distribution in the sky. Instead, in PR the measured target positions are tied to the assumed position of the corresponding (single) calibrators. Nevertheless, as long as the calibrator sources provide good fiducial points (i.e. are stationary), this virtual point is also stationary and changes between the astrometric measurements at different epochs trace the motion of the target in both MV and PR.

Target Source	Weight_1	Weight_2
J0106+1300 (C4)	1.147	0.1735
OH128.6–50.1 (OH)	0.985	0.2475

Table 3.2. MultiView weights used to implement the direction dependent ionospheric calibration along the line of the sight of the target source in the analyses. Column 1 lists the target sources, for analyses MV_{QSO} and MV_{OH}, respectively. Columns 2 and 3 are the weights that were applied for the phase transfer between C2 and C1 ("Weight_1"), and between C3 and this combination ("Weight_2"), for the calibration of the corresponding target source.

The implementation of the MV direction dependent calibration strategy is more complicated than a basic bilinear interpolation and the calculated φ_{MV} phases can be written as

$$\varphi_{MV} = \Big[(\varphi_{C3} \pm n2\pi)\, w_1 + (\varphi_{C2} \pm m2\pi)(1 - w_1)\Big]\, w_2 + (\varphi_{C1} \pm p2\pi)(1 - w_2) \ , \tag{3.12}$$

where $\varphi_{C1}, \varphi_{C2}, \varphi_{C2}$ are the phase solutions for the individual calibrators (these terms would be used in normal phase referencing to correct the target phases). The calculated MV phase solution includes a correction for untracked 2π phase ambiguities in the measured calibrator phases, which would lead to errors in the spatial interpolation. Those are automatically detected by searching over ambiguities in the formation of every interpolation (i.e. changing n, m, p in the equation) and optimizing the result. Additionally, one has the ability to steer the corrections by forcing the addition of ambiguities at the outset.

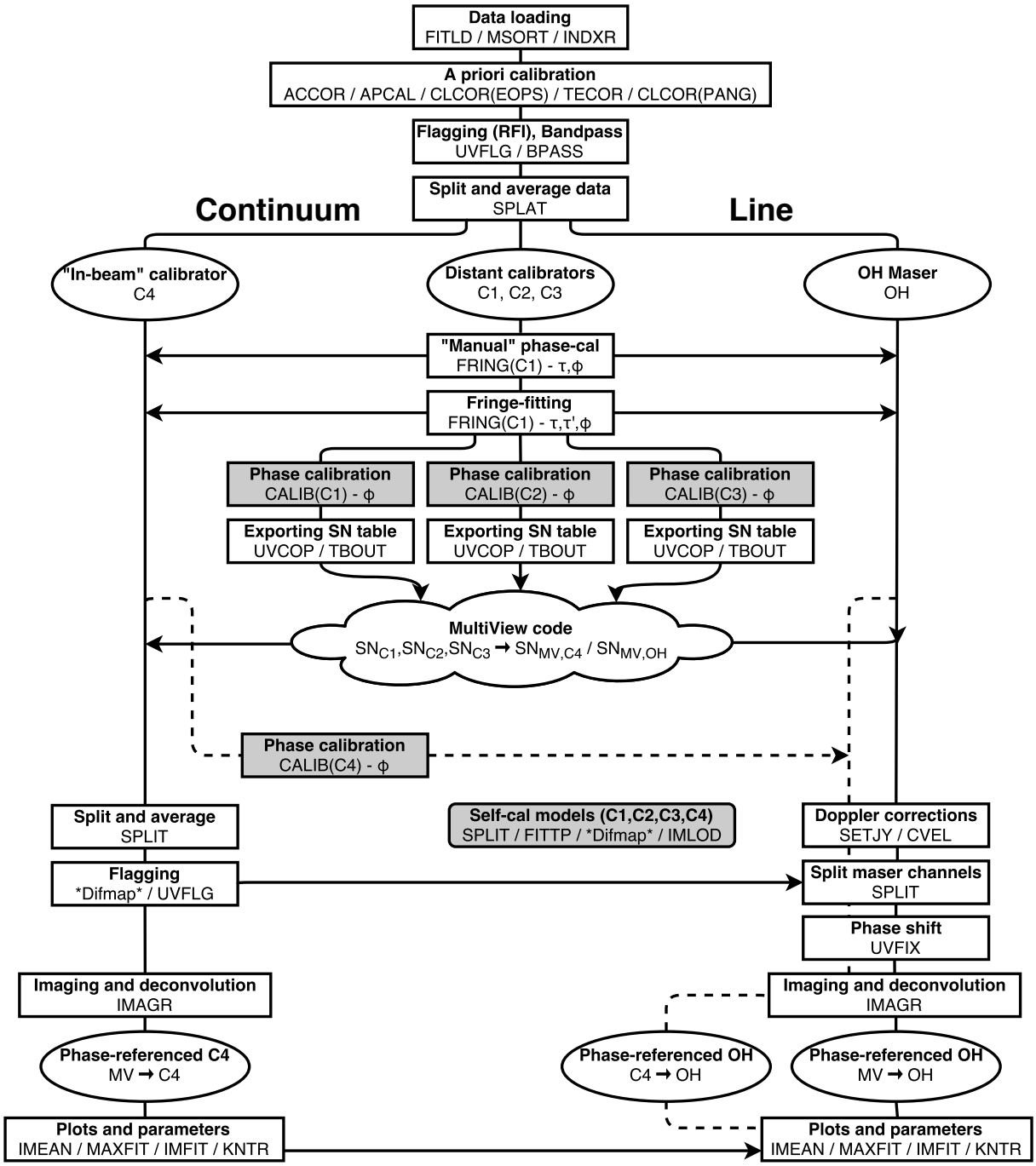

Figure 3.6. Schematic flow of MultiView calibration. Rectangles represent specific steps in the calibration, while ellipses indicate important datasets created during calibration. Shading means that source structure models were created or used in the calibration step. The cloud represents the external MultiView code. Arrows mean the copying and applying of SN or FG tables between datasets. Dashed lines show the in-beam calibration flow where it diverges from the MV calibration. In all cases the sources, AIPS tasks and derived solutions are specified.

Astrometric Calibration	Target Source(s)	Reference Source	Angular Separation	Analysis ID
Single Calibrator				
PR	C4	C2	1.°84	PR_{2°
PR	C4	C1	3.°88	PR_{4°
PR	C4	C3	6.°49	PR_{6°
in-beam PR	OH	C4	0.°4	$PR_{in-beam}$
Three Calibrators				
MV	C4	C1, C2, C3	1.°84, 3.°88, 6.°49	MV_{QSO}
MV	OH	C1, C2, C3	2.°00, 3.°81, 6.°30	MV_{OH}

Table 3.3. Astrometric analyses compared in this paper, along with aliases used throughout the text. Column 1 are the calibration techniques: using a single calibrator, regardless that the observations of the pair are carried out using source switching or simultaneously observed, and using three calibrators; PR = Phase Referencing and MV = MultiView. Columns 2 and 3 list of target and reference sources, respectively. Column 4 is the target–calibrator(s) angular separation. Column 5 is the analysis identification name used throughout the text. All analyses have been carried out for epochs I and II, separated by one month.

Error Analysis

The following approaches have been used to quantify the uncertainties of the astrometric measurements in the MultiView demonstration and PR comparison.

Repeatability errors. The repeatability of the measured positions between the two epochs of observations, which provide independent measurements of the relative source position, is used as an empirical estimate of the astrometric errors. The difference (Δ_{I-II}) of the positions are indicative of uncompensated systematic ionospheric residual errors remaining after calibration for each analysis. The repeatability errors, corrected for the bias introduced by having only two measurements, are calculated as: $\sigma_{\rm pos,rep} = \Delta_{I-II} \times \sqrt{2/\pi}$. They are a measure of the precision of the calibration method, in absence of inherent position changes, and are used as the figure of merit for the comparative study. Note that while there is a limited sample of two epochs the different analyses are carried out on the same observations, enabling a direct comparison of the compensation efficiency of the systematic errors under the same weather conditions.

Thermal noise (and other random) errors. The ratio of the synthesized beam size (θ_B) and SNR in the astrometric maps (i.e. PRed and MVed maps) gives an estimate of the uncertainty in the measurement of the position of a feature in the maps due to random noise, as $\sigma_{\rm pos,thermal} \sim 0.5\theta_B/SNR$. This error has a contribution from thermal (usually dominated by the receiver) random noise, and from residual atmospheric phase fluctuations. The latter depends on the duty cycle during the observations, the angular separation between sources and the weather conditions. It is commonly referred to as the thermal noise error and represents the ultimate astrometric precision achievable, in absence of any other error contributions. It is usually overwhelmed by other systematic contributions.

Fractional Flux Recovery. The FFR quantity is defined as the ratio between the peak brightness in the astrometric maps (i.e. PRed and MVed maps) and the self-calibrated maps of the same source. It is a useful quantity for comparison between methods and is related to the thermal noise

error. It provides an empirical estimate of the residual uncorrelated errors, such as atmospheric phase fluctuations, which result in image coherence losses. In general, image coherence losses arise from residual short term phase fluctuations, hence it is expected to increase with larger duty cycles (in this case the duty cycle is 300 s). The coherence losses also increase with the source's angular separation, due to residual long term phase variations which distort the image. Nevertheless, neither of these quantities are sensitive to error processes that cause systematic position offsets, such as those expected from the spatial structure, direction dependent nature, of the ionospheric errors.

Accuracy. The observed quasars were selected from a VLBI catalog with precise positions with accuracies $\sim$ 0.2 mas (rfc2015b). Differences of no more than a few mas between the catalog positions and the relative astrometric measurements presented in this paper are expected, arising from the effects that effectively change the measured positions. These are: the use of group delays observable in geodetic analysis compared to the phase delays in our relative astrometry analysis (Porcas, 2009), expected position changes in the observed core at different frequencies (i.e. the core-shift effect) and differential structure blending effects between the observing frequencies of the catalog (calculated "ionosphere-free" positions from S/X band observations, i.e. at an infinite frequency) and the presented VLBA observations (1.6 GHz).

3.2.3 Results

The main goal of these observations was to demonstrate the feasibility of MV to achieve high precision astrometry at low frequencies, along with a comparative study between MV and PR.

Calibrated Visibility Phases and Astrometric Images: MV vs PR

Visibility Phases. Fig. 3.7 shows a superposition of the residual relative visibility phases of C4 for a representative subset of baselines, after calibration using PR (analysis id: PR_{2°, PR_{4° and PR_{6°) and MV (analysis id: MV_{QSO}) for the same range of target–calibrator angular separations, from epochs I (left) and II (right). The long time-scale trends in PR analysis are easily appreciated: the deviations from zero are increasingly large for pairs with larger angular separation and are different in the two epochs, with epoch II being significantly better. This is indicative of systematic residual phase errors, which depend mainly on the weather conditions. Satellite-based GPS data [5] are consistent with epoch II ionospheric conditions being more benign (see Figs. 3.8,3.9). The largest disturbances are seen at the beginning of the observations, which correspond to times near sunrise. Note that, in epoch II, the phases for the 6° angular separation pair are larger (by about a factor of $\sim$3) and with opposite sign compared to those for the 2° pair and that they correspond to calibrators on opposite sides of the target. This is consistent with the expectations from a wedge-like ionospheric structure responsible for direction dependent errors as described in Sect. 3.2.2. MV results in the smallest phase residuals (significantly smaller than PR_{2°) with almost none of the signatures for sunrise or systematic trends visible in PR, and are similar for both epochs. All of these are indicative of a superior performance on the mitigation of ionospheric errors regardless of the weather conditions. This is crucial for accurate single-

[5] The GPS ionospheric data comes from the US Total Electron Content Product Archive of the National Oceanic and Atmospheric Administration (NOAA). https://www.ngdc.noaa.gov/stp/IONO/USTEC/)

and multi-epoch astrometric analysis, as shown in the next section.

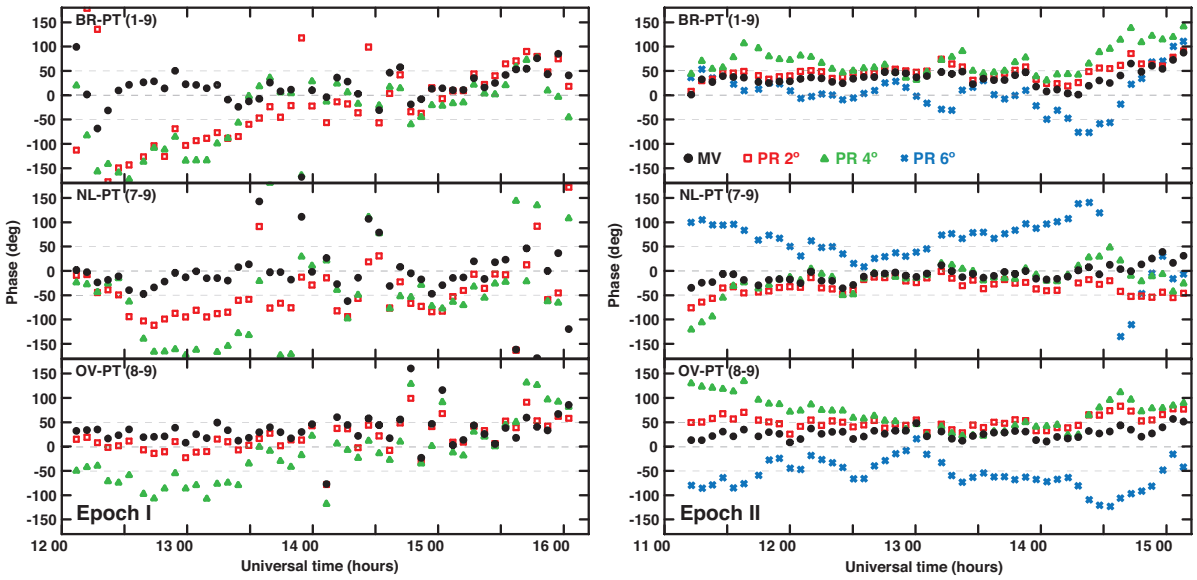

Figure 3.7. Calibrated visibility phases for C4 using MV (black dots) with three calibrators, and PR with a calibrator 2° (red squares), 4° (green triangles) and 6° (blue crosses, Epoch II only) away, on a subgroup of baselines, in Epoch I (left) and Epoch II (right).

Astrometric images. The calibrated visibilities are used to generate the final product of the analysis, the astrometric images, which convey the astrometric measurements presented in the next section. Fig. 3.10 shows the MVed image for the C4 quasar obtained using the three calibrators together and the three PRed images using a single calibrator ∼2°, 4°, and 6° away, for the two epochs. The image degradation arises from remaining short and long term residual phase variations in each analysis. A qualitative comparison suggests that the PRed images improve with closer angular separations, as expected; that the MV is similar to PR_{2° at both epochs, with MV slightly better at epoch I, under worse weather conditions. Fig. 3.11 shows the self calibrated maps of the observed quasars. For a quantitative comparison, Table 3.4 lists the peak brightness and rms noise values in the astrometric images along with the coherence losses (i.e. FFR) estimated with respect to the self calibrated images, for the two epochs of observations. The corresponding astrometric thermal noise errors, estimated as described in Sect. 3.2.2, are listed in Table 3.5. Nevertheless, as stated above, these estimates are not sensitive to residual systematic errors, which propagate into position shifts while maintaining the quality of the image. Those are better addressed by the repeatability errors, presented in the next section.

Astrometric Repeatability

Astrometry is performed directly on the images of quasar C4 shown in Fig. 3.10 by measuring the offset of the peak of brightness from the center of the map. This offset corresponds to the difference between the present measurements and the catalog positions used for correlation. Fig. 3.12a shows the astrometric measurements, or offsets, of the target quasar C4 using PR (analysis ID: PR_{2°, PR_{4°, PR_{6°) and MV (analysis ID: MV_{QSO}) at the two epochs of observations. Fig. 3.12b shows an expansion of the area around the MV measurements at the two epochs. The astrometric uncertainties in the plot are 1σ thermal noise error bars ($\sigma_{\mathrm{pos,thermal}}$) listed in Table 3.5.

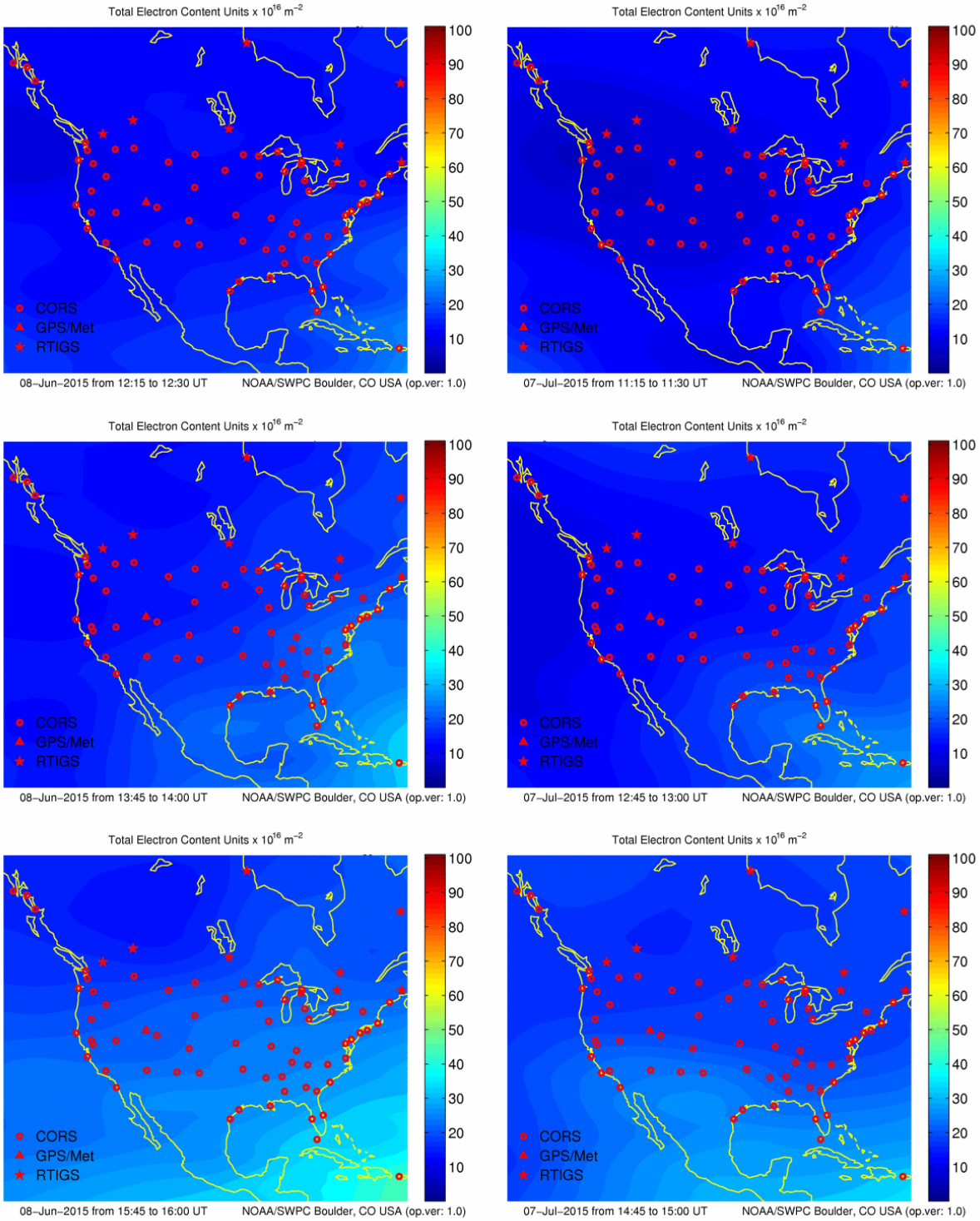

Figure 3.8. Maps of total electron content (TEC) over the United States, the site of the VLBA, derived from NOAA GPS measurements. Ionospheric conditions are shown at the beginning, middle and end of the observing sessions (from top to bottom), for Epoch I (left) and Epoch II (right). The gradual increase in the TEC values starting at the Caribbean is due to the diurnal solar motion, with sunrise times in the first half of the observing sessions.

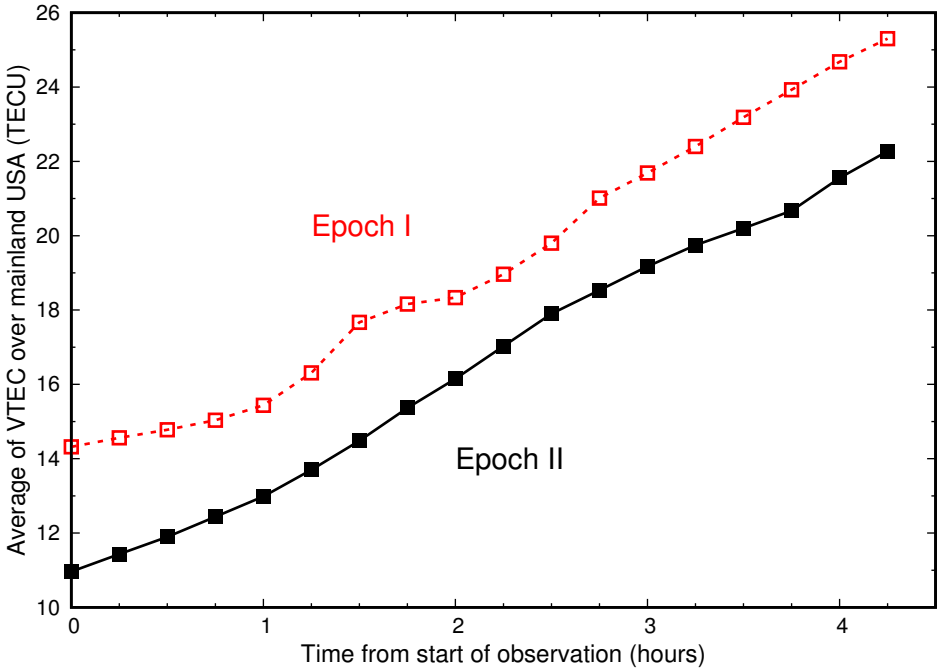

Figure 3.9. Average of VTEC content over the continental US during our observing session (only the region covered by GPS stations). The average values in Epoch I are probably larger as the observations were scheduled a bit later in the day. The smoother changes in Epoch II indicate a more stable ionosphere and better observing conditions.

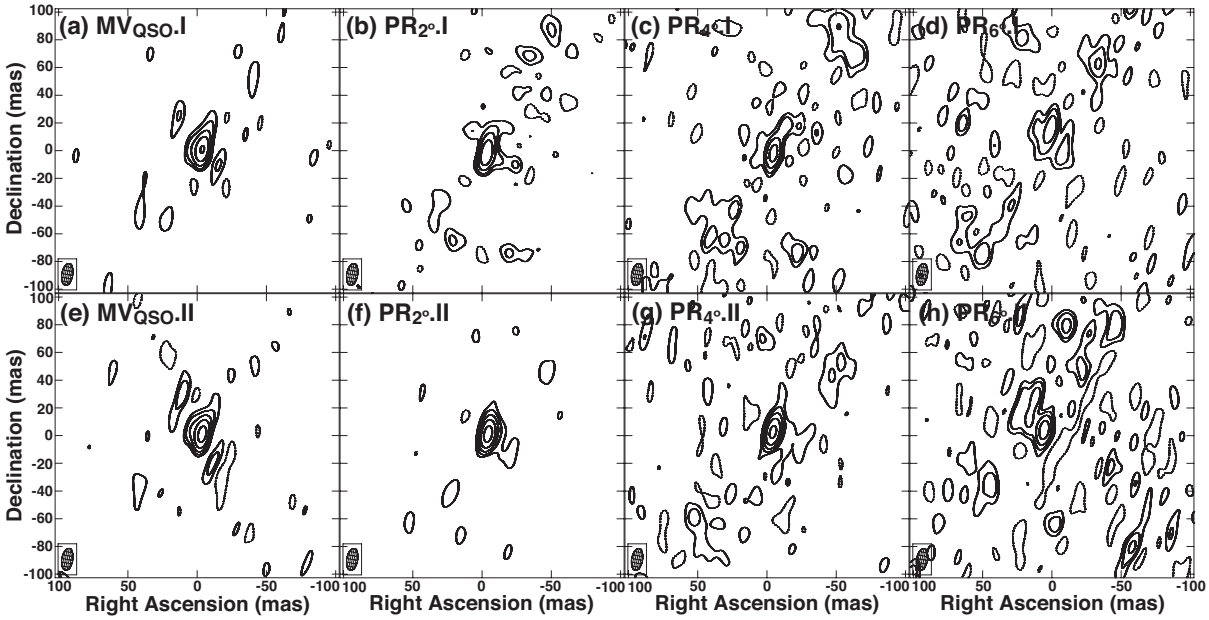

Figure 3.10. Astrometric images of C4 using the compared analyses. From left to right, MV, PR_{2°, PR_{4° and PR_{6°, for epoch I (upper row) and epoch II (lower row). The lowest intensity contour in all images are at 3σ level of the MV map and doubling thereafter. The images have been restored with the same beam: 8×16 mas with PA$=-10^\circ$. See Table 3.4 for values of peak brightness, rms noise and astrometric offsets in the images.

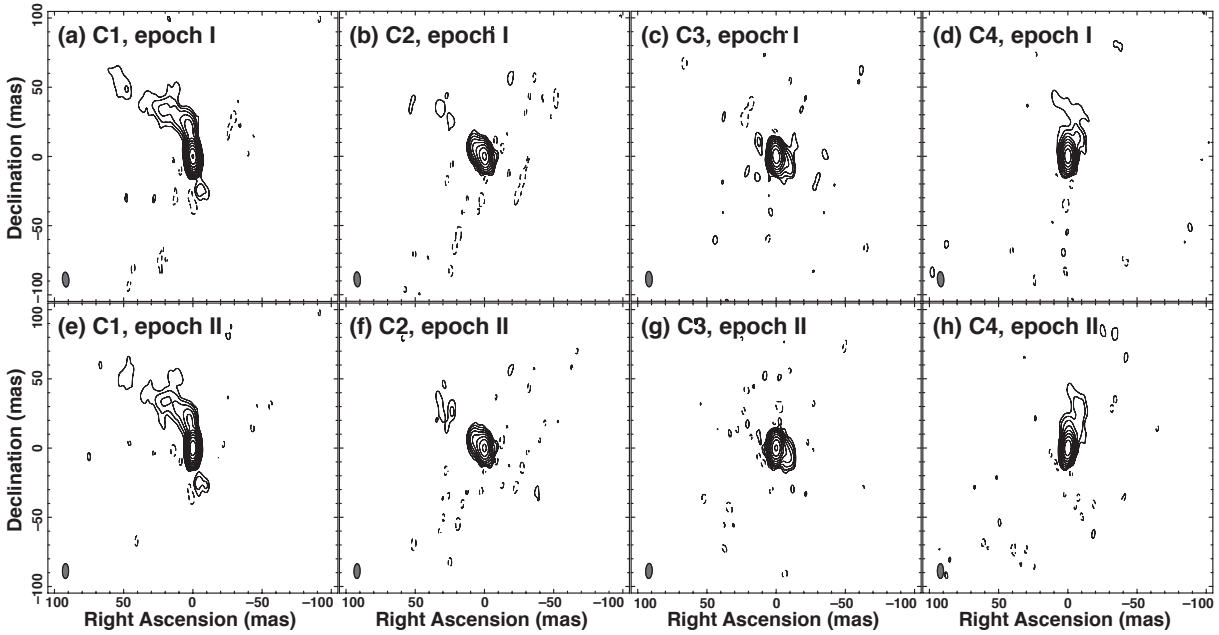

Figure 3.11. Self-calibrated maps of the observed quasars. Peak brightnesses are listed in Table 3.1. The lowest intensity contour is the 3σ level and doubling thereafter. Restoring beam is 8×16 mas with PA$=-10°$.

Note that, in general, while the PR and MV measurements at a given epoch are expected to differ, because they are tied to different reference points, the inter-epoch differences convey information on the source position changes (if any) undergone in the 1-month time span between the two epochs. For stationary sources, as it is the case for quasars, no or negligible position changes are expected. Therefore one can estimate the repeatability errors using the change in the measured offsets at the two epochs for a given technique. Table 3.5 lists the repeatability errors estimated as described in Sect. 3.2.2 which are an empirical estimate of the astrometric precision. It is immediately obvious that the repeatability errors are much larger for PR, compared to those for MV. Also, that the repeatability errors are larger than the thermal noise errors for PR; instead they are within the 1σ thermal noise error bars for MV.

Fig. 3.12c displays the repeatability errors as a function of source pair angular separations, for PR analysis.This linear trend is as expected from PR analysis, as closer angular separations provide a better atmospheric compensation. The MV repeatability errors are the smallest, more than one order of magnitude smaller than those for the closest pair with PR, and are equivalent to those from a very close pair of sources (i.e. close to zero angular separation) in PR analysis. It is worth highlighting that instead the MV and PR_{2° images are of similar quality and have similar FFR values. This underlines the insensitivity of the PRed images to large systematic errors. This underlines the superior quality of the calibration of atmospheric errors using multiple calibrators, compared to that achieved with a single calibrator with the same range of angular separations, and that MV analysis leads to higher precision astrometry. This is in agreement with the findings from our previous simulation studies, where we concluded that using multiple calibrator sources with MV resulted in one order of magnitude improvement compared to PR with a single calibrator (Jimenez-Monferrer et al., 2010; Dodson et al., 2013).

Fig. 3.12a also conveys qualitative information on the astrometric accuracy of the different calibration techniques since the observed quasars have well determined positions in the rfc2015b

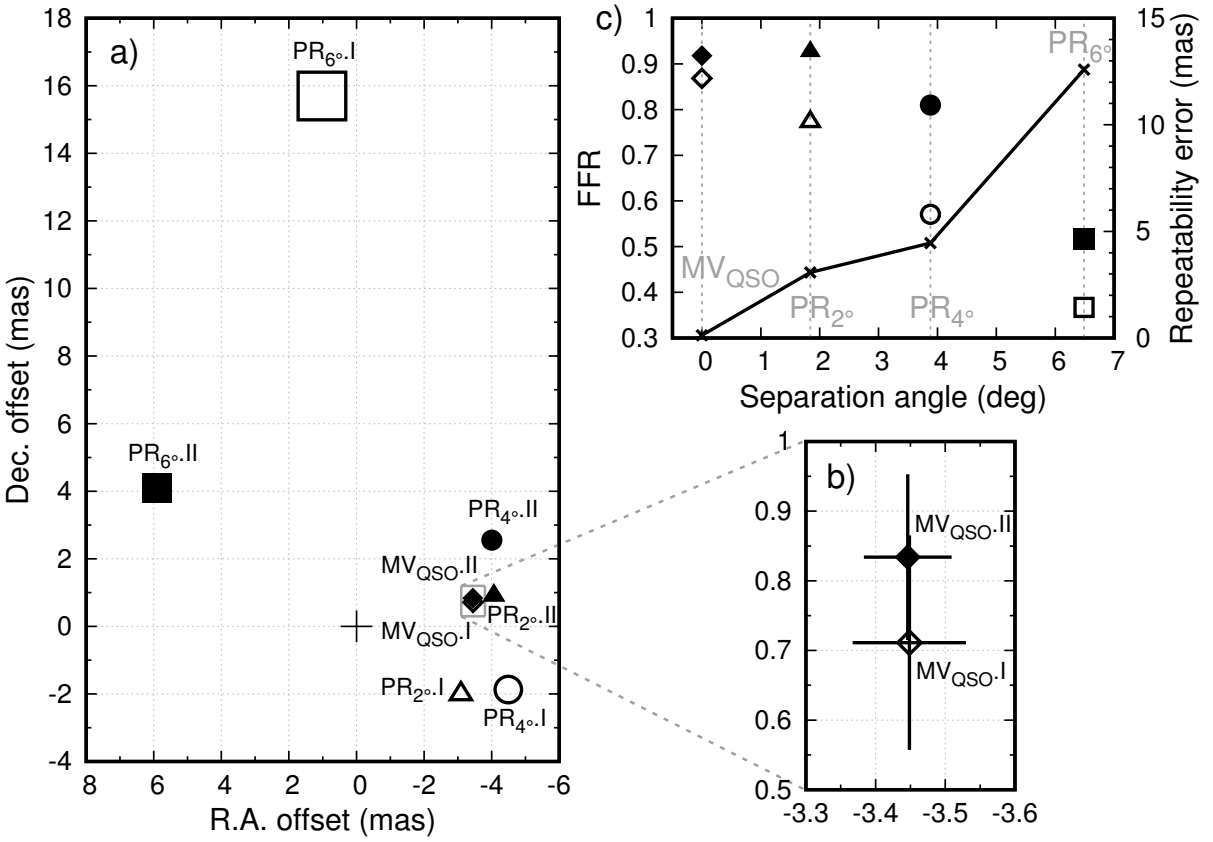

Figure 3.12. *a)* Astrometric offsets in the angular separations measured with MV, PR_{2°, PR_{4° and PR_{6° analyses (see Table 3.3 for description), from the observations of quasars at the two epochs, with respect to those in the VLBA radio fundamental catalog rfc2015b. The size of the plotted symbols corresponds to the estimated thermal noise error in each case (see Table 3.5). The labels describe the analysis ID and epoch of observations. *b)* Zoom for MV astrometric solutions. The error bars are the thermal noise errors. Both epochs agree within the error bars. *c)* Solid line shows the corresponding repeatability astrometric errors versus the angular separation between target and calibrator for PR analysis, and for an effective 0° separation for MV. Filled and empty symbols show the Flux Fractional Recovery quantity versus angular separation for MV (diamond), PR_{2° (triangle), PR_{4° (circle), and PR_{6° (square) analyses, for epoch I (empty) and epoch II (filled).

Epoch	Analysis ID	Sep. (deg)	Peak (mJy/beam)	rms (mJy/beam)	FFR (%)	Astrometric Offset Δ_{RA} (mas)	Δ_{DEC} (mas)
I	MV_{QSO}	~ 0.	64	1	87	-3.45	0.71
I	PR_{2°	1.8	57	1	77	-3.09	-2.02
I	PR_{4°	3.9	42	2	57	-4.49	-1.87
I	PR_{6°	6.5	27	2	37	1.02	15.70
II	MV_{QSO}	~ 0.	67	1	92	-3.45	0.83
II	PR_{2°	1.8	67	1	93	-4.06	0.90
II	PR_{4°	3.9	59	1	81	-4.01	2.55
II	PR_{6°	6.5	38	2	52	5.89	4.09

Table 3.4. Outcomes from astrometric analyses. Column 1 is the epoch of observations. Columns 2 and 3 are the analysis ID and source angular separation, respectively. Columns 4, 5 and 6 are the peak brightness, rms noise and Fractional Flux Recovery values measured from the astrometric images in Fig. 3.10, respectively. Columns 7 and 8 are the astrometric offsets of the peak of brightness in the astrometric images shown in Fig. 3.10 from the centre of the map; these are shown in Fig. 3.12a).

Analysis ID	$\sigma_{pos,thermal}$ (mas) Epoch I	Epoch II	$\sigma_{pos,rep}$ (mas) Δ'_{I-II}
MV_{QSO}	0.17	0.14	0.1
PR_{2°	0.19	0.11	2.7
PR_{4°	0.42	0.22	3.9
PR_{6°	0.75	0.44	11.2

Table 3.5. Empirically estimated astrometric errors for measurements presented in this chapter. Column 1 is the calibration strategy (see Table 3.3 for description). Columns 2 and 3 are the thermal noise errors for epochs I and II, respectively. They have been calculated using the values listed in Table 3.4 with a beam of 8×16 mas PA=-10°. Column 4 lists the repeatability errors, calculated from the astrometric offsets in Table 3.4 and corrected for bias for two epochs, with $\Delta'_{I-II} = \Delta_{I-II} \times \sqrt{2/\pi}$. See Section 3.2.2 for description of error analysis.

catalog. We expect offsets of no more than a few (~1–2) mas to account for differences between both measurements in all cases (see discussion in Sect. 3.2.2). Hence the magnitude of each of the astrometric offsets in Fig. 3.12a is indicative of the accuracy of that measurement and the method. PR offsets increase for larger source separations; MV results in the smallest offsets which indicates higher calibration accuracy. In fact, the magnitude of the accuracies is similar to the repeatability errors listed in Table 3.5.

Finally, the distribution of the measurements in Fig. 3.12a is also indicative of the spatial structure of the propagation medium being a planar surface. There is a resemblance between the geometric distribution of the three PR estimates at epoch I (i.e. PR_{2°.I,PR_{4°.I,PR_{6°.I) and epoch II (i.e. PR_{2°.II,PR_{4°.II,PR_{6°.II). Such distributions would arise from planar spatial structures in the propagation medium above each antenna, where the size and orientation of the triangles at each epoch depend on the weather conditions at a given epoch. The triangle for epoch I is more elongated than for epoch II. Moreover, both triangles appear rotated with respect to each other around a pivot point which is close to the MV measurements, which remain practically unchanged (within the thermal noise error bars) at both epochs, regardless of the weather conditions, as is expected from a quality calibration.

Subarray imaging analysis

This section is just a short demonstration of a new technique to detect systematic effects in the astrometry (Orosz et al., 2017b). A full explanation of its technical background is given later in Sect. 4.1.3 as well as demonstrating it on maser sources. Systematic errors are hard to detect as they introduce shifts in the position without degrading the resulting image quality. The presented technique tries to separate separate these two types of error sources, by imaging the calibrated visibilities with all possible three-antenna subarrays of the VLBA. The peak positions is then measured in the resulting maps, which are all coherent but shifted images of the same source. Comparing the positions determined from these subarrays can expose antennas affected by systematic errors. Figure 3.13 demonstrates the results from subarray imaging for C4, using all possible PR and MV calibration solutions.

The spread of the derived positions is related to random errors and it gets larger with increasing calibrator separations. In order to show how antennas can be related to shifts depending on calibration method and ionospheric conditions, BR (circles) and HN (triangles) were highlighted as being the most remote antennas in the continental VLBA (MK and SC had to be flagged out earlier). In PR_{6° and PR_{4° we do not see any particular pattern, but systematic shifts become visible in the PR_{2° and MV solutions due to the smaller scatter. Using the methods described in Asaki et al. (2007) and Orosz et al. (2017b), we expect residual ionospheric errors to be on the order of ∼0.1 mas for MV and ∼0.6 mas for PR_{2°, which are comparable to the shifts seen for BR in Epoch I and demonstrate the additional corrections in MV. However, the MV solutions also show a small peculiar offset for HN, almost identical in size and direction in both epochs, that is also visible in Epoch I of PR_{2° although in the opposite direction. Understanding this effect requires further study.

Astrometry on OH-maser source: MV vs. in-beam PR

In this section the astrometric results from PR with an in-beam calibrator are compared to MV with more distant calibrators, based on the analysis using the spectral line OH-maser as the target source (analysis IDs: $PR_{in-beam}$ and MV_{OH}, respectively, in Table 3.3). The $PR_{in-beam}$ analysis uses the simultaneous observations of C4 and the OH maser target source, 0.°4 away; the MV analysis uses the alternating observations between the target line source and the three (continuum) calibrators C1, C2 and C3, which are ∼2°, 4°, and 6° away. Fig. 3.14a shows the astrometric offsets estimated at epoch II, with respect to epoch I, for both analyses. This accounts for the different reference points in PR and MV and permits a direct comparison of the inter-epoch differences. The estimated thermal noise errors are $\sigma_{\mathrm{pos,thermal}}$∼0.5 mas and ∼1 mas in right ascension and declination, respectively. Note that, in this case, the inter-epoch differences trace the expected motion of the stellar target, due to the proper motion and parallax, during the 1 month interval between epochs. Hence, unlike the case of quasar-only analysis described in the section above, the astrometric changes between the two epochs are not a direct measure of the repeatability errors (and the precision of the method) and an extra step is required to eliminate the contribution from the motion of the source.

The proper motion and parallax of the OH maser target source was measured using a set of four in-beam phase referencing observing sessions spanning 1 year (Orosz et al., 2017b). These include the two epochs described in this paper, plus two additional epochs with a similar ob-

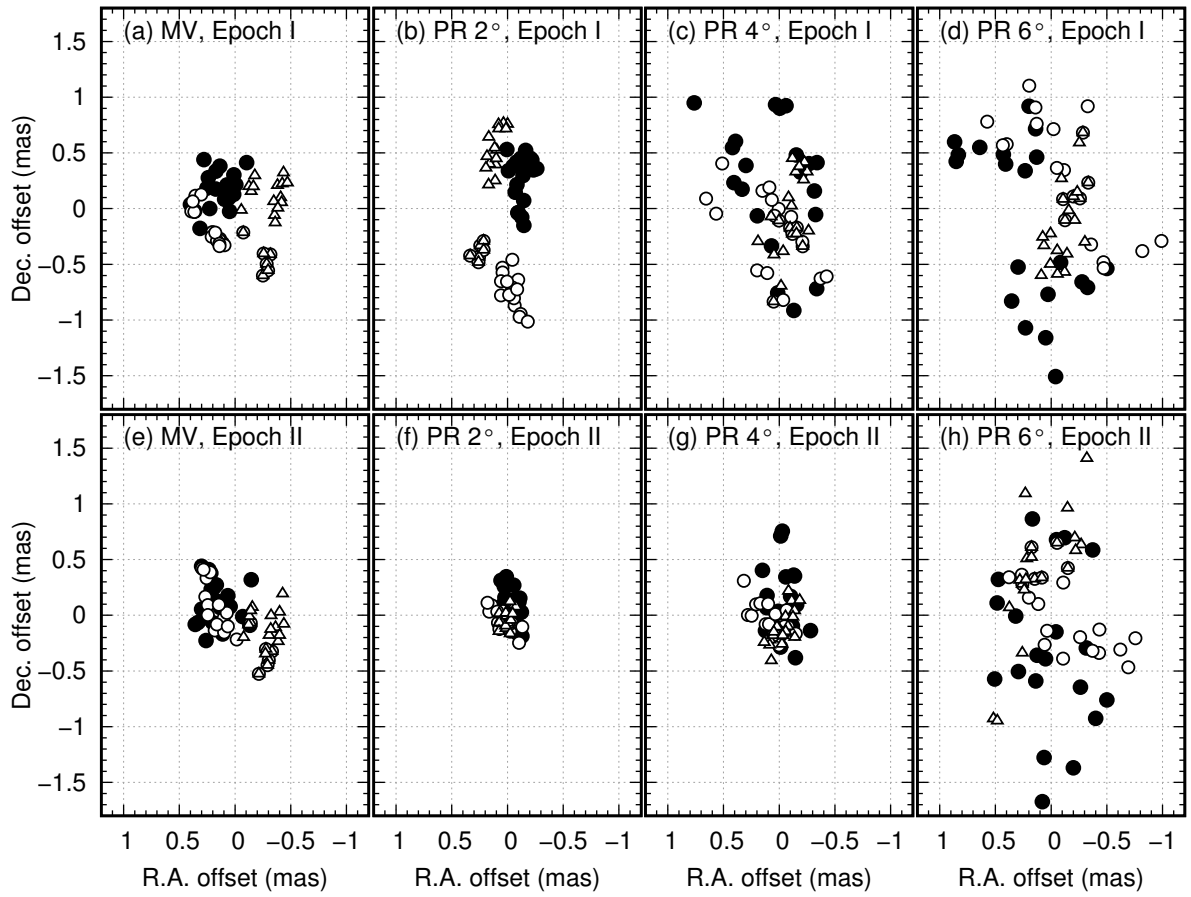

Figure 3.13. Positions of C4 (J0106+1300) in respective epochs using the various solutions, determined with all the 56 three-antenna subarrays of the continental VLBA (not incuding MK or SC). Open circles and triangles mark measurements that contain antennas BR and HN respectively. Offsets are relative to the mean positions.

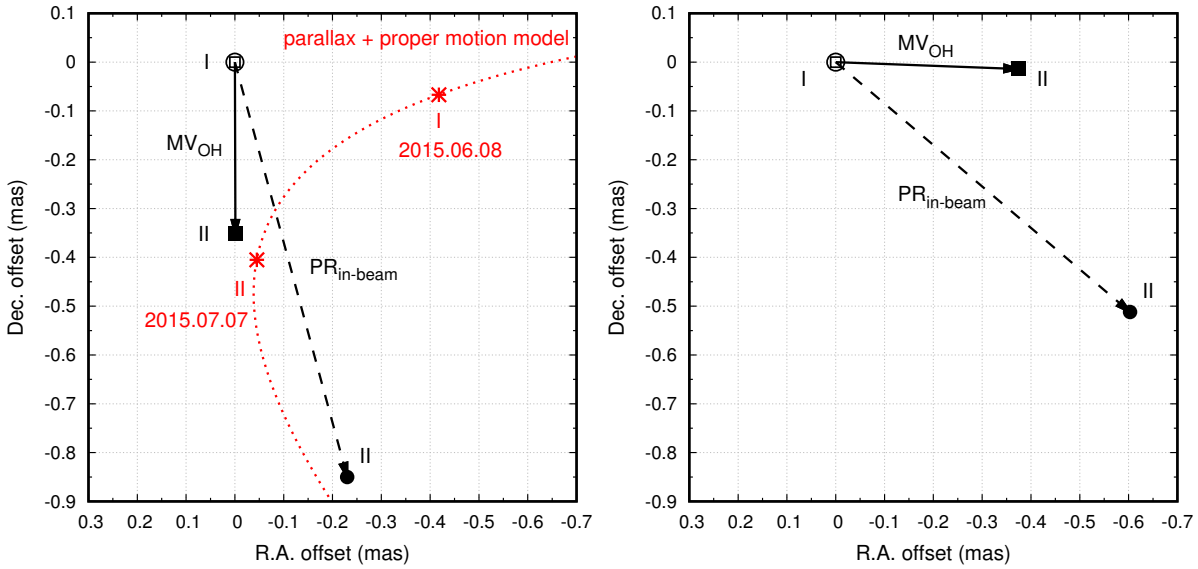

Figure 3.14. *(left)* Astrometric changes in the position of the line source OH measured with MV and PR$_{in-beam}$ at epoch II, with respect to epoch I. The estimated thermal noise errors are 0.5 mas and are not displayed. The labels describe the analysis ID and epoch of observations. Also shown is the expected apparent motion of the OH maser source between both epochs, due to the proper motion and parallax (see text). *(right)* Same as *left*, after correcting for the apparent motion of OH maser source due to the proper motion and parallax.

serving configuration, except for having longer duty cycle times (∼15 minutes) which prevented MV analysis. The measured parallax is $\pi = 2.9 \pm 0.8$ mas and the proper motion is $\mu(\alpha, \delta) = (-0.1 \pm 0.4$ mas yr^{-1}, -7.5 ± 0.7 mas yr$^{-1})$. Fig. 3.14b is same as Fig. 3.14a, after removing the contributions from the proper motion and parallax between epochs I and II, with the repeatability errors being $\sigma^{MV_{OH}}_{pos,rep} = 0.29$ mas for MV$_{OH}$ and $\sigma^{PR_{in-beam}}_{pos,rep} = 0.64$ mas for PR$_{in-beam}$. The repeatability errors for MV$_{OH}$ are half the magnitude for PR$_{in-beam}$, albeit based on more distant calibrators[6]. In this case all measurements agree within the thermal noise errors, which are larger for the case of a weak source.

3.2.4 Discussion and Conclusions

Demonstration of MultiView high precision astrometry at low frequencies

The ionospheric propagation effects are the main limitation to routinely achieving high precision astrometry at frequencies ∼<8 GHz, using state-of-the-art phase referencing methods developed for higher frequencies. This is due to the distinct direction dependent signature, which limits high precision measurements to cases when there is a suitable very close calibrator ∼ arcmins away. Combination of multiple calibrators around the target results in a significant reduction of the systematic astrometric errors, from the mitigation of the spatial structure effects, by using a bilinear (spatial) interpolation to estimate the calibration along the direction of the target source.

[6]Due to the small number of epochs and their sub-optimal spacing, several proper motion and parallax models agree with our measured astrometry (for more details, see Orosz et al., 2017b). Fig. 3.14 shows the model which gave the largest and most conservative repeatability errors. Using a slightly different model, the smallest measured repeatability errors were $\sigma^{MV_{OH}}_{pos,rep}$=0.17 mas and $\sigma^{PR_{in-beam}}_{pos,rep} = 0.44$ mas.

In this chapter, an empirical demonstration was presented of the superior mitigation of MV along with a comparative study with phase referencing analysis using a single source at a range of angular separations, including in-beam phase referencing. All the analysis have been carried out using the same VLBA observations at 1.6 GHz. The repeatability was used between two epochs of observations to provide an empirical estimate of the systematic astrometric errors, which are otherwise very difficult to quantify.

High precision MV astrometry of $\sim 100\ \mu$as was achieved in a single epoch of observations of quasars with calibrators at 2° and larger angular separations, effectively reaching the thermal noise limit of the observations. This corresponds to more than an order of magnitude improvement with respect to the precision achieved using PR with a single calibrator 2° away, which is $\sim$3 mas, due to the residual systematic errors in the analysis. This underlines the importance of correcting for the spatial structure of the ionospheric residuals. The comparative improvement can be interpreted as MV compensation being equivalent to that from PR with a single calibrator $\sim 10\times$ closer, in this case $\sim 0.2^\circ$ away, assuming a linear dependence between astrometric precision and target–calibrator angular separation. Also, the presented results indicate that there is a common limiting factor for accuracy and precision, namely the residual ionospheric propagation errors, and both are improved by a quality calibration as provided by MV.

The performance of MV calibration was also demonstrated in the case of a weak source using the observations of the OH maser source, and compared MV using 2°, 4° and 6° angular separations with in-beam PR using a calibrator $0.^\circ 4$ away. The repeatability errors are larger, as expected from lower SNR, but interestingly keep the same corresponding relative astrometric signature found in the analysis of the quasars. That is MV_{OH} calibration is a factor of two better with respect to $\mathrm{PR}_{in-beam}$ using a calibrator five times closer to the target. Therefore these observations have demonstrated the benefits of using multiple calibrators, with an improvement of more than one order of magnitude in astrometric precision in the present case, reaching the thermal limit of the observations of $\sim 100\mu$as. In general, MV is expected to be relevant for observations in the frequency regime where the ionospheric effects continue to be the dominant source of errors, that is, in observations up to $\sim$ 8 GHz. Finally, greater improvements are expected from increased sensitivity, and faster duty cycles, with maximum benefits from simultaneous observations and closer source distribution, to minimize the non-linear deviations of the actual ionospheric spatial structure above each antenna from a planar surface.

MV in the context of SKA and multi-beam instruments

Precise astrometric capability is of great importance in the SKA era. It is an SKA goal to achieve $10\,\mu$as astrometric accuracy at a single epoch of observations at $\sim$1.4 GHz (Paragi et al., 2015). The high sensitivity and long baselines of SKA VLBI observations will result in a much reduced thermal noise level and high spatial resolution. Therefore this goal is achievable as long as a sufficiently accurate ionospheric phase calibration strategy is in place. For a single calibrator source and PR techniques, the required angular separation to the target would be $\sim$ 1 arcmin (Paragi et al., 2015). This puts a very tight limit on the number of available calibrator sources, even at the SKA sensitivities (Godfrey et al., 2011). This constraint on the angular separation can be significantly relaxed, by using multiple calibrator sources and MV techniques, as suggested by the presented demonstration and previous simulation studies. Additionally, the multi-beam capability of SKA will allow for simultaneous observations of all sources and there-

fore eliminate the errors arising from short term phase fluctuations, which result in a reduction of coherence losses (i.e. characterized by the FFR quantity) and thermal noise errors, while improving overall performance. This applies to other instruments with multi-beam systems such as ASKAP, WSRT Apertif, Effelsberg in the 800–1800 MHz range or the prototype system at the Sardinia Radio telescope, currently operating with 5 beams in C-band but expected to expand both in frequency and number of beams. The shown demonstration includes three calibrators; note that the more calibrators the better, as this will allow the most accurate reconstruction of the atmospheric effects. Therefore it seems hopeful that MV can deliver the goal of 10 μas astrometry for many targets with SKA.

Other relevant scientific applications of MV

Near Field Cosmology. The presented case study used astrometric observations of a group of quasars in the role of targets and calibrators and an OH maser source in the ground state at 1.6 GHz. Scientific applications using such a group of sources applied to studies with the SKA of the nearby universe, including the Milky Way galaxy and the Local Group of galaxies are described in Imai et al. (2016). Although that case-study report discussed the scientific applications conservatively based on only in-beam PR astrometry, the shown results indicate that MV would provide further benefits.

Pulsars at 1.6 GHz. The empirically estimated MV astrometric accuracy of $\sim 100\,\mu$as at 1.6 GHz with VLBA observations, using calibrators more than $\sim 2^\circ$ away is at the state-of-the-art, only comparable with in-beam phase referencing observations with a calibrator $\sim$ 10s of arcminutes away (Deller et al., 2013, 2016). This improvement is expected to continue to apply at all angular scales. Hence, using three calibrators within the SKA-Mid antenna beams and MV will result in a further increase by one order of magnitude of the astrometric precision, extrapolating from the present comparative study. In general, allowing for larger angular separations makes it possible to select good calibrator sources, which are fundamental for multi-epoch studies. With the higher probabilities of finding suitable calibrators the general applicability is also highly increased. In some cases, such as pulsar observations in the galactic plane, it might even be desirable to use calibrators out of the plane to reduce the effect of scattering. This would be possible using MV.

Methanol masers at 6.7 GHz. High precision astrometry observations of methanol masers at 6.7 GHz hold the prospect to contribute to the successful program for 3D mapping of our Galaxy, as a complement to the precise water maser measurements (Reid et al., 2014). However the advanced PR strategies used at 22 GHz, in the tropospheric dominated regime, fail to provide high precision astrometry at 6.7 GHz, as this is in the ionospheric dominated regime. Therefore MV with fast source switching between sources, or simultaneous observations if possible, provides a strategy for superior calibration of the tropospheric and ionospheric errors resulting in precise astrometry.

4 | Astrometry of circumstellar hydroxyl masers

The previous chapter laid down the basics of VLBI astrometry, introduced possible error sources and a new technique to deal with these errors. From now on, we will concentrate on the application of OH maser astrometry to measure the proper motion and annual parallax to AGB stars, while also looking at various analysis methods to study systematic errors and other distance measurement methods involving OH masers. Finally, we explore some possible scenarios where AGB stellar distances can help further our understanding, mainly concentrating on the evolution of TP-AGBs and their Period–Luminosity relation, with also a brief outlook on utilizing AGB stars to probe the dynamics of the Milky Way.

4.1 Annual parallaxes of WX Psc and OH 138.0+7.2

Relative astrometry using VLBI has proven to be very successful for conducting trigonometric parallax measurements of maser (and also radio continuum) sources. Masers are excellent tracers of various environments related to the young and evolved stellar populations in the Milky Way Galaxy: HMSFRs, AGBs or their massive counterparts, RSGs. CH_3OH or H_2O masers at the relatively high radio frequencies of 12 and 22 GHz respectively are excellent for high-precision parallax measurements of HMSFRs at a $\sim$10 μas-level. This astrometric precision is achieved by using techniques that enable us to calibrate errors due to atmospheric effects. The geodetic blocks in VLBI observations (Reid et al., 2009) and the dual-beam system (Honma et al., 2008b) introduced in VERA are examples of such calibration techniques, both designed to address the dominant error sources above $\sim$10 GHz: the static (temporally stable and systematic) and dynamic (short-term turbulent and random) terms of the non-dispersive excess path delays caused by the troposphere, respectively.

Thanks to these calibration techniques, there have been a series of successful parallax measurements of AGB stars using mostly circumstellar H_2O masers (see Nakagawa et al., 2016, and references therein), with also a few results from SiO masers at 43 GHz (e.g. Min et al., 2014). H_2O masers have also been used to measure distances to a couple of post-AGB stars (Tafoya et al., 2011; Imai et al., 2011, 2013b) and RSGs (e.g. Asaki et al., 2010). However, H_2O masers are neither the strongest nor the most stable of the stellar masers for measuring the parallaxes of AGB stars. Instead, the strongest and most commonly found ones are the 1.6 GHz ground state OH masers, with thousands of known sources in the Milky Way Galaxy (Engels & Bunzel, 2015).

In the case of OH/IR stars – AGB stars heavily enshrouded in optically thick CSEs – OH masers are suitable for astrometry, especially the strongest line at 1612 MHz (e.g. Herman & Habing, 1985). These masers are located in the CSE at a distance of several hundred stellar radii from the central host star, expanding outward at terminal velocity. OH masers are pumped by infrared continuum background radiation to which stellar photons are converted by a heavy dust shell. As a result, 1612 MHz masers are excellent tracers of OH/IR stars: they are saturated, radially amplified and located in relatively calm regions, with strong features stable over decadal timescales (e.g. Etoka & Le Squeren, 2000).

However, VLBI astrometric observations at low frequencies (especially below approximately 2 GHz, i.e. L-band) are challenging to calibrate accurately due to the dominant ionospheric error contributions with typical residual path length errors of hundreds of centimeters at 1.6 GHz, compared to only a few centimeters from the troposphere. These dispersive terms are slowly changing spatial irregularities of plasma density in the atmosphere that cause serious direction dependent errors in astrometry. In turn, they drastically degrade the accuracy of conventional phase-referencing techniques by introducing systematic astrometric offsets into the observations.

Despite the challenges, there have been a few results of annual parallax measurements using OH masers. van Langevelde et al. (2000) and Vlemmings et al. (2003) used the two main-line OH masers at 1665 and 1667 MHz with mostly a conventional source-switching phase referencing strategy to measure parallaxes at a $\sim$1 mas-level precision. Vlemmings & van Langevelde (2007) refined and continued these measurements, using in-beam phase referencing – i.e. simultaneously observing the maser with a reference calibrator which lies within the same antenna beam – to push the astrometric precision firmly into the sub-mas regime. As we will also discuss in this chapter, the problems encountered at low frequencies can be mitigated by substantially decreasing the target–calibrator separations, from a few degrees down to a few tens of arcminutes.

Looking beyond spectral line VLBI, we see that L-band pulsar astrometry has flourished in the past decade, as those observations are not hindered by resolved spatial and velocity structures like OH masers. Since pulsars are continuum sources, wider bands, higher recording rates and pulsar gating – recording signals only during on-pulse periods – can be employed to significantly increase signal-to-noise ratios and, as a result, reduce (random noise-induced) astrometric errors. For the systematic errors, so far, there have been two main ionospheric calibration strategies for L-band continuum astrometry: measure and remove the dispersive component of the ionospheric delays by using wide-spread bands to detect its frequency-dependent curvature (Brisken et al., 2000, 2002); or use in-beam astrometry to almost completely remove dynamic (random) and mitigate static (systematic) error terms (Chatterjee et al., 2001, 2009). Deller et al. (2013, 2016) demonstrated that by using in-beam calibrators with careful scheduling and data reduction, it is possible to measure parallaxes at a $\sim$10 μas-level precision despite the low frequency.

An important side note is that ionospheric errors are not only a problem for L-band astrometry, but can dominate the error budget even at 5 GHz (see e.g. Krishnan et al., 2015; Kirsten et al., 2015). In addition, in-beam astrometry can be limited by the availability of suitable calibrators, and by residual systematic errors in the measurements due to non-zero source separations. Here comes into play the technique demonstrated in Sect. 3.2: MultiView, an alternative multi-calibrator approach (Rioja et al., 2009; Dodson et al., 2013) that can fully remove even the

effects of the static ionosphere and make astrometry completely free of systematic errors (Rioja et al., 2017). MultiView might hold the promise for future observations, however, the main focus of this chapter will be exploring the limits of traditional in-beam maser astrometry at low frequencies.

In this chapter, we are going to look at VLBI observations of 1612 MHz OH masers to measure the trigonometric parallaxes and proper motions of two long-period variable OH/IR stars, WX Psc and OH 138.0+7.2. Their respective pulsation periods are 650 and 1410 days (Engels et al., 2015), and both exhibit high mass loss rates of $\sim 10^{-5}$ $M_\odot$ yr^{-1} (calculated based on the method in Goldman et al., 2017). The VLBI observations are described in Sect. 4.1.1, then the flow of data reduction and maser detections in Sect. 4.1.2. A comprehensive astrometric error analysis is conducted in Sect. 4.1.3, describing the different error terms and their effects on the VLBI measurements. A new method is introduced to try to identify systematic errors and estimate the uncertainties in astrometric measurements. Parallax and proper motion results are discussed in Sect. 4.1.4, along with a comparison to distances derived by the phase-lag technique (e.g. van Langevelde et al., 1990).

4.1.1 Observations

Observations were conducted with the VLBA of two OH/IR stars, WX Psc (also known as IRC +10011 or OH 128.6−50.1) and OH 138.0+7.2 (hereafter abbreviated to OH138). Table 4.1 lists basic details on the target maser sources and calibrators used. The target sources were selected from the "Nanay 1612 MHz monitoring of OH/IR stars" project[1] (Engels et al., 2015), based on having calibrators in the same VLBA beam with precise and reliable positions[2], i.e. within 0.°7 of the OH maser sources in the present case. Also, only double-peaked OH sources were considered, which already had their periods and phase-lag distances measured.

Table 4.1. List of observed sources.

Target	Period (days)	V_{LSR} (km s^{-1})	Calibrator (J2000)	ID	Right ascension (h m s)	Declination (° ′ ″)	Sep. (°)	$S_{1.6GHz}$ (mJy b^{-1})
WX Psc	650	8.9	J0106+1300	C_{ib}	01 06 33.35651	13 00 02.6039	0.40	70
			J0121+1149	C_1/FF	01 21 41.59504	11 49 50.4130	3.81	2100
OH138	1410	−37.7	J0322+6610	C_{ib}	03 22 27.22883	66 10 28.3005	0.70	750
			J0257+6556	C_1	02 57 01.34302	65 56 35.4270	2.92	270
			J0102+5824	FF	01 02 45.76238	58 24 11.1366	18.74	1300

Notes. For the stellar coordinates refer to Sect. 4.1.2, while for the precise OH maser offsets to Table 4.4. Stellar pulsation periods are from the "Nanay 1612 MHz monitoring of OH/IR stars" project. Calibrators were selected using the Astrogeo Catalog and their coordinates are accurate to $\lesssim$0.3 mas. Systemic velocities and $S_{1.6GHz}$ flux densities were measured using the VLBA observations. Calibrator IDs refer to Fig. 4.1 and go as follows: C_{ib}= in-beam; C_1=secondary; FF=fringe finder.

Each source was observed at four epochs over a period of one year. The details of the observing sessions are given in Table 4.2, whereas the source scan pattern on the sky is shown in Fig. 4.1.

[1]Project home: www.hs.uni-hamburg.de/nrt-monitoring

[2]Calibrators with status "C" in the Astrogeo Catalog (astrogeo.org).

The sessions were scheduled near the peaks of the sinusoidal parallax signatures to maximize the sensitivity for parallax detection and ensure that we can separate the linear proper motions from the parallactic modulations. The desired sampling was only partially achieved due to failed observing epochs and other technical difficulties. All observations are publicly available from the NRAO VLBA archive under project codes BO047A and BO047B.

Table 4.2. Summary of observing sessions conducted with the VLBA.

Target	Epoch	Date (DOY)	MJD (days)	UT range (day/hh:mm)	Project code	Flagged data	Remarks
WX Psc	I	2014 Aug 01 (213)	56870	0/09:32−0/13:33	BO047A6	LA	no FD
	II	2015 Feb 17 (048)	57070	0/20:22−1/00:22	BO047A3	MK, SC	
	III	2015 Jun 08 (159)	57181	0/12:06−0/16:06	BO047A7	MK, SC	
	IV	2015 Jul 07 (188)	57210	0/11:12−0/15:12	BO047A4	MK, SC	
OH138	I	2014 Feb 16 (047)	56704	0/22:25−1/02:26	BO047B1	MK	
	II	2014 May 07 (127)	56784	0/18:40−0/22:40	BO047B2	KP, PT	no NL
	III	2014 Aug 07 (219)	56876	0/11:08−0/15:08	BO047B3	KP	
	IV	2015 Feb 22 (053)	57075	0/22:02−1/02:02	BO047B4	SC	

Notes. Flags refer to data from antennas not used in the astrometry, which were identified using methods described in Sect. **??**. In the NRAO archive WX Psc has several failed epochs due to recording or correlation problems: BO047A1, A5, & A7.
VLBA stations. BR=Brewster, WA; FD=Fort Davis, TX; HN=Hancock, NH; KP=Kitt Peak, AZ; LA=Los Alamos, NM; MK=Mauna Kea, HI; NL=North Liberty, IA; OV=Owens Valley, CA; PT=Pie Town, NM; SC=Saint Croix, VI

Each observing session was 4 h long to ensure sufficient (u, v) coverage and sensitivity, spending ∼70% of the time on the in-beam calibrator (C_{ib}) and OH maser pairs with intermittent observations of fringe finders (FF) in every 2 hours and bright secondary calibrators (C_1) in every 15 min. For the target scans, antennas were pointed halfway between the OH maser and C_{ib} positions, except for Epochs I–II of the WX Psc sessions, where the pointing center was the OH maser source. The 2-bit quantized signals were recorded on Mark5C units in dual circular polarization with 128 Mbps using 4 intermediate frequency (IF) bands, each with a bandwidth of 4 MHz. The IFs were spread out over 300 MHz, centered around the four ground-state OH maser lines of 1612, 1665, 1667, 1720 MHz and the H I line at 1420 MHz. Each band had a channel spacing of 1.95 kHz, corresponding to a velocity resolution of 0.36 km s^{-1}. Note that for the last two epochs of WX Psc (BO047A7, & A4) a slightly modified observing setup was used for parallel investigations of high-precision astrometry at L-band (see Sect. 3.2 and Rioja et al., 2017). The on-source time on the target was decreased to 40%; the switching cycle to C_1 (and two other calibrators) was decreased to 5 min and the IF bandwidths were increased to 8 MHz (256 Mbps recording rate), but keeping the same spectral resolution. The changed setup did not affect the in-beam parallax measurements.

Since the masers were always observed simultaneously with the C_{ib} phase reference calibrators in the same primary beam, all bands were correlated with VLBA-DiFX (Deller et al., 2007, 2011) in a single run using two phase centers set to the maser and C_{ib} calibrator positions. Phase tracking centers for the calibrators were set to the coordinates described in Table 4.1, whereas for the OH maser targets the following a-priori J2000.0 positions were used during correlation: $(\alpha, \delta)^{\text{a priori}}_{\text{WX Psc}}$=($01^{\text{h}}06^{\text{m}}25\overset{\text{s}}{.}98$,+12°35′53″.0) and $(\alpha, \delta)^{\text{a priori}}_{\text{OH138}}$=($03^{\text{h}}25^{\text{m}}08\overset{\text{s}}{.}80$,+65°32′07″.0). For de-

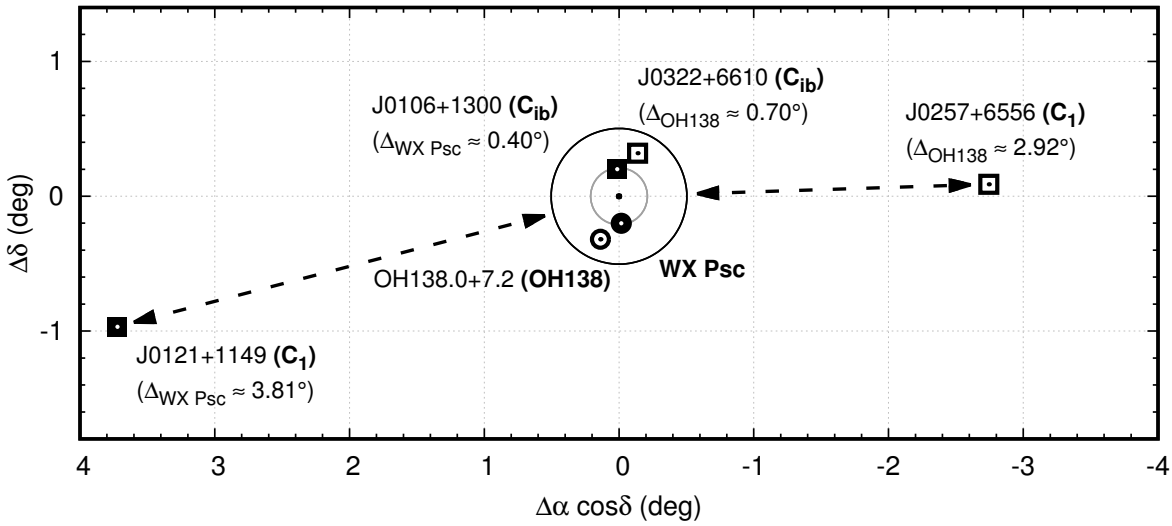

Figure 4.1. Observing setup of the astrometric measurements for both targets plotted together. Solid and open symbols represent the sources associated with the two different monitoring campaigns of WX Psc and OH138, respectively. The target masers are marked as circles and the calibrators as squares. Angles in parentheses show the separation between the respective targets and calibrators. The two concentric circles represent the half-power beamwidth and full beamwidth of the VLBA. Dashed arrows denote source switching (with 5–15 min cycles). Coordinates are relative to the target pointing centers, different for each campaign.

tails on the observations and correlator output, refer to the VLBA File Server[3].

4.1.2 Data Reduction and Maser Detections

The data analysis was carried out using the AIPS package with an in-beam phase referencing strategy. Flux density calibration was performed using system temperatures and gain information recorded at each station. The Earth orientation parameters from the VLBA correlator were refined by the U.S. Naval Observatory final solutions. Initial ionospheric delay corrections were performed using the NASA Jet Propulsion Laboratory IONEX files, which contain zenith TEC maps derived from global navigation satellite system observations. Finally, phases were corrected for parallactic angle effects before phase referencing.

After flagging channels contaminated by radio-frequency interference, instrumental phase calibration was performed using single FF calibrator scans with the phase rates zeroed. Next, scans on C_1 were used to determine the group delays, phase rates and bandpass characteristics. Fringe-fitting was performed by averaging polarizations, as Stokes V values were always less than ∼10% of Stokes I, making the difference between polarizations negligible (see Fig. 4.2). After applying this calibration to the Maser–C_{ib} pair, the final phase calibration solutions were obtained using C_{ib} (with IFs and polarizations averaged) and transferred to all channels in the maser scans. Thus WX Psc and OH138 were effectively phase referenced to their respective in-beam calibrators. Finally, phases were rotated to shift the phase-

[3]VLBA File Server: www.vlba.nrao.edu/astro/VOBS/astronomy

tracking center to the vicinity of the maser emission before imaging. The shifted J2000.0 phase-tracking centers used for astrometry are: $(\alpha, \delta)^{\rm shifted}_{\rm WX\ Psc}$=(01$^{\rm h}06^{\rm m}26^{\rm s}$.02574,+12°35′52″.8242) and $(\alpha, \delta)^{\rm shifted}_{\rm OH138}$=(03$^{\rm h}25^{\rm m}08^{\rm s}$.42975,+65°32′07″.0900).

Though the in-beam phase referencing observations were affected by the primary beam attenuation of the antennas, a correction scheme was not applied in the present observations. As a result, the flux density scales mentioned in this chapter are systematically lower than the true values. Using an Airy disk model presented in Middelberg et al. (2013) with an antenna diameter of D=25.47 m, the estimated amplitudes of WX Psc and J0106+1300 are lower by ∼47%, and those of OH138 and J0322+6610 are lower by ∼90%. Uncalibrated amplitudes do not seriously affect the astrometric measurements, because the phase pattern in the primary beam is expected not to have a significant systematic offset and also the resulting instrumental error is believed to be constant throughout our observing sessions. However, in order to minimize possible error sources and achieve better signal-to-noise ratios, proper flux density corrections should be applied in future in-beam astrometric observations by adopting a suitable primary beam model and beam squint corrections as done in Middelberg et al. (2013).

For both OH/IR stars all four ground-state OH maser transitions were observed, but only the double-peaked 1612 MHz satellite lines could be detected. The full resolution VLBA spectra of the 1612 MHz OH masers are shown in Fig. 4.2. In both profiles, the blueshifted features relative to the stellar systemic velocities have peak flux densities of ∼0.2 Jy, compared to ∼20 Jy from single dish observations with, e.g, the NRT, meaning only ∼1% of the total maser emission could be recovered from the OH regions. The redshifted features have a similar flux density recovery percentage for WX Psc, but are almost completely missing for OH138, perhaps due to more serious foreground scattering from the circumstellar envelope. However, in all cases maser emission on baselines longer than ∼4000 km are resolved out significantly for both the blue- and redshifted regions, similar to that seen in Imai et al. (2013a).

4.1.3 Astrometric Error Analysis

Theoretical Predictions

The dominant error sources after in-beam phase referencing are composed of various components of uncompensated atmospheric terms, and additional contributions from source/velocity structures and thermal noise (Reid & Honma, 2014). Since the in-beam calibrators are observed simultaneously in the same beam with the maser targets, the derived phase solutions can be directly applied to the masers and do not have to be interpolated in time between the calibrator scans. This mitigates the effects of temporal phase fluctuations, a dynamic term causing random errors in the astrometry. The small target–calibrator separations also reduce excess path errors.

Given the present observing parameters (1.6 GHz, 0 min switching time due to simultaneous observations, 0°.4–0°.7 target–calibrator separations), the expected errors from the static and dynamic components of the troposphere and ionosphere can be estimated (Asaki et al., 2007), by assuming a typical zenith path error of 3 cm (Reid et al., 1999), a 6 TECU uncertainty[4] in the adopted ionospheric maps (Ho et al., 1997), and a typical zenith angle of 45°. This predicts,

[4]TEC Unit; 1 TECU = 10^{16} electrons m^{-2}

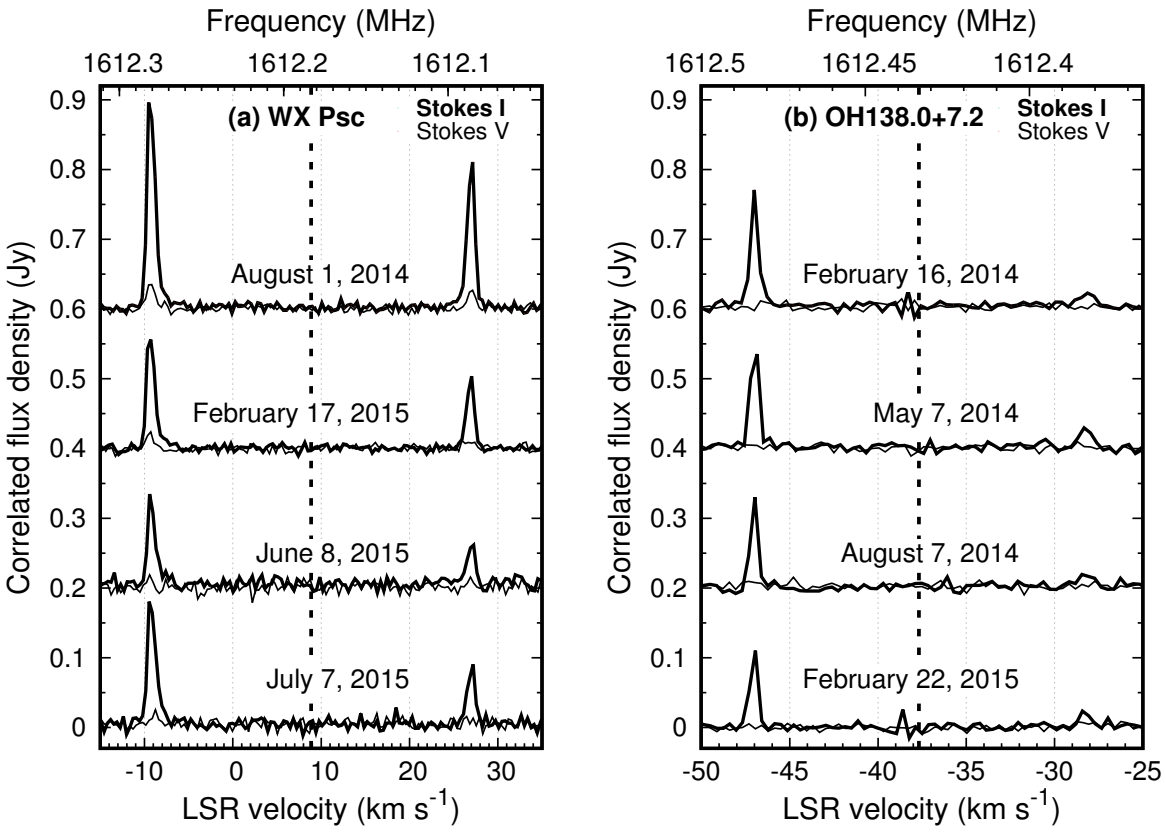

Figure 4.2. Scalar averaged cross-power spectra of the 1612 MHz OH maser emission for each epoch towards (a) WX Psc and (b) OH138. Thick and thin lines denote the Stokes I (total intensity) and V (degree of circular polarization) parameters, respectively. The spectra are unsmoothed and have a channel spacing of 1.95 kHz (0.36 km s^{-1}). Maser spots used for the parallax fitting are located in the brighter blueshifted peaks. Thick dashed lines mark the systemic velocities, calculated by averaging the strongest blue- and redshifted maser channels from all epochs. Spectra of different epochs have been shifted along the vertical axis for clarity.

per baseline, a dynamic ionospheric phase error of 3° / 5°, and a static ionospheric phase error of 16° / 28° for WX Psc / OH138. Due to the low frequency, the non-dispersive tropospheric phase errors are negligible; less than 1° per baseline.

The biggest residual errors in L-band are related to *spatial* static terms, direction dependent systematic errors from the inadequate modeling of the ionospheric sky-plane TEC distribution. This means that reducing the target–calibrator separation is of utmost importance in mitigating atmospheric errors in low-frequency VLBI astrometry. Also, even with in-beam phase referencing the dynamic terms from ionospheric phase fluctuations are not zero. This is because the traveling waves causing the temporal disturbances in the ionosphere have spatial scales of hundreds of kilometers, which again reflect as residual errors due to the non-zero target–calibrator separations. Assuming these components are independent and adding them in quadrature, the total atmospheric phase errors per baseline are estimated to be 16° / 29° for WX Psc / OH138. These $\phi_{\rm atmo}$ phase errors per baseline can be roughly converted to $\sigma_{\rm atmo}$ astrometric errors in the VLBA maps as $\sigma_{\rm atmo} \approx (\phi^{[\circ]}_{\rm atmo}/360^\circ) \cdot (\theta/\sqrt{N})$, where θ is the size of the synthesized beam and N is the number of stations in the array. Using N=8 and beam sizes described in Sect. 4.1.4, the total atmospheric errors in the presented in-beam astrometry are estimated to be approximately 0.3 mas / 0.4 mas for WX Psc / OH138, dominated by the effects of the static ionosphere. In

bad ionospheric conditions (i.e. having larger residual TEC values), deviations even as large as ∼0.7 mas can be expected.

Contribution from the target source structure to systematic astrometric errors is hard to predict, due to the variable behavior in the spatial and velocity structures of masers, and the possibility of multiple maser spots blending together. In the present case, OH maser spots used for the astrometric measurements seem to show complex spatial structures at lower resolutions when using a (u, v) taper of 13 Mλ (corresponding to baselines of ∼2000 km). However, when using the full resolution of the VLBA, only compact albeit not completely unresolved emission is detected. The systematic effects caused by the maser velocity structure are kept to a minimum by fitting the parallax using individual spots with the same velocity between epochs. Feature fitting is not feasible due to the few detected spots in each feature[5].

Astrometric errors from the image thermal noise are approximated as $\sigma_{\rm therm} \approx 0.5 \cdot (\theta/{\rm SNR})$, where θ is the size of the synthesized beam in case the source is unresolved, and SNR is the signal-to-noise ratio in the VLBA maps. The trade-off of limiting the astrometric fitting to the most compact parts of the OH maser emission – as an effort to reduce systematic effects from source structure – is a reduced SNR and thus a larger thermal noise component in the total astrometric error budget. Fortunately, the thermal noise is a random error source, so it has a more benign effect on the parallax measurements than leaving possible systematic errors in our datasets. However, this highlights one of the major difficulties in low-frequency astrometry. As $\sigma_{\rm therm} \propto \nu^{-1}$, where ν is frequency, the intrinsic limit of astrometry is lower than for CH_3OH or H_2O masers at higher frequencies.

The astrometric errors are quantitatively investigated not only by the analytical method described above, but also by simulating 1.6 GHz VLBA observations with ARIS (Asaki et al., 2007). Input parameters are adopted based on the present observation parameters and typical error values in VLBI observations: the target source is a single circular Gaussian component with a full width at half maximum of 10 mas and a maximum peak of 0.4–0.8 Jy in 1.95 kHz bandwidth. The reference sources for WX Psc and OH138 are J0106+1300 and J0322+6610 with flux densities of 0.07 Jy and 0.75 Jy in 32 MHz bandwidths, respectively. Because the above source strengths were assigned by referring to the data reduction results, the effects of primary beam attenuation were not considered. Imaging was conducted without MK and SC as described in Sect. 4.1.4. A total of 200 samples were simulated with astrometric errors estimated as the position offsets in RA and Dec from the phase tracking centers that contained 67% of the simulated positions.

The obtained astrometric errors from the simulations are 1.2 / 0.7 mas for WX Psc / OH138 in the case of a 0.6 Jy target Gaussian component, showing good consistency with the observation results (see Sect. **??**). The ARIS simulations show that despite the smaller target–calibrator separation, the astrometric errors of WX Psc can be worse than that of OH138 mainly because the reference source of WX Psc is weaker. Although transferred errors from calibrator structure can be ruled out as their structures were modeled before phase referencing, the thermal noise in the transferred visibility phase solutions from the weaker J0106+1300 to WX Psc is higher than in the case of J0322+6610 and OH138. The simulations also show that the astrometric errors are particularly sensitive to the peak value of the target Gaussian component: the astrometric error for a maximum peak of 0.4 Jy is a factor of ∼1.6 worse than for a maximum peak of 0.6 Jy,

[5] A maser spot refers to an individual maser brightness peak imaged in one spectral channel, and a maser feature refers to a group of spots which are considered to relate to the same physical maser cloud.

while the error for a maximum peak of 0.8 Jy is a factor of ∼1.3 better than for a maximum peak of 0.6 Jy. These errors can be different from epoch to epoch as the maser source strength varies.

The same simulations were repeated with the ionospheric model errors turned off, obtaining astrometric errors of 1.0 / 0.4 mas for WX Psc / OH138 for a maximum peak of 0.6 Jy. Comparing the two sets of simulations, the contribution of the ionospheric model error to the astrometric measurements was found to be ∼0.6 mas, which is consistent with the previous analytical estimates. We can also see that the limited bandwidth on the calibrators is a major contributor to the total error budget, which can be avoided in future observations by using larger total bandwidths for an increased continuum sensitivity. The sizes of datasets can be kept manageable by using several correlator passes and spectral "zooming", i.e. correlating all scans with a coarse resolution on the full bandwidth and the maser scans with a high resolution on a narrow bandwidth containing the spectral features. This feature is routinely available on both DiFX (Deller et al., 2011) and SFXC (Keimpema et al., 2015) correlators used at most VLBI arrays.

Empirical Errors from Subarray Imaging

As discussed previously, astrometric errors are composed of systematic and random errors. Because the former can yield systematic shifts in the measured maser positions, their identification is crucial for *accurate* astrometry. We can try to do this by imaging the strongest maser channel for each source with all possible three-antenna subarrays of the VLBA using the automated CLEAN procedure in AIPS, then measure the position of the peak in each resulting map with the verb MAXFIT[6] (see Fig. 4.3). By limiting the imaging to three antennas, each with an independent static ionospheric error, coherent but shifted images are formed of these subsets of data. Therefore, comparing the maser positions determined from these subarrays clearly expose the antennas that are contaminated by systematic errors, because their subarray images will also be affected and shifted systematically.

Looking at Fig. 4.3, it is clear that the subarray imaging worked better for OH138, which has a strong and compact maser spot, and seems less conclusive for WX Psc where the detected emission is more resolved and much weaker (see Sect. 4.1.4). In most cases, the distribution of the derived positions is elongated in declination, which is due to the geometry of the VLBA. Among the 120 possible subarrays the majority are dominated by East–West baselines, which yield poorer angular resolution in the North–South direction. This is just a random effect which does not skew the astrometric results (see Fig. 4.3a,c,e–h). Next, the measured patterns are discussed, with the specific sessions and epochs shown in bold.

OH138 session Epochs I–IV. Systematic shifts could be found and linked to specific antennas (Epoch I: MK in RA; Epoch II: PT and KP in positive and negative Dec, respectively; Epoch III: KP in Dec; Epoch IV: SC in RA). The size of these shifts are approx. 0.5–1 mas, which agree with the expectations for the static ionospheric error contributions. While substantial offsets found in the case of MK and SC are possible due to the long baselines and difference in antenna elevations, it comes as a surprise that some of the core southwestern antennas (FD, KP, LA, OV, PT) would also be affected by ionospheric model errors to such a degree.

[6]For measuring the peak positions, the Gaussian model fitting of IMFIT/JMFIT, the quadratic function fitting of MAXFIT and simply selecting the brightest pixel with IMSTAT were compared. As long as the mapped area was a few times larger than the fitted maser spot and the pixel sizes were adequately small compared to the synthesized beam – in our case 0.1×0.1 mas – all three approaches produced nearly identical results.

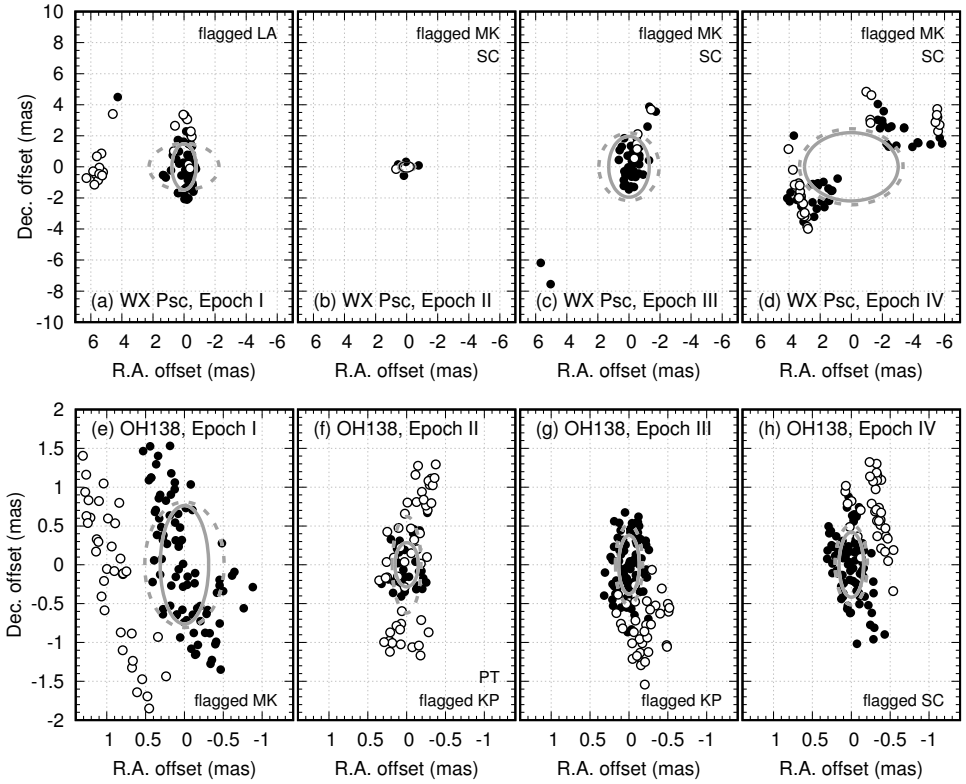

Figure 4.3. Fitted positions of the brightest maser spot toward (a)–(d) WX Psc and (e)–(h) OH138 in respective epochs, which are determined using all (≤120) three-antenna subarrays of the VLBA. Open circles mark measurements from triangles that contain antennas flagged in the final astrometric solutions. Offsets are relative to the mean positions derived from the retained data and shifted to zero (filled circles). Dashed and solid ellipses show, respectively, the 1σ contour of unweighted Gaussian models fitted to the measured peak positions before and after flagging the indicated antennas. Ellipses have been shifted to the center to make them easier to compare.

Dodson et al. (2017) found that under normal conditions the typical ΔTEC model differences between VLBA antennas on the mainland US are of the order of 1 TECU. After the phase referencing corrections with a calibrator $\lesssim$1°away, the residual systematic differences would be $\lesssim$1 TECU×sin(1°)≈0.02 TECU. These would cause systematic phase errors of $\lesssim$6°(Asaki et al., 2007), which translate to $\lesssim$1 mas astrometric errors for 600 km baselines, i.e. the average separation between the core antennas of the VLBA. Although this seems to explain the observed offsets, it is curious that some close-by core stations are more heavily affected than other mainland antennas further away, as would be expected from Dodson et al. (2017). Future observations should be conducted to investigate this issue in more detail. For the present analysis, data related to the marked offset antennas were flagged out before making the final image cubes and getting the astrometric solutions used for the parallax fitting (see Fig. 4.3e–h).

WX Psc session Epoch I. A systematic shift of ~6 mas can be seen for LA, which is much larger than expected from ionospheric errors. Instead, it might be an artifact from the imaging of a weak source with only three antennas. Although data was flagged related to LA for safety and because flagging provided slightly better parallax fits, it only changed the parallax values by 4% which is well below the relative fitting errors of $\gtrsim$30% (see Fig. 4.3a).

WX Psc session Epoch II. The maser is too weak to be useful for error analysis as its measured

positions show scatter over the whole mapped region of 100×100 mas. As a result, only a few measured positions are found around the mean, with the rest not displayed due to the large scatter (see Fig. 4.3b).

WX Psc session Epoch III. Subarray imaging works, but no specific pattern can be seen in the measured maser positions for any antenna. Data points related to antennas MK and SC are randomly scattered over the whole map area and are not displayed beyond the central region (see Fig. 4.3c).

WX Psc session Epoch IV. Measured positions cluster into two complex groups offset by ∼6 mas, similar in size to that seen in Epoch I. Also, no antenna could be linked to the pattern. Again, it is suspected that this might be an artifact due to the low image quality of the three-antenna subarrays. The complex geometric structure of the group towards the NW certainly hints at the idea that it might be linked to the different beam patterns of various subarray images. As a result, the measured shifts are not necessarily related to systematic errors and no flagging was performed based on these results (see Fig. 4.3d).

To summarize, data flagging for astrometric analysis was done based on the subarray imaging results for all epochs in the OH138 session. All epochs of WX Psc showed no emission on baselines to MK and SC in their cross-power spectra and measurements of their subarray images showed large scatter, except in Epoch I. As a result, data related to MK and SC were flagged out in Epochs II–IV, and the subarray imaging results were used for flagging Epoch I.

As a way to evaluate the total astrometric uncertainty of the final measurements, a new technique is implemented based on the presented subarray imaging (see Table 4.3). Calling these new estimates *triangle baseline errors*, they are calculate by fitting a 2D unweighted Gaussian model to the distribution of peak positions obtained by the ensemble of subarrays, after flagging the specified antennas (shown as solid grey ellipses in Fig. 4.3). There is a potential risk in estimating errors based on a flagging scheme designed to minimize position scatter, as taking out more antennas could result in unreasonably small error values. Keeping this in mind, flagging was kept to the minimum possible, only taking out significantly outlying antennas where the scatter could be explained by a viable error source.

The resulting values are believed contain all residual error sources and are thus probably less likely to underestimate astrometric uncertainties. However, as noted earlier this method requires the maser spot to be strong enough to image it reliably with only three antennas. It is noted that using more antennas would decrease the thermal noise and increase the success rate of forming images. However, this would result in less points to analyze and increase the risk of images getting defocused more rather than shifted coherently; although defocusing also affects the three-antenna method due to time averaging over the 4 h long sessions. This could only be avoided by using short snapshots where the time variable error sources could be considered constant, but the analysis of the resulting images would be hampered by higher side-lobe levels. In any case, using more antennas would make the interpretation of the resulting distribution and identification of possible systematic errors less clear.

Thermal noise errors are evaluated as the random thermal noise in the maps. Fitting errors are associated with the ability to fit Gaussian models to these maser maps and include the effects of maser source structure. As expected, we can see that errors scale as $Thermal < Fitting < Triangle$. In the analyses (see Table 4.3) this trend is evident in all but WX Psc session Epoch II,

Table 4.3. Error estimates of astrometric results

Method	Error in R.A.				Error in Dec.				Total Error			
	I	II	III	IV	I	II	III	IV	I	II	III	IV
	mas	mas	mas	mas	mas	mas	mas	mas	mas	mas	mas	mas
					WX Psc Spot ❍							
Thermal	0.24	0.57	0.58	0.42	0.46	1.09	1.10	0.80	0.52	1.23	1.24	0.90
Fitting	0.71	1.00	0.75	0.67	1.04	1.50	1.39	1.04	1.26	1.80	1.58	1.24
Triangle	0.78	0.48†	1.31	3.02†	1.48	0.34†	1.96	2.20†	1.67	0.59†	2.36	3.74†
					OH138.0+7.2 Spot ❍							
Thermal	0.04	0.07	0.03	0.04	0.09	0.17	0.08	0.09	0.10	0.18	0.09	0.10
Fitting	0.09	0.11	0.05	0.06	0.19	0.19	0.11	0.12	0.21	0.22	0.12	0.13
Triangle	0.31	0.15	0.13	0.16	0.76	0.29	0.38	0.42	0.82	0.33	0.40	0.45

Notes. I–IV refer to the observing epochs. Thermal: errors from thermal noise are based on the equation in Sect 4.1.3. Fitting: calculated by least-squares fitting of Gaussian models to the images using the AIPS task IMFIT/JMFIT. The parameters of the image cubes used for the calculations are described in Sect. 4.1.4. Triangle: errors derived from subarray imaging by fitting Gaussian models to the measured peak positions of all subarrays (see grey solid ellipses in Fig. 4.3). All errors are summed in quadrature.
† Unreliable triangle baseline errors due to failed subarray imaging (see Sect. **??**).

where the subarray imaging failed. The triangle baseline errors of WX Psc session Epoch IV also seem problematic and most likely overestimate the real astrometric uncertainties due to the complex structure seen in Fig. 4.3d. However, in most cases the values confirm that the triangle baseline errors are the most conservative estimates. They should not be skewed by a high SNR in the image, but contain all possible error sources instead. In conclusion, final astrometric error estimates are based on these values directly in all but the two problematic epochs. In the case of WX Psc, triangle baseline errors are 1.1–1.8× larger than fitting errors where the method works. As a result, for astrometric analysis the final errors are taken as the double of the fitting errors for Epochs II and IV of WX Psc, although as no real flagging was possible for these epochs (besides MK and SC), the increase in the subarray scatter might be even larger than the values measured using other flagged epochs.

4.1.4 Astrometric Results and Discussion

Maser Maps and Parallaxes

Final maser image cubes for proper motion and parallax fitting were produced with the AIPS CLEAN procedure after flagging data listed in Table 4.2, based on the method described in Sect. **??**. Uniform weighting was used for mapping, as that gave the best astrometric results after considering the trade-off between angular resolution and SNR. Maser emission was detected over several channels in all epochs of both stars and both peaks, however the redshifted features were always too defocused for astrometry. Typical synthesized beam sizes achieved in the final image cubes were approximately 18 × 8 mas for WX Psc, and 13 × 5 mas for OH138 due to less flagging. Figure 4.4 shows a typical example from the produced image cubes, which plots the brightest maser channel in both the blue- and redshifted peaks of OH138.

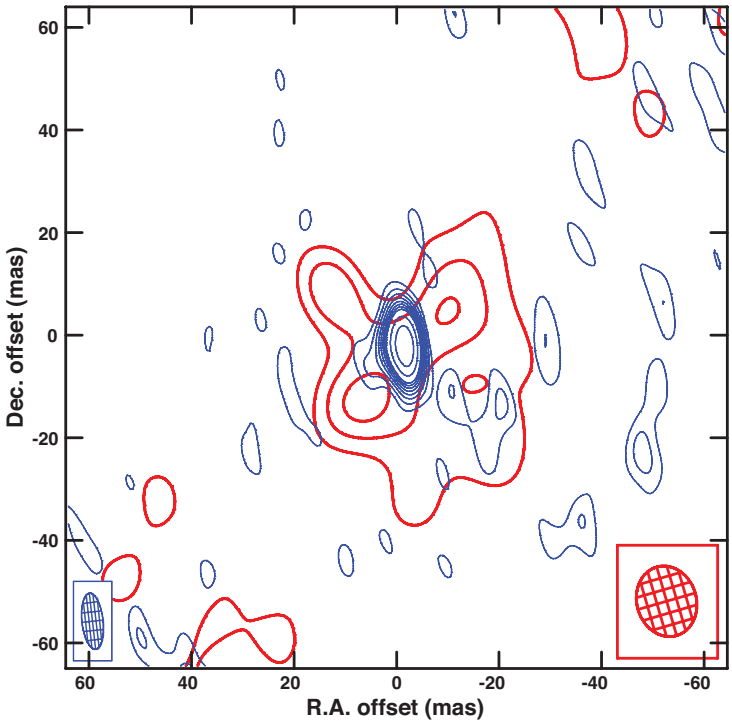

Figure 4.4. Contour map of 1612 MHz OH maser spots towards OH138 in Epoch III. Blue thin contours show the compact blushifted maser spot used for astrometry at −47.0 km s^{-1}, while red thick contours show the brightest redshifted maser channel at −28.5 km s^{-1}. To emphasize faint structures, contour levels run linearly from 3×RMS for 8 steps, then exponentially with a base of $\sqrt{2}$. RMS values refer to the average noise in line-free channels of the image cube. Synthesized beams used for restoring the maps are shown in the bottom corners, with sizes of 13×5 mas (blue) and 16×13 mas (red). The map covers an area of 128×128 mas, centered on the shifted phase tracking center.

Only a single feature is detected in the blueshifted peaks of WX Psc and OH138, but they are reasonably compact and stable in both cases to be used for astrometric analysis. 2D Gaussian models are fitted to the CLEAN maps of the blueshifted maser emission to determine the astrometric position in each epoch. Faint and extended emission from the brightest redshifted maser spots can only be detected on baselines of $\lesssim$2000 km, as they are completely resolved with smaller synthesized beams. Red- and blueshifted spots clearly overlay for OH138, indicating that we are truly seeing the front and backside of the expanding 1612 MHz OH shell. In the case of WX Psc the position of the redshifted maser was ambiguous, but no trace of emission spatially coinciding with the blueshifted feature was detected.

Maser motion is characterized by a combination of a linear proper motion component and a sinusoidal component from the annual parallax. Figure 4.5 shows the fitted proper motions and parallaxes of WX Psc and OH138, while Table 4.4 lists the measured and calculated values. In the case of WX Psc, only a single detected maser spot could be used to derive the maser motions, and although the proper motion could be determined, only an upper limit could be calculated for the annual parallax (see below). For OH138, the motion of two spots of the same maser feature were followed and fitted, and the final proper motion and parallax values were derived using "group fitting" – i.e. fitting both maser spots together by assuming a common distance. The derived values were checked by also fitting the parallax from the two spots individually, with all giving consistent results.

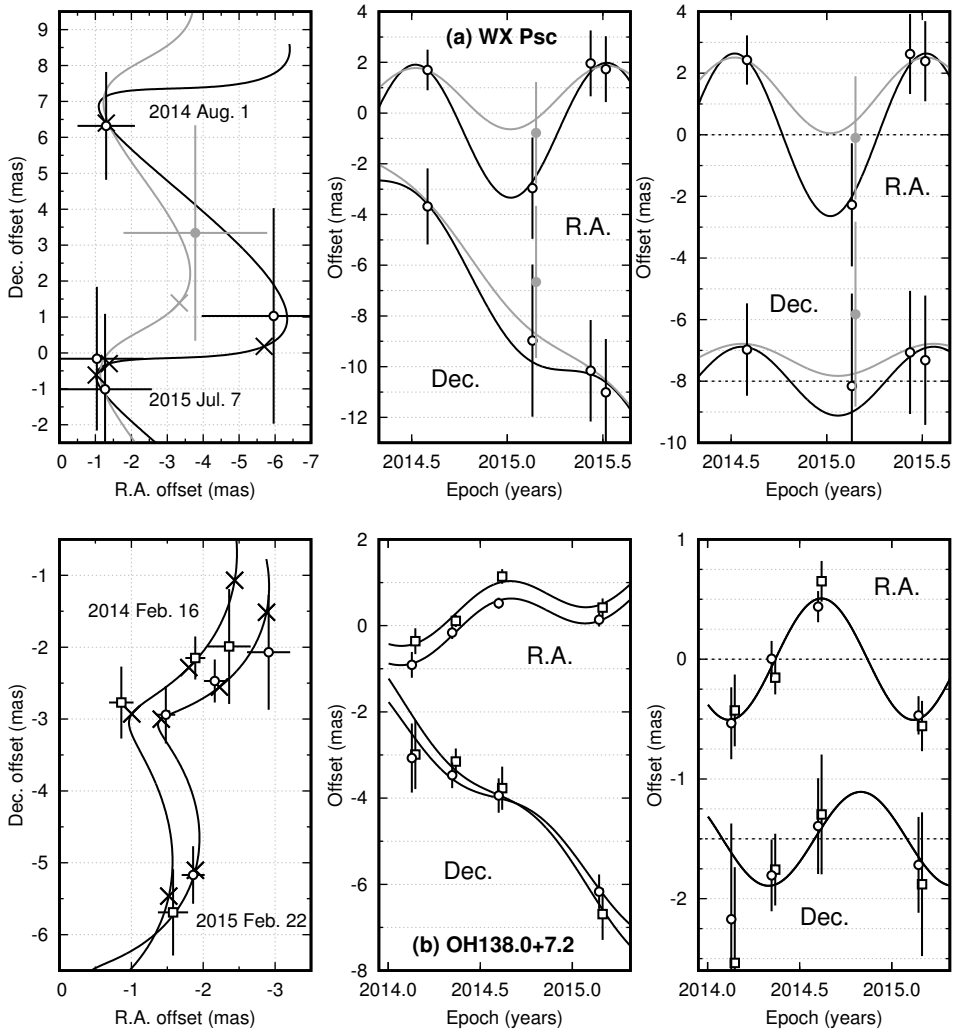

Figure 4.5. Parallax and proper motion fitting for 1612 MHz OH maser spots associated with (a) WX Psc and (b) OH138. Left: Maser spot positions on the sky with respect to the shifted phase tracking centers; first and last epochs are labeled. The positions expected from the fitted models are indicated with crosses. Middle: Maser spot offsets in RA and Dec as a function of time, with the best parallax and proper motion fits. Right: Parallactic motions of maser spots in RA and Dec shown after removing the linear proper motions. In case of WX Psc, two possible models are shown due to the ambiguity in the maser spot position in Epoch II. For clarity, in the middle and right panels constant shifts are added to the offsets, with spots also shifted in time by a small amount (7 days) in case they are in the same epoch.

The proper motion values contain both the systemic proper motions related to the stellar movement and the internal motions of the OH masers relative to their host stars. It is not possible from the few detected maser spots to unambiguously separate these two components, however this does not change the value of the parallax as long as the masers are not accelerating. Also, as we are tracing the front side of an expanding shell in the line-of-sight of the star (see Fig. 4.4), internal motions should not dominate the derived proper motions (c.f. van Langevelde et al., 2000).

In the case of WX Psc, there is a large ambiguity in the derived parallax value from the difficulty of tracing the same maser component between epochs. In Epoch II the brightest part of the feature separates into two spots in adjacent velocity channels (-9.3 and -9.7 km s^{-1}), both

Table 4.4. Astrometric results of 1612 MHz OH masers around WX Psc and OH138.

Target	Spot ID	Epoch	V_{LSR} (km s^{-1})	$\Delta\alpha \cos\delta$ (mas)	$\Delta\delta$ (mas)	$S_{1.6GHz}$ (mJy beam^{-1})	RMS	SNR
WX Psc	❍	I	−9.5	−1.3 ± 0.8	6.3 ± 1.5	190	11.0	17
		IIa	−9.3	−6.0 ± 2.0	1.0 ± 3.0	54	7.4	7
		IIb	−9.7	−3.8 ± 2.0	3.3 ± 3.0	50	7.4	7
		III	−9.4	−1.0 ± 1.3	−0.2 ± 2.0	104	14.4	7
		IV	−9.5	−1.3 ± 1.3	−1.0 ± 2.1	128	13.0	10
	(a)	$\mu_\alpha \cos\delta$ = 0.1±0.4 mas yr^{-1}			μ_δ = −7.5±0.7 mas yr^{-1}		π = 2.9±0.8 mas	
	(b)	$\mu_\alpha \cos\delta$ = 0.1±0.6 mas yr^{-1}			μ_δ = −7.5±1.0 mas yr^{-1}		π = 1.3±1.2 mas	
OH138	❍	I	−47.0	−2.9 ± 0.3	−2.1 ± 0.8	472	7.9	60
		II	−47.2	−2.2 ± 0.15	−2.5 ± 0.3	343	11.6	30
		III	−47.0	−1.5 ± 0.13	−2.9 ± 0.4	570	8.8	65
		IV	−46.9	−1.9 ± 0.16	−5.2 ± 0.4	516	8.2	63
		$\mu_\alpha \cos\delta$ = 0.92±0.14 mas yr^{-1}			μ_δ = −3.48±0.31 mas yr^{-1}		π = 0.47±0.06 mas	
	❒	I	−46.7	−2.4 ± 0.3	−2.0 ± 0.8	190	7.9	24
		II	−46.9	−1.9 ± 0.14	−2.2 ± 0.3	408	11.6	35
		III	−46.6	−0.9 ± 0.17	−2.8 ± 0.5	156	8.8	18
		IV	−46.6	−1.6 ± 0.2	−5.7 ± 0.6	130	8.2	16
		$\mu_\alpha \cos\delta$ = 0.93±0.27 mas yr^{-1}			μ_δ = −4.33±0.73 mas yr^{-1}		π = 0.61±0.12 mas	
Group fitting		$\mu_\alpha \cos\delta$ = 0.93±0.21 mas yr^{-1}			μ_δ = −3.89±0.53 mas yr^{-1}		π = 0.52±0.09 mas	

Notes. Spot ID symbols are identical to ones used on Fig. 4.5, with the exception of WX Psc spot IIb plotted in gray. In the case of WX Psc, (a) shows the model fit in black and uses spot IIa, while (b) shows the model fit in gray and uses spot IIb for Epoch II with the rest of the epochs being identical between the two variations (see Fig. 4.5). Positions are relative to the following J2000.0 phase centers: $(\alpha, \delta)_{\text{WX Psc}}$=($01^h06^m26^s.02574$,+12°35′52″.8242) and $(\alpha, \delta)_{\text{OH138}}$=($03^h25^m08^s.42975$,+65°32′07″.0900). Position errors are the same as error bars shown on figures and are derived from subarray imaging (see "triangle baseline errors" in Sect. **??**). OH138 Spot ❒ errors were rescaled from Spot ❍ errors by the difference in SNR. RMS values refer to the average noise in line-free channels of the image cubes.

evenly shifted to the brightest spot's velocity of −9.5 km s^{-1} in other epochs. Parallax models were fitted using both spots individually and while the proper motion values agree, there is a discrepancy in the amplitude of the parallaxes (see the black and gray models in Fig. 4.5 for the fits using the spot at −9.3 and −9.7 km s^{-1} respectively). The parallax values also have a large uncertainty due to the timing of the observations, as the fitting errors are dominated by the measurement errors in Epoch II. Therefore, uncertainties that are double the formal fitting errors are quoted conservatively (c.f. Reid et al., 2009), since effectively the parallax and proper motion solutions have only one degree of freedom. Averaging the two channels provides a parallax value between the two extremes with all options resulting in χ^2<1 solutions. At this time, it is impossible to better constrain the parallax value of WX Psc and only a 3σ upper limit of $\pi \lesssim 5.3$ mas is quoted as the final result.

The fitted parallax values for OH138 using unflagged data and data that were flagged as described in Sect. **??** were also compared. All measurements were derived from the same data reduction and were assigned identical astrometric uncertainties for comparison. When data are flagged, results are what is shown on Fig. 4.5 and listed in Table 4.4: π=0.52±0.09 mas with

χ^2=4.2. As the result is derived using group fitting, the quoted uncertainty is the formal fitting error multiplied by $\sqrt{2}$ to allow for the possibility of correlated positions for the two maser spots (c.f. Reid et al., 2009). For the unflagged data the fitted values are: π=0.36±0.14 mas with χ^2=10. One can see a reduction in both the χ^2 values and the σ fitting errors in the flagged data in comparison to the unflagged data, though the two parallaxes are consistent within their uncertainties. The error in the parallax obtained with the flagged data is lower and that reflects the additional effort made in mitigating systematic errors, thus π=0.52±0.09 mas is concluded as the parallax estimate for OH138.

On a side note, I would like to mention the limitations of a common practice in parallax papers. Astrometric errors are often calculated by adjusting the error values in each coordinate independently to attain a $\chi^2_{\rm red}=\chi^2/K\sim1$ value in the proper motion and parallax fitting, where K is the number of degrees of freedom in the model (e.g. Reid et al., 2009; Imai et al., 2012). This might be a valid method for estimating errors when fitting highly overdetermined models with many epochs and maser spots, but it has two problems: K is not always simply "data points" minus "model parameters" and the χ^2 value also has an uncertainty due to measurement errors (Andrae et al., 2010). In our case, K is essentially 1 and 3 for the fitting of WX Psc and OH138 respectively, thus e.g. we can derive a $\chi^2_{\rm red}\approx1.4$ for the OH138 parallax. Although $\chi^2_{\rm red}$ values around unity are reassuring in evaluating the quality of the fit, the mentioned problems in calculating $\chi^2_{\rm red}$ are most severe when K is small and renders $\chi^2_{\rm red}$ based error estimation and parallax fitting unreliable in the present case.

Comparison with Published OH Astrometry

Prior to the results presented here, only 5 AGB stars had measured parallaxes based on astrometry of OH masers (van Langevelde et al., 2000; Vlemmings et al., 2003; Vlemmings & van Langevelde, 2007). These measurements used 1665 MHz and 1667 MHz main-line transitions and a variation of conventional source-switching and in-beam techniques, depending on the available calibrators for each source. In the case of conventional phase referencing (U Her, R Cas and W Hya), the total astrometric uncertainties were between 0.7–3 mas per epoch, depending on the target–calibrator separations and ionospheric conditions. Proper motion errors for RA and Dec were in the range of 0.3–3 mas yr^{-1} and 0.3–5 mas yr^{-1}, respectively. The precision of the parallax estimates were 0.3–4 mas, where fitting errors depend on the number of observed epochs and maser spots used, although more spots do not necessarily imply a higher precision or accuracy. The astrometric uncertainties generally decreased when in-beam calibration was possible (S CrB and RR Aql, with calibrator separations of 20′−24′), to 0.2–1.5 mas per epoch. Fitting errors also decreased to 0.2–0.7 mas yr^{-1}, 0.3–0.7 mas yr^{-1} and 0.17–0.5 mas for the proper motions in RA, Dec, and the parallax, due to the smaller source separations and simultaneous observations of target–calibrator pairs.

From this, we can conclude that the astrometric precision per epoch of the presented OH maser measurements is essentially the same as prior in-beam results indicating no reduction in error contributions of dynamic nature. On the other hand, the uncertainties in our parallax and proper motion fits of OH138 agree with previous in-beam investigations in spite of using fewer epochs (4 epochs per star compared to 5–17 epochs in previous works). The errors in the proper motion of WX Psc also agree with this trend, while the parallax results were shown to be too ambiguous for a useful comparison. This might indicate that the flagging scheme explained in Sect. 4.1.3

works well in reducing static errors and can be of good use to multi-epoch maser VLBI investigations at low frequencies. However, these error metrics have to be treated with care as there are very few data points (see Andrae et al., 2010). Smaller errors can also be attributed to better sampling of the parallactic motion (i.e. measuring at the RA extrema as opposed to a uniform sampling, Reid et al., 2009), although the presented measurement spacings were also not optimal.

Comparison with the Phase-Lag Technique

In the following section, derived trigonometric distances are compared to distances derived with the "phase-lag" technique (van Langevelde et al., 1990, hereafter called as "phase-lag distances"), to try to evaluate their accuracy as distance measurement tools to evolved stars. As discussed at the beginning of Sect. 4.1, the 1612 MHz OH masers around OH/IR stars originate in saturated circumstellar shells, expanding outward at terminal velocity. As a result 1612 MHz OH masers are radially amplified and their intensity follow the underlying stellar pulsations.

Phase-lag distance measurements rely on monitoring these variations in the red- and blueshifted maser peaks to determine the τ_0 time shift between the emission coming from the front and backside of the 1612 MHz OH maser shell (van Langevelde et al., 1990). The D linear diameter of the shell can be obtained using $D{=}c\tau_0$, where c is the speed of light in vacuum. By also measuring the ϕ angular size of the OH shell through interferometric observations (Etoka et al., 2014), we can get the d_{pl} phase-lag distance to the star as $d_{pl}{=}D\phi^{-1}{=}c\tau_0\phi^{-1}$.

Table 4.5 lists the two different distance estimates for our observed OH/IR stars, where the phase-lag values[7] are taken from Engels et al. (2015). Trigonometric distances are the reciprocals of the measured parallax values described in Sect. 4.1.4. In case of low significance results, prior assumptions can heavily influence the converted distance (Bailer-Jones, 2015), such as the spatial distribution of the Galactic AGB population. However, as known distributions are poorly constrained and depend largely on the initial mass, their effect on the trigonometric distances are not considered at this time. In the case of WX Psc, only a lower limit of $\gtrsim$190 pc is quoted on the distance at a 3σ significance level. For OH138, the measured distance is $\sim$1.9 kpc at a $>5\sigma$ significance.

Phase-lag distances agree with the trigonometric distances within the errors, but only OH138 can yield a proper comparison at this time. The phase-lag distance of OH138 gives a larger value by $\sim$15%, which might be explained by the limited sensitivity of the interferometric observations in determining the angular size of the OH shell close to the systemic velocity where the 1612 MHz OH maser emission is the weakest. This can lead to an overestimation of the distance, although poor map quality also makes measurements more uncertain so we cannot consider this a systematic bias. Furthermore, the measured angular size also depends on the assumed OH maser shell model: deviations such as spherical asymmetry, non-isotropic radiation, or a thicker OH shell cause systematic errors and skew the measured distances, unless corrected by proper geometrical modeling (Etoka & Diamond, 2010).

[7]Based on an on-going single-dish monitoring program with NRT, and imaging campaigns with the VLA and eMERLIN. For updates in the phase-lag distance project, refer to www.hs.uni-hamburg.de/nrt-monitoring.

Table 4.5. Comparison of distance estimates.

Method	WX Psc distance (kpc)	OH138.0+7.2 distance (kpc)
Trigonometric	$\gtrsim$0.2	$1.9\ ^{+0.4}_{-0.3}$
Phase–lag	0.5 ± 0.1	2.2 ± 0.5

Notes. Trigonometric errors are based on the parallax fitting, with only a 3σ lower limit quoted for WX Psc. Phase-lags assume ±20% relative errors based on Engels et al. (2015).

4.1.5 Summary and Outlook

Over the last decade the field of OH maser astrometry has been in abeyance. In this chapter, VLBA multi-epoch measurements were used to derive astrometric solutions of 1612 MHz OH masers around WX Psc and OH 138.0+7.2, the first results since Vlemmings & van Langevelde (2007). It was shown that the largest limitation in attaining these low-frequency astrometric solutions is from direction-dependent static ionospheric errors that can cause large systematic shifts in the measured maser positions, and are very sensitive to the target–calibrator separation. This can cause serious problems even with in-beam phase referencing calibration techniques, and limit the accuracy of OH maser parallax measurements at 1.6 GHz. An attempt to partially address this problem was the introduction of a new method to identify data affected by systematic errors. It is based on making many different three-antenna subarray images of the same compact emission and analyzing the spatial distribution of the peak positions between the various images. It was also shown that it is possible to get a good estimate of astrometric uncertainties using this technique, although variations in antenna number should be explored to increase the robustness of the results. It would also be prudent to further investigate the correlation between the static ionospheric errors of different antennas in VLBI arrays.

Based on the corrected OH maser astrometry, the resulting annual parallax of OH138 is π=0.52±0.09 mas, making it the first sub-mas OH maser parallax measured. This corresponds to a distance of d_π=$1.9^{+0.4}_{-0.3}$ kpc, which places the source in the thick disk region ∼240 pc above the Galactic plane. For the parallax of WX Psc only a 3σ upper limit of $\pi\lesssim$5.3 mas could be determined, placing it at a distance of $d_\pi\gtrsim$190 pc. The present results are also the first trigonometric distance measurements to enshrouded OH/IR stars, with long period variability (650 and 1410 days) and high mass loss rates of $\sim10^{-5}$ $M_\odot$ yr^{-1}. Finally, the trigonometric distances were used to evaluate the phase-lag distance estimates of these sources and found the two independent methods to be in good agreement with each other. Due to the large uncertainty in the derived distances, it is necessary to continue the parallax observations for a more comprehensive analysis. This would also make it possible to explore additional error estimates, e.g. cross-validation or bootstrapping (Andrae et al., 2010), to better confine the errors of our astrometry and evaluate the newly introduced triangle baseline errors.

Working out the technical issues of low-frequency OH maser astrometry will make it possible to accurately and precisely measure the trigonometric distances to a large number of OH/IR stars and study potential questions in late stellar evolution. One main scientific topic is the study of the period–luminosity relationship of Galactic long period variable AGB stars and the evolutionary connection between Miras and OH/IR stars. Accurate distances can also help us better understand, e.g. how metallicity or mass loss influence stellar pulsation and evolution,

and they can also help us put constraints on AGB evolutionary models. Additionally, stellar OH masers can open up possibilities as new relaxed tracers of Galactic dynamics, and by measuring their distance we could study the motion of material in the inter-arm regions and thick disk. A short introduction of these topics using the results derived here is presented in the next chapter.

As a technical outlook for high-precision low-frequency astrometry, the development and testing of advanced calibration techniques are also underway, i.e. the *MultiView* technique mentioned presented Sect. 3.2 as an alternative approach to in-beam phase-referencing calibration. MultiView is based on the 2D modeling of the phase screen around the target by using scans on multiple calibrators. This makes it possible to fully compensate for the spatial static component of the ionosphere, even with calibrators several degrees away. The demonstration of its performance can be seen in Sect. 3.2 or Rioja et al. (2017), achieving complete atmospheric mitigation and effectively reaching the thermal noise limit in our measurements. Further development and testing is necessary to support the mentioned science goals using stellar OH masers.

Finally, it is important to note that the Square Kilometer Array (SKA) is planned to be an important part of future VLBI networks (Paragi et al., 2015; Green et al., 2015; Imai et al., 2016). As this will concentrate on the ionospheric dominated low frequencies, it is important to understand and solve the limiting factors of OH astrometry and parallax measurements, which will allow us to take full advantage of the astrometric capabilities of the SKA.

4.2 Science cases of stellar OH maser astrometry

In this section, we are going to look at some possible scenarios where the annual parallax measurements of OH/IR stars can be important. The presented results and ideas are not yet fully developed, mostly due to the small number of trigonometric distances to AGBs, and as such this is only meant as an introduction. We are mainly going to focus on the PLR of Mira variables and LPV OH/IR stars, with shortly mentioning the impact of accurate stellar maser astrometry on the study of stellar evolution and Galactic dynamics.

4.2.1 Period–luminosity relation and stellar evolution

One of the last stages in the evolution of stars in the approximate mass range of 0.8–8 $M_\odot$ is the TP-AGB phase, where stars experience heavy mass loss in the form of stellar winds and pulsations in their envelopes. Although the stellar winds of AGB stars play a crucial role in understanding the chemical enrichment of galaxies, some aspects of their evolution still remain unclear (Marigo et al., 2013). As stars ascend the AGB they go through various stages of instability, from low amplitude overtone pulsators to Mira and OH/IR variables having large amplitude pulsations in the fundamental mode. Pulsations also exhibit a large range of periods from anywhere between about 100 days to over 2000 days. Studies of the stellar population of the LMC have demonstrated that these AGB pulsators fall on a number of PLRs, which are believed to be linked to their different pulsation modes (e.g., Wood, 2000; Ita et al., 2004). Studying these PLRs serve a double purpose: they can be used as good distance indicators and also provide invaluable insight into the mass-loss process and evolution of AGBs (e.g., Whitelock, 2012).

Mira variables, fundamental mode AGB pulsators, have been intensively studied at periods of 100–500 days in the LMC, and their PLR is well constrained in this range (Whitelock et al., 2008). However, Ita & Matsunaga (2011) found that the clear linear relation between m_k and $\log P$, the K band apparent magnitude and the logarithm of the pulsation period, starts breaking down above ∼400 days, but the study of this long period regime has been limited due to the smaller sample size and limited use in Mira PLR distance scale studies. The precisely known distance to the LMC (see Feast, 2013, , and references therein) also gives us accurate luminosity measurements and the ability to derive various stellar parameters in an effort to understand their relation to each other. For example, at periods above ∼400 days higher luminosity AGB stars undergoing HBB might be the cause of some of the observed deviations in the PLR, as a result of the core-mass luminosity connection (Whitelock, 2012). In contrast with the LMC where it is enough to study the m_k – $\log P$ relation due to the small relative differences between the members of the LMC stellar population, the study of the AGB PLR in the MWG requires us to convert the m_k apparent magnitudes to M_k absolute magnitudes due to the large range of possible distances. However, constructing a Galactic M_k – $\log P$ relation has been difficult due to the large uncertainties in the measured distances.

Astrometric VLBI observations of circumstellar masers can determine the proper motions and annual parallaxes to these mass-losing evolved stars. Nakagawa et al. (2014, 2016) has measured several AGB stellar distances using H_2O masers, and collected all available VLBI parallax distances of other AGB stars – including parallaxes from SiO, H_2O , and OH masers (see Table 7 of Nakagawa et al., 2016, and references therein) – to determine the Galactic PLR of Mira variables at P$\lesssim$500 days. However, none of these measurements were towards OH/IR stars, which usually have higher luminosities and longer periods Habing (see review by 1996). Figure 4.6 shows a summation of all the available information we have of the Galactic AGB PLR at the moment, including also the most recent distances to OH/IR stars from Orosz et al. (2017b). The slope of the PLR has been determined by several authors, and I am not going to go into the details of how to determine it or its exact value. Nevertheless, we can see from the spread of the positions that there is ∼0.6 mag uncertainty in its zero point, while the slope of the relation is kept fixed to that determined from the LMC sample. Our astrometric sample size is not big enough to conduct a quantitative analysis at the present time, however general trends can be noted.

For this present look at Fig. 4.6, we are only interested in the relation for the fundamental mode pulsators, as Mira variables and OH/IR stars dominantly pulsate in this most simple mode. Pulsation modes are sensitive to a multitude of stellar parameters, such as their chemical composition, metallicity, mass, mass loss rate, temperature and luminosity. As a result, as AGB stars loose a copious amount of mass – more and more as they progress in their evolution – while also constantly changing the chemical composition of their atmospheres due to their complicated nucleosynthesis in several active layers, the resulting pulsations and their evolution can be very complicated to model, with several modes overlaid atop each other. According to the simulations of (Marigo et al., 2017), some general trends can be concluded. At lower luminosities and higher effective temperatures the dominant pulsation mode is a shorter period first-overtone one, and most thermally-pulsing AGBs start off here. We can observe this in Fig. 4.6 as well, with most semiregular variables (SRa and SRb, stars at the early stage of the TP-AGB phase) clustering around the first overtone (C′) at periods of only ∼120 days. Later as the star evolves, a transition to a dominant fundamental mode with a longer period can occur, meaning that the observed SR, Mira and OH/IR stars might be the same type of AGB star, only observed at different evolutionary stages. Also, stars with higher luminosities and lower effective temperatures

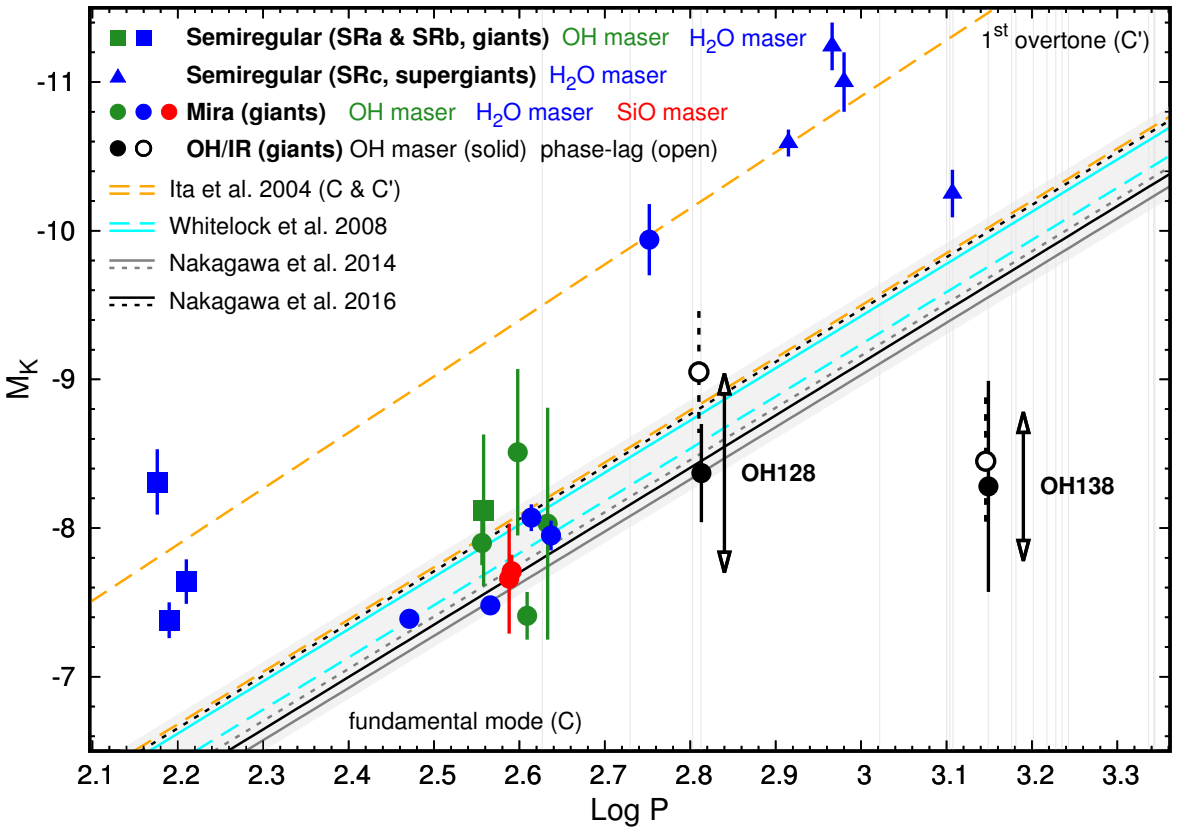

Figure 4.6. Period–Luminosity relation of Galactic AGB stars at K magnitude (2.2μm), with all stars plotted that have a measured VLBI parallax using circumstellar masers (see Table 7 in Nakagawa et al., 2016, for a complete set of distances, periods and references). Red supergiants and semiregular variables have also been plotted for reference, but the PLRs have all been determined using only Mira variables with P$\lesssim$500 days. The multitude of shown PLRs are different solutions, using different subsets of data and methodologies (see cited papers for more details). The black points mark the new datapoints, derived using the OH maser parallax distances presented in Sect. 4.1. Open-headed arrows show the K-mag pulsation amplitudes. Thin grey lines indicate other OH/IR stars with known OH masers and pulsation periods from (Engels et al., 2015).

might skip the dominant first overtone stage and start off as fundamental pulsators; this is an observed characteristic of stars undergoing HBB. Figure 4.6 also shows some RSGs, however we know too little of their behavior and too few data points to derive any conclusion. In any case, Mira and OH/IR stars are believed to be dominant fundamental pulsators, and we are interested in their evolutionary connection and use as distance indicators.

As the OH/IR stars have very thick dust shells, their luminosities have to be corrected for circumstellar extinction in order to plot them on Fig 4.6 in absolute K magnitudes. Having a measured distance to a star (e.g. via annual parallax), the M_K absolute K magnitude can be calculated as

$$M_K = m_K - A_K - 5\,(\log_{10} d - 1)\ , \tag{4.1}$$

where M_K and m_K are the mean absolute and apparent magnitudes of the star at 2.2 μm, d is the distance to the star in parsecs and A_K is the total extinction at 2.2 μm. In the case of WX Psc and OH138, the distance is taken from the OH maser astrometric measurements (see Sect. 4.1)

to be $0.34^{+0.14}_{-0.07}$ kpc and $1.9^{+0.4}_{-0.3}$ kpc respectively[8], while m_K was measured to be 8.12 ± 0.5 mag for WX Psc (Shintani et al., 2008; Chibueze et al., 2016) and 1.65 ± 0.64 mag for OH138 (Yamashita, 2016) using the Kagoshima 1m near-infrared monitoring data[9].

The total extinction A_K is comprised of: circumstellar and interstellar extinction. Circumstellar extinction is by far more dominant for close-by OH/IR stars with heavy dust shells, and it is the biggest source of error in M_K after the uncertainty in the derived distance. In order to calculate the effect of the circumstellar envelope, we have modeled the SEDs of our OH/IR stars using the photometric data found in the VizieR archive[10] (see Table 4.6). The fitted photometric range was 1–160 μm, using only single-epoch data to account for the source variability and accurately model the stellar parameters. Figure 4.7 shows the resulting SED fits, using the modeling method described by Goldman et al. (2017).

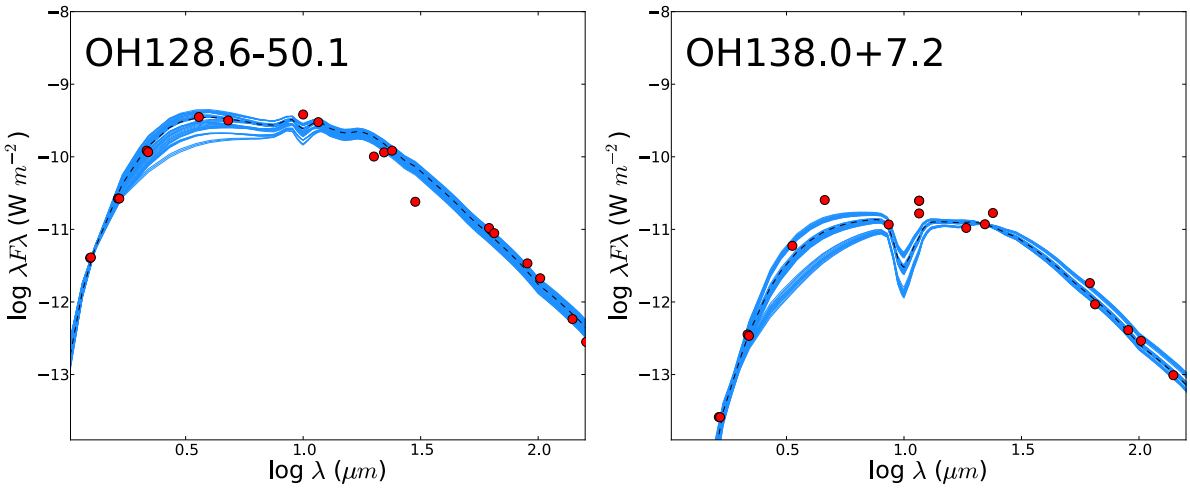

Figure 4.7. Spectral energy distributions of WX Psc, aka OH128.6–50.1 (left), and OH138.0+7.2 (right) based on the method described by Goldman et al. (2017). Blue lines mark the best 50 models, with the dashed line marking the best fit. Red points mark the single-epoch photometric data from Table 4.6, with error bars too small to show.

The fitted SEDs come from radiatively driven wind models using the DUSTY 1-D radiation transfer code (Elitzur & Ivezić, 2001)[11]. The models use a blackbody for the central star and assume a spherical dusty envelope of warm silicate grains from Ossenkopf et al. (1992) with varying effective and inner boundary temperatures, and an "MRN" power-law grain-size distribution (Mathis et al., 1977; Clayton et al., 2003). The best fit to our photometry is found from fitting over 8000 DUSTY trial models using a χ^2-minimizing fitting technique, with each model having 100s of varying normalization factors and various optical depths (see Goldman et al., 2017, for more details on the SED modeling). From the best SED model, DUSTY derives the

[8]The parallax distance to WX Psc was ambiguous due to the velocity structure of the OH maser feature (see Sect. 4.1.4, and another distance could also be derived with a lower significance at d=$0.77^{+10}_{-0.37}$ kpc. Since this is essentially only a lower limit estimate and it is impossible to determine at the moment which of the two distance estimates is closer to reality, the discussion of WX Psc is not at all definite and is only meant as a demonstration of possible science case studies.

[9]The quoted apparent magnitudes are mean values, with the min-to-max amplitude of the fitted stellar K-mag light curve given as "error" intervals. See Chibueze et al. (2016) for more details on the Kagoshima 1m near-infrared monitoring observations.

[10]VizieR Photometry viewer: http://vizier.u-strasbg.fr/vizier/sed/

[11]The DUSTY code: http://www.pa.uky.edu/~moshe/dusty/

Table 4.6. Archival photometry used for the SED fitting of the OH/IR stars.

Wavelength (μm)	Flux density (Jy)	Flux density (Jy)	Filter[†]
	WX Psc	OH138.0+7.2	
0.878	0.46 ± 4		Johnson: I
1.24	1.67 ± 0.04	307 ± 42 (μJy)	2MASS: J
1.25	1.71 ± 0.04	314 ± 43 (μJy)	Johnson: J
1.63	14.5 ± 2.7	14.1 ± 0.1 (mJy)	Johnson: H
1.65	14.6 ± 2.7	14.2 ± 0.2 (mJy)	2MASS: H
2.16	87.6 ± 24.3	257 ± 3 (mJy)	2MASS: Ks
2.19	84.7 ± 23.6	249 ± 3 (mJy)	Johnson: K
3.35		6.62 ± 0.56	WISE: W1
3.6	424 ± 40		Epchtein: [3.6]
4.6		38.9 ± 2.7	WISE: W2
4.8	507 ± 50		Epchtein: [4.8]
8.61		33.5 ± 2	AKARI: S9W
10	1275 ± 130		Epchtein: [10]
11.6	1160 ± 60	95.8 ± 8.6	IRAS: [12]
11.6		64.1 ± 1	WISE: W3
18.4		64.2 ± 3.7	AKARI: L18W
20	672 ± 130		Epchtein: [20]
22.1	847 ± 60	86.7 ± 0.1	WISE: W4
23.9	968 ± 48	134 ± 8	IRAS: [25]
30	240 ± 100		Epchtein: [30]
61.8	215 ± 19	37.5 ± 3.4	IRAS: [60]
65	192 ± 37	20.1 ± 1	AKARI: N60
90	102 ± 4	12.3 ± 0.7	AKARI: WIDE-S
102	72.1 ± 7.9	9.9 ± 0.89	IRAS: [100]
140	27.1 ± 3.2	4.57 ± 2.01	AKARI: WIDE-L
160	15 ± 3		AKARI: N160

Notes. All values are listed in the VizieR online database (Ochsenbein et al., 2000), except for the photometry from Epchtein et al. (1980). References below list the infrared mission or system definition papers. [†] Johnson: Johnson (1966), 2MASS: Skrutskie et al. (2006), WISE: Wright et al. (2010), Epchtein: Epchtein et al. (1980), AKARI: Murakami et al. (2007); Ishihara et al. (2010), IRAS: Neugebauer et al. (1984).

dust shell's optical depth, expected expansion velocity, and the star's mass loss rate. The luminosity is calculated by assuming the previously mentioned OH parallax distances and scaling the model with the resulting normalization factor (see Table 4.7).

Table 4.7. Stellar parameters from fitted SED models using DUSTY.

Target	L (10^3 $L_\odot$)	τ	v_{exp} km s^{-1}	$\dot{M}$ (10^{-6} $M_\odot$ yr^{-1})	r_{gd}	T_{eff} (K)	T_{inner} (K)
WX Psc	3±1	4.1	7±2	4±1	30±15	3500	1200
OH138.0+7.2	3±1	8.9	4±1	11±2	30±15	2900	800

Notes. L stellar luminosity, τ optical depth of the CSE at 10 μm, v_{exp} expansion velocity of the CSE, $\dot{M}$ stellar mass loss rate, r_{gd} gas-to-dust ratio in the CSE, T_{eff} stellar effective temperature, T_{inner} temperature of the inner side of the dust shell. Error bars are derived from the best 50 SED fits (see blue lines on Fig. 4.7.

There are several factors that introduce uncertainties in our derived values, such as the changing dust mineralogy as the star evolves or departures from spherical symmetry in the dust shell. The derived formal errors using the various fits therefore include measurement uncertainties, fitting inaccuracies as well as variations in the parameters that we assumed. Also, our observed expansion velocities from OH masers (tracing the gas in the CSE) are about a factor of 2 larger than the expansion velocities from the DUSTY models. As the models seem to underestimate the true expansion rate, the resulting $M_\odot$ values are only lower limit estimates, which is in agreement with previous findings by Ramstedt et al. (2008) using a comparison between CO (also a gas tracer) and DUSTY models. Comparing our AGB stellar parameters to that of median values in the Galactic Bulge and LMC (see Table 5 of Goldman et al., 2017), we find the following:

- The expansion rate is comparable to both samples, and the OH maser derived velocities also give a factor of 2 larger values than DUSTY results in the case of the LMC and Galactic Bulge. The luminosity is about half of the Galactic centre and only 5% of the LMC values. Temperatures are about the same in all cases.
- The τ optical depths are comparable to that of Galactic centre stars (which range in $\tau \approx 3-20$), but are considerably higher than the average LMC value of $\tau \approx 0.8$, which is probably a result of the lower metallicity of the LMC in general (as the gas-to-dust r_{gd} ratio, which has an influence on opacity, scales inversely with metallicity van Loon, 2000).

The τ optical depth is related to the shape of the SED and can be determined from our DUSTY models as such (see details in Goldman et al., 2017). It is mainly determined by the optical properties of the grain particles in the dust shell, so τ is dependent on how the grain opacity changes as a function of wavelength. The circumstellar extinction can be estimated from the τ optical depth by using the relation of

$$A_K = 2.5 \log_{10} e^{\tau_K} = 1.086\, \tau_K \ , \tag{4.2}$$

where K mag is at 2.2μm. In the DUSTY models, the optical depth of the CSE is calculated at 10 μm, which is almost exactly double the value as the optical depth at 2.2 μm using

our described dust grain model. As a result, the circumstellar extinction values at 2.2 μm for WX Psc / OH138 are estimated to be 2.22 mag / 4.83 mag. The interstellar extinction is corrected for by applying the interstellar extinction curve from Rieke & Lebofsky (1985) to a value of $A_V \sim 1.8$ mag kpc^{-1}, which is a general extinction value for lines of sight close to the plane of the MWG (as in our case) and are applicable for stellar distances up to a few kpc (Whittet, 2003). Thus using a correction factor of $A_K/A_V = 0.112$ and assuming the distances of 0.34 kpc and 1.9 kpc to WX Psc and OH138 respectively, we estimate the interstellar extinction at 2.2μm to be 0.07 mag / 0.38 mag for WX Psc / OH138. The total extinction A_K is the sum of the circumstellar and interstellar extinction: 2.3 mag and 5.2 mag for WX Psc and OH138 respectively, with the circumstellar extinction dominating the values as our sources are close-by OH/IR stars with optically thick heavy dust shells.

Using Equation (4.1) with the derived values for A_K and the earlier quoted m_K apparent magnitudes from Yamashita (2016) and Chibueze et al. (2016), we estimate the M_K absolute magnitudes to be -8.4 ± 0.6 and -8.3 ± 0.4 for WX Psc and OH138 respectively. Doing the same calculation using the phase-lag distances in Table 4.5 results also in similar values, -9.1 ± 0.4 and -8.5 ± 0.4 for WX Psc and OH138 respectively. In all cases, the errors in M_K are calculated by adding the SED fitting uncertainty and the distance uncertainty in quadrature. Figure 4.7 shows the resulting PLR diagram for all the AGB stars with known VLBI distances, with our corrected LPV OH/IR stellar magnitudes plotted as well. We refrain from a detailed analysis, but it is clear that OH138 falls well below the various Galactic PLR predicted by the literature. This indicates that LPVs might deviate from the PLR defined at lower periods, something that is expected based on, e.g., Ita & Matsunaga (2011); Whitelock (2012).

The pulsation period of an AGB star is expected to relate to its mass, metallicity and evolutionary phase. The initial mass plays an important role the dredge-up efficiency, and whether the star undergoes HBB or not; this in turn influences the chemical composition of the star that determines the C/O ratio in the CSE (e.g., Karakas, 2010). It is expected that higher initial mass stars reach higher luminosities in their TP-AGB phase, that will result in higher mass loss rates. As a result, as the star progresses through the TP-AGB phase, its mass decreases while the luminosity remains the same (Goldman et al., 2017). Following this argument, as the star is losing mass, but stays at the same luminosity, the mass loss rate increases and the decrease in mass lengthens the pulsation period. Thus, the source evolves to longer pulsation periods while the luminosity remains constant. Looking at Table 4.7 and Fig. 4.7, our two OH/IR stars support this argument: their L luminosity and M_K absolute magnitudes are the same, even though their pulsation periods differ by a large amount (760 days).

Stellar pulsation amplitudes can also be affected by the changing chemical makeup of the star (Goldman et al., 2017), which can be inferred from the $r_{\rm gd}$ gas-to-dust ratio. Pulsation periods can also hint at the evolutionary stage, with more evolved stars having pulsations with larger amplitudes and longer periods, however the link between pulsation period and evolutionary stage is still unclear (e.g, Sloan et al., 2012). For more on the background of theses issues, refer to Goldman et al. (2017). In any case, measuring trigonometric distances to AGB stars with long periods will shed light on the connection between the various solar parameters, pulsation periods, mass loss rates and the evolutionary stage. Figure 4.7 indicates possible sources for future parallax monitoring campaigns with thin gray lines from citetengels2015b. These sources have double-peaked 1612 MHz OH masers and measured pulsation period, with most of them above 1000 days. Measuring their distance would make it clear if the length of the pulsation period is really independent of luminosity above a certain point. Determining the PLR for very

long periods – if there is one – and its dependence on other physical parameters would also enable the use of OH/IR stars as possible distance indicators.

Another way to utilize our distance measurements is to use the derived stellar luminosities and pulsation periods, and compare the resulting data points to current TP-AGB evolutionary tracks (see Fig. 4.8. The evolutionary tracks were calculated by Paola Marigo and Ambra Nanni from the University of Padova, by using their self-developed COLIBRI code, the can compute the TP-AGB evolution from the first thermal pulse up to the complete ejection of the stellar mantle by stellar winds (Marigo et al., 2013, 2017). It is possible to compute detailed evolutionary tracks for many different model parameters, such as initial star masses, chemical abundances, nuclear reaction rates, dredge-up efficiencies. As an example, Figure 4.8 shows the period–luminosity evolution of two stars with initial masses of 1.0 and 1.2 $M_\odot$ and different metallicities (left and right), assuming they are pulsating in the fundamental mode. The left plot shows the two stellar tracks with a solar metallicity of [Fe/H]~0, and it is clear that while the models can reproduce the derived luminosities of WX Psc and OH138, they cannot reach such long periods at these relatively low luminosities. Increasing the metallicity from solar [Fe/H]~0 to "super-solar" [Fe/H]~0.3 helps in getting longer periods, but the matching is still not that satisfactory (right). Metallicities higher than this are unlikely for our close-by sources.

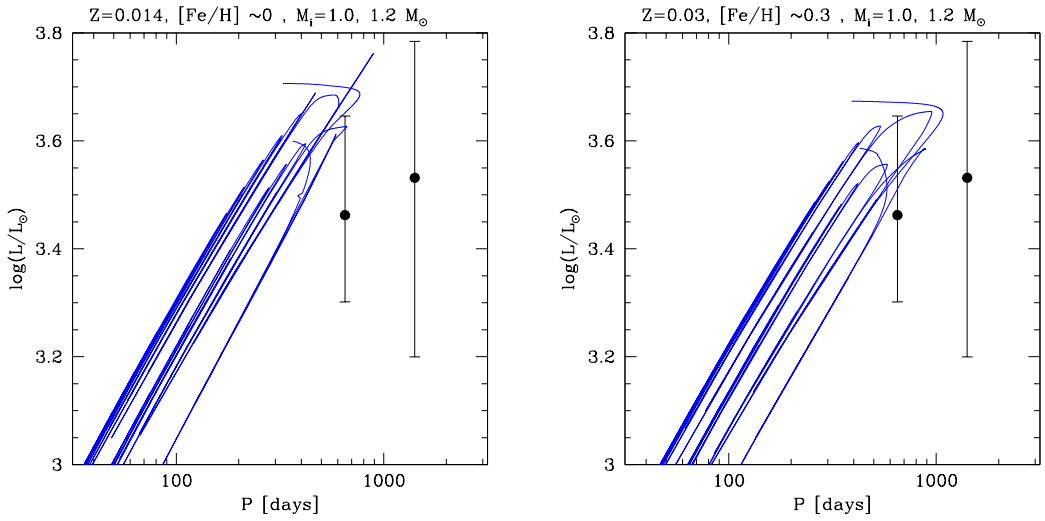

Figure 4.8. TP-AGB evolutionary tracks in the period–luminosity plane for initial masses of 1 $M_\odot$ and 1.2 $M_\odot$ (blue lines), with initial metallicities of solar ([Fe/H]~0, left) and super-solar ([Fe/H]~0.3, right). The black dots mark the derived luminositied for WX Psc (P=650 days) and OH138 (P=1410 days) using the measured OH maser annual parallaxes and DUSTY modeling presented earlier in this chapter.

The fit is poor especially for OH138, but we note that OH138 lies in the thick disk region above a region in the Perseus Arm (z~250 pc), which shows high peculiar motions based on HMSFR proper motion measurements (Reid et al., 2014). This region therefore shows some signs that deviate from Galactic standards and might explain a possibly higher metallicity in OH138 than what would be expected in typical conditions. It is also possible that our derived luminosities are incorrect; the values depend on the measured trigonometric distance and the DUSTY SED modeling. Therefore, any biases in the distance and SED fitting can introduce systematic errors into the luminosity calculation, and the SED fits in Goldman et al. (2017) were shown to underestimate certain parameters (as we also noted previously for our fits, e.g. in the case of the expansion velocities when compared to velocities derived from direct single-dish 1612 OH

maser measurements using the NRT). Thus is is feasible that our stellar luminosities are higher, which means that their long periods then could be explained with high mass progenitors. However, putting speculation aside, based on our present results the luminosities of our OH/IR stars are compatible with low-mass progenitors of 0.8–1.2 $M_{\odot}$, with the caveat that the our derived luminosities are quite uncertain. The measured periods pose a theoretical problem, but with the present data a satisfactory answer cannot be given. It is essential to continue investigating this issue from both observational and theoretical ends, by deriving more accurate parallax distances and extinction parameters, but also investigating the effects of various parameters on the COLIBRI evolutionary track, e.g. different mass loss laws, mixing length parameters, or new pulsation models.

4.2.2 Galactic dynamics

As a final thought for Sect. 4, we take a brief look at another, longer-scale possibility in exploiting our derived OH maser parallaxes to OH/IR stars. Up till now, the study of the structure and kinematics of the MWG was mainly done by parallax measurements to HMSFR tracers, in the large scale surveys of BeSSeL and VERA. This has produced a clear view of the spiral arm structure visible from the Northern Hemisphere (Reid et al., 2014, 2016), but not much else is known about the dynamics of other parts of the MWG as HMSFR are confined to the spiral arms. As mentioned in Sect. 4.1, high-precision VLBI astrometry was focusing on CH_3OH or H_2O masers up till recently as the calibration strategies are effective and well understood at the frequencies of these molecular transitions. ABG stars could not be used as tracers, as they only exhibit SiO, H_2O and OH masers, and all three had various problems in the astrometric applicability (see Sect. 4.1). However, with new observation techniques, such as the demonstrated MultiView technique for OH masers (see Sect. 3.2) or SFPR for SiO masers (Dodson et al., 2013), AGB stars can now be more readily utilized as Galactic tracers by conducting proper motion and parallax measurements.

We will concentrate on OH masers, due to the large available sample (several thousand) in Engels & Bunzel (2015) and Qiao et al. (2016), covering both hemispheres. Stellar OH maser sources are spread over not just the Galactic thin disk, but the inter-arm regions, the Galactic thick disk and bulge, as well. OH maser parallaxes to OH/IR stars can directly help in mapping these regions, but they can also be used indirectly by evaluating distance measurements by the phase-lag method (see Sect. 4.1.4). Working out the issues in the phase-lag method would allow us to measure the distance to a large number of OH/IR stars with future SKA surveys. This was we could build up a more complete picture of MWG dynamics by using the dynamically relaxed AGB stars as new Galactic tracers, and explore how widely the materials ejected from the stars are spread in the MWG.

Figure 4.9 shows all the AGB and RSG stars that have measured annual parallaxes (Nakagawa et al., 2016; Orosz et al., 2017b, and references therein), overlaid on the most recent Galactic map based on parallaxes to HMSFR (Reid et al., 2016). All the known distances are confined to less than <3 kpc, due to the technical challenges in stellar maser astrometry. However, with MultiView, it is now feasible to measure distances to 1612 MHz OH masers with a much higher accuracy, thus extending the region can be probed by VLBI stellar maser astrometry. The next step towards large scale SKA surveys utilizing the phase-lag technique by multi-epoch monitoring of a large number of 1612 MHz OH masers is to measure the annual parallaxes to a

significant number of stars, and compare those values to phase-lag distance measurements to calibrate the later. The first targets can be sources in Engels et al. (2015), which are marked with open circles on Fig. 4.9. As a final side note, measuring the distance and proper motion of AGB stars would also make it possible to directly measure the difference in their rotation speed compared to HMSFRs. Based on large scale studies by Honma et al. (2012) and Reid et al. (2014), HMSFRs seem to lag behind on average to calculated circular orbits. By comparing the 3D velocities of HMSFRs tracing the spiral arms and AGBs tracing the Galactic disk, it would be possible to see if the observed HMSFR lag is caused by physical processes or errors in the 3D solar motion. However, at the moment the available AGB distances do not sample a large enough area to conduct this test, so it is important to continue OH maser parallax and proper motion measurements by adopting and improving upon the techniques described in this thesis.

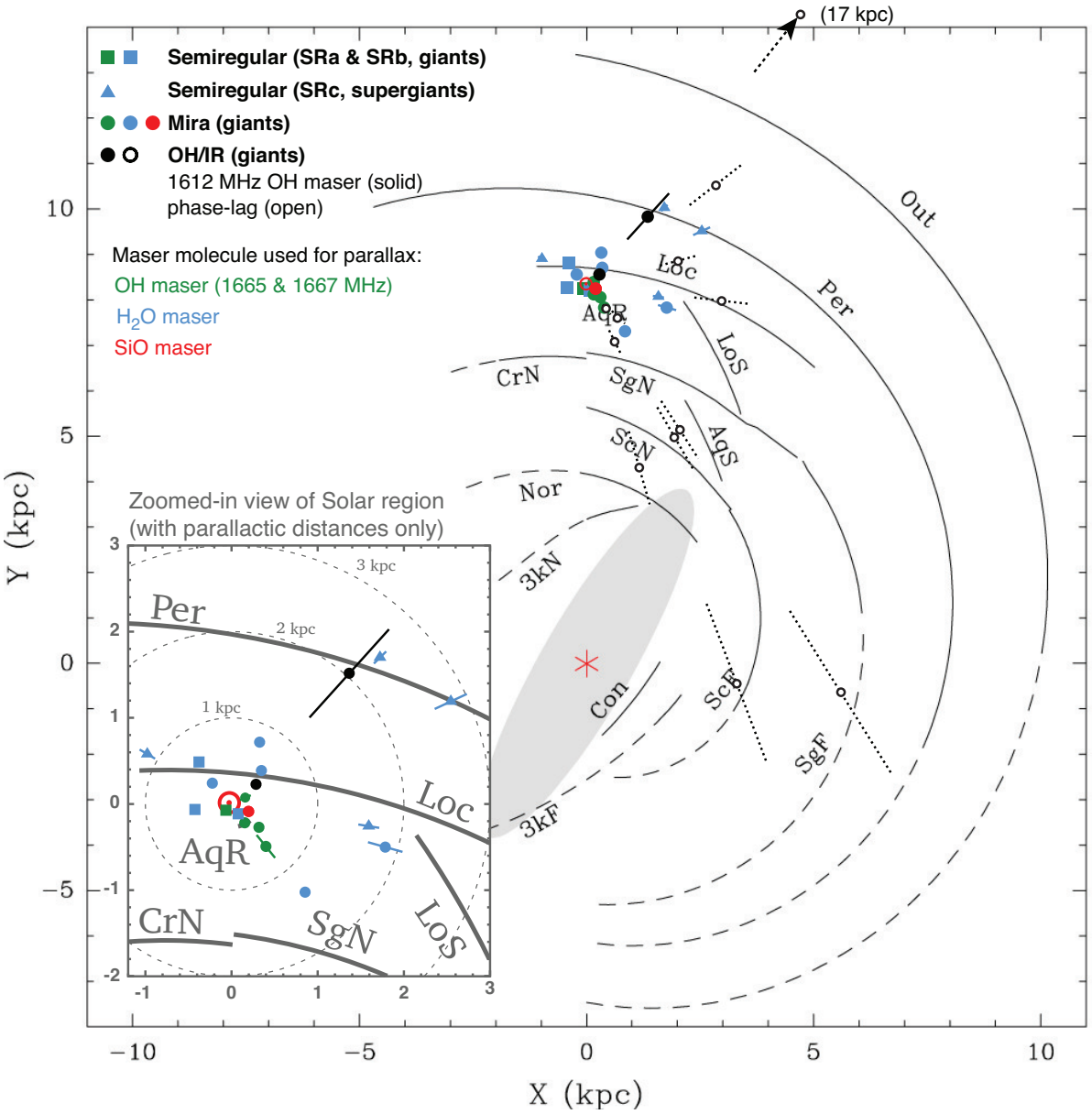

Figure 4.9. All evolved stars with maser parallaxes overlaid on the most recent Galactic map based on parallaxes to HMSFR (Reid et al., 2016). Solid symbols show sources with parallax based distances, while open circles show sources with phase-lag distances. The later are possible targets for future OH maser measurements, to validate the accuracy of these distances.

5 | Astrometry of water fountain water masers

Up to now, we concentrated on thermally-pulsing AGB stars and the masers in their CSEs. The next stage in late stellar evolution is when the nucleosynthesis stops and the star enters the post-AGB phase. In this stage, the star can no longer maintain the 1612 MHz OH masers seen previously, and the main form of maser pumping mechanism becomes collisional excitation. Post-AGB stars are important, as they are the link between AGB stars and PNe, two late stages with strikingly different characteristics yet located closely in the evolutionary sequence. Explaining the formation of PNe, whose morphology depart significantly from spherical symmetry, is one of the big questions in late stellar evolution (see review in Balick & Frank, 2002). It involves a sudden change in mass-loss mode from spherical to bipolar that occurs on a timescale of only a few hundreds of years.

Water fountain stars are key objects in understanding this process, as they are presently undergoing such morphological changes and also host masers in morphologically and kinematically highly collimated fast jets (see e.g. Imai et al. 2002). These masers allow us to make use of VLBI to measure the precise motion of the outflows and thus characterize the physical parameters of the mass-loss. VLBI observations show that the maser emission is shock-excited in bipolar outflows. Due to the short lifespans of water fountains, only about a dozen are known so far.

Despite the believed importance of WFs in explaining the shaping of PNe, we still do not know whether all intermediate-mass stars pass through the WF phase, or only those with some special (and yet unknown) physical characteristics. The evolution of WFs are also open to debate, and there are certain differences in the maser distribution of WF jets that might serve as indicators to assess the detailed evolutionary sequence of evolved stars from leaving their AGB phase to becoming young PNe (Suárez et al., 2009). Another interesting difference between individual WFs is that some also host H_2O masers in slowly expanding central structures, in addition to H2O masers in the high-velocity jets. This might indicate at a remnant of the circumstellar envelope or some toroidal structure, but the scarcity of known sources and the lack of long-term monitoring measurements make it impossible to give a firm explanation. Therefore, it is important to use the unique capabilities of VLBI astrometry and these H_2O masers to map and characterize the spatial and kinematic structure of each source individually, and then try to find common characteristics between them to better understand jet launching and PNe shaping.

5.1 Astrometry of water masers around IRAS 18113–2503

IRAS 18113–2503 was first noted by Preite-Martinez (1988) to be a possible PN, based on IRAS data (cataloged as PM 1–221). Later it was listed as a possible proto-PN, i.e. post-AGB star, by several authors (Hu et al., 1993; Kohoutek, 2001; Szczerba et al., 2007), before Gómez et al. (2011) finally confirmed it as a WF, mapping the objects using VLA measurements of 22 GHz H_2O masers. IRAS 18113–2503 harbors jets, spanning a very large line-of-sight velocity range of ∼500 km s^{-1}, with the very high velocity dispersion of ∼170 km s^{-1} in each jet. Gómez et al. (2011) concluded that based on the single-epoch VLA data, the large dispersion could be interpreted as the jets having a large opening angle, or as internal shocks along the jet, generated by episodic mass-loss events with increasing velocities.

In order to learn more about this WF, we started two H_2O maser monitoring campaigns with the VLBA and VERA to measure the source's proper motion and parallax. The VLBA observations (project ID: BG231, PI: J.-F. Gómez) were spaced every 2 weeks for a total of 5 epochs, to measure the internal motion of the WF jets, but they are still under analysis. The early results from the data reduction clearly show two distinct cap-like bow-shocks in both blue- and red-shifted outflows (Gómez et al. 2017, in prep) in all 5 epochs. The pattern is similar to that seen in many other WFs, such as IRAS 19190+1102 (Day et al., 2010), W43A (Chong et al., 2015), or IRAS 18043–2503 presented in the next chapter only having a different inclination angle. The results suggest the same as IRAS 18043–2503, that WF jets shape their CSE in accordance with the so called "cavity model" (Chong et al., 2015), although this should be further tested due to alternative hypotheses (see Yung et al., 2011, 2017).

In order to measure the annual parallax, we conducted monitoring observations with VERA over one year, with the following epochs: 2014 April 4, June 12, September 5, October 3, November 3, December 3, 2015 February 6, March 6 and April 4. Due to the large velocity spread of the masers, the VERA bandwidth could only cover the brighter blueshifted lobe. Left-handed circular polarization signals were recorded in VERA7 mode, i.e. a dual-beam setup with 1 IF in the A-beam centered on the H_2O maser lines and 15 contiguous IFs in the B-beam covering the continuum reference source J1820-2528 1.53° away. An IF had a bandwidth of 16 MHz, with a spectral resolution of 31.25 kHz (0.42 km s^{-1}) for the maser IF, that resulted in a total recording data rate of 1024 Mbps. The phase tracking center for IRAS 18113–2503 was set to $(\alpha, \delta)_{J2000.0}$=(18:14:26.743, 25:02:54.75), about 1′ northeast of the detected maser emission.

Data was reduced using the NRAO AIPS package and normal phase referencing approach that is standard when dealing with VERA dual-beam data (see e.g. Burns et al., 2014; Nakagawa et al., 2016, for details). The final RMS varied between epochs, mainly depending on the static tropospheric error residuals after calibration (see Sect. 3.1), with values between ∼0.1–0.3 Jy for the line-free channels. Maser maps were produced by applying the CLEAN procedure (Högbom, 1974) to emission peaks registered at a signal-to-noise cutoff of 6, with typical beam sizes of 2×1 mas at 22 GHz. Following common nomenclature, a maser 'spot' refers to an individual maser brightness peak imaged in one spectral channel, and a maser 'feature' refers to a group of spots which are considered to relate to the same physical maser cloud, thus a maser feature typically comprises of several maser spots. Maser spots are categorized into features when they are part of the same spectral feature and spatially grouped together (this is sometimes difficult as maser spots often show an elongated distribution, as discussed in Sect 2.3). Wherever possible, we define the nominal astrometric position of a maser feature by determining the flux weighted

average of the brightest three spots in the feature.

As the VLBA maser detections are initial unpublished results, no coordinates are shown. We only discuss the results from the first two epochs for the proper motion analysis in this work (see Fig. 5.1), and we also show an initial annual parallax based on 4 features that could be traced for most of the epochs (see Fig. 5.2). The analysis is still ongoing, but there are a few results that can be already discussed. In the initial proper motion analysis based on the first two epochs 12 maser features could be traced, with an additional 17 and 4 individual features cataloged in epochs I and II respectively. Average astrometric errors were 0.02 mas in right ascension and 0.05 mas in declination. As only the blueshifted outflow could be observed, the systemic source motion could not be calculated and thus the proper motion vectors are the sum of the systemic source motion and the outflow's motion. To circumvent this issue, we tried to derive the proper motion of the outflow by assuming that IRAS 18113–2503 follows the Galactic rotation curve (with which one should be careful for intermediate-mass post-AGBs). From this we can calculate the source motion due to Galactic rotation at the near and far kinematic distances (see Fig. 5.3). Subtracting the calculated motions (black vectors on Fig. 5.1) from the measured maser proper motions, we can estimate the internal motions in the outflow and possibly break the kinematic distance ambiguity. At the far kinematic distance, the residual maser motions (total–systemic) follow the jet axis derived from the VLA observations in Gómez et al. (2011), whereas for the near distance they completely disagree. Thus based on only this information, we can conclude that IRAS 18113–2503 is located around the far kinematic distance.

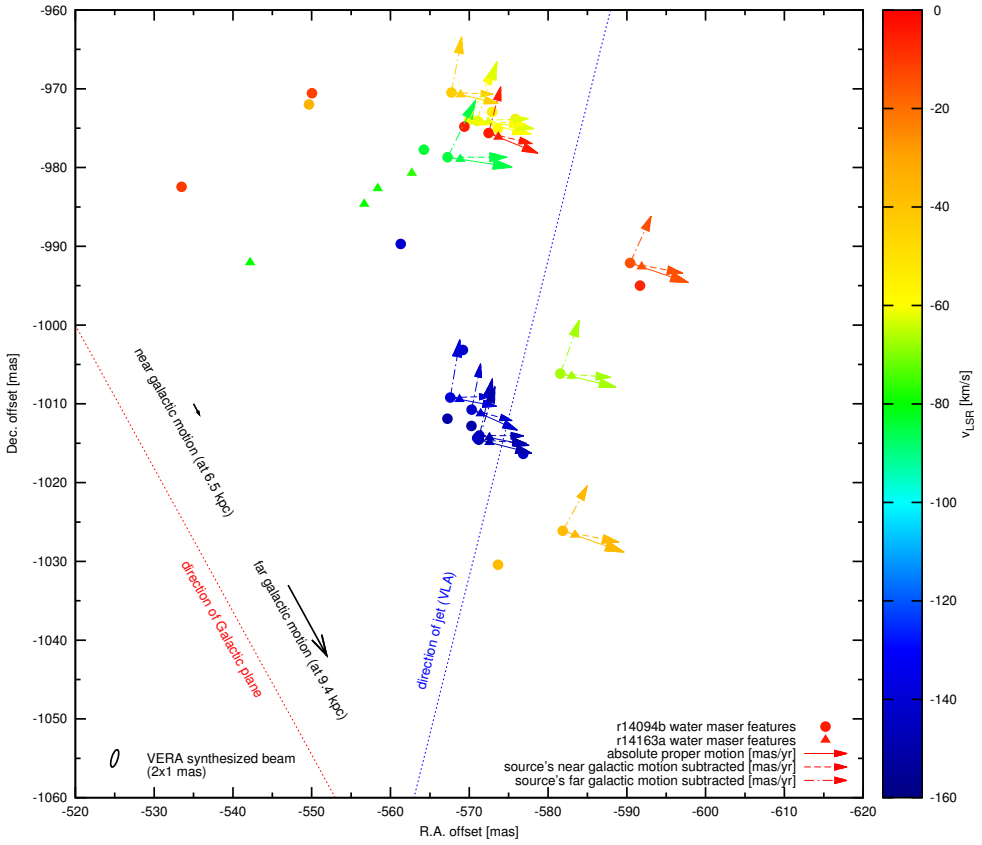

Figure 5.1. Water masers and their motions towards IRAS 18113–2503 in the first two epochs of the VERA monitoring. Solid arrows show the measured proper motions, whereas dashed and dot-dashed arrows show the maser proper motions after the contribution from the Galactic rotation has been subtracted at the near and far kinematic distance, respectively. The jet axis is from Gómez et al. (2011).

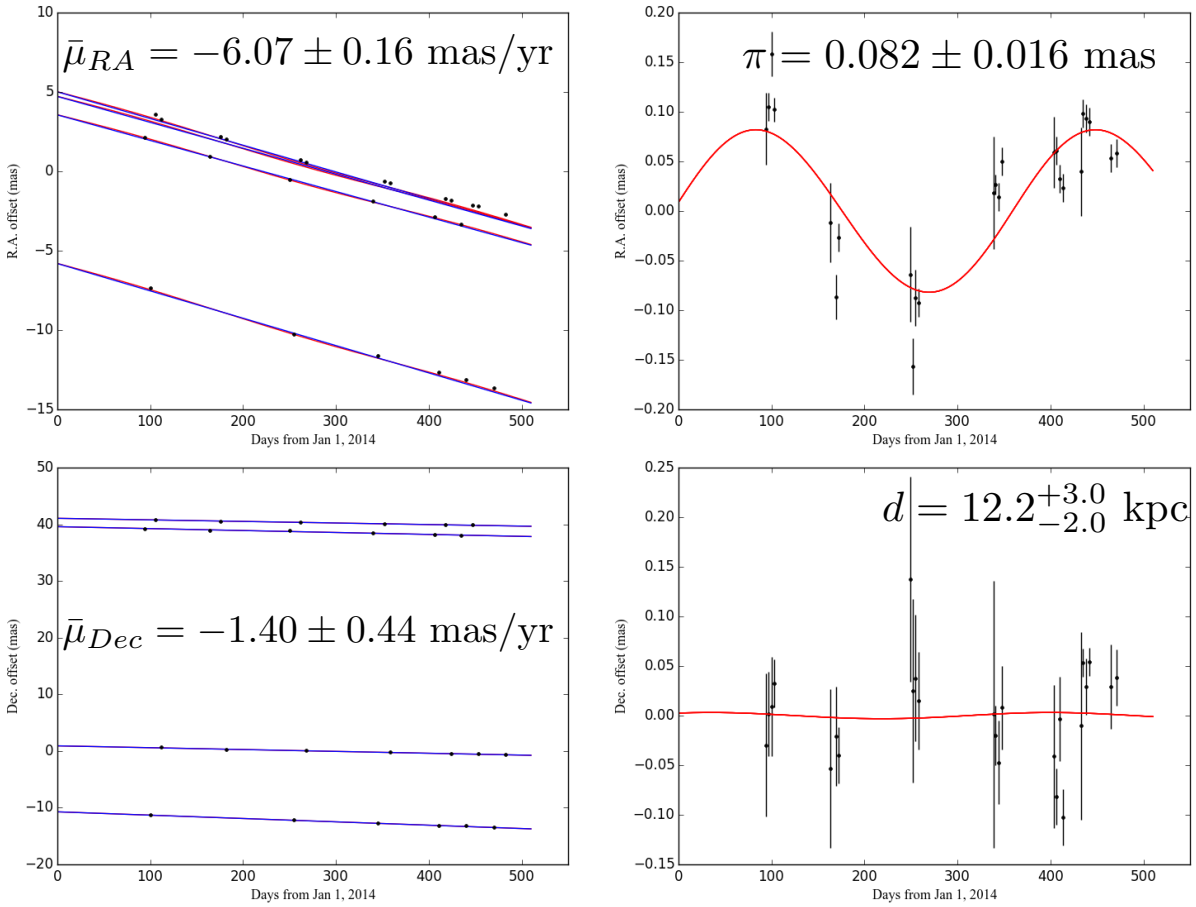

Figure 5.2. Proper motion (left, blue) and annual parallax motion after subtracting the linear proper motions (right, red) of IRAS 18113–2503 H_2O masers, based on four features that could be traced over seven epochs. The zero point on the proper motion plots is arbitrary, whereas the error bars show only the thermal noise errors. The quoted values are initial results only.

An initial annual parallax has also been determined, with the derived values shown on Fig. 5.2. With a trigonometric distance of ~12 kpc, IRAS 18113–2503 is the farthest known water fountain to date and only the third with a measured trigonometric distance after IRAS 19312+1950 (Imai et al., 2011) and IRAS 18286-0959 (Imai et al., 2013b). Based on this distance, IRAS 18113–2503 is located towards and beyond the Galactic Centre in the thick disk at z≈770 pc below the Galactic plane. The parallax is consistent with the far kinematic distance within 2σ.

Using the measured total maser motions (solid arrows) from Fig. 5.1 and subtracting from them the motion caused by Galactic rotation at the measured trigonometric distance, we can estimate the 3D velocities of the H_2O masers in the WF jet. This gives us a velocity range of ~310–430 km s^{-1}, an inclination angle of $\gtrsim$40°, and an outflow kinematic age of ~15 years. The large spread in the calculated 3D velocities favors an episodic mass-loss scenario, however definitive answers on the jet launching and parameters will only come after the full analysis of both the VLBA and VERA data sets.

Without going into more detail, I want to close Sect. 5.1 with an interesting phenomenon involving the flux density variations of the WF H_2O masers. Figure 5.4 shows the variability of the blueshifted outflow's spectrum towards IRAS 18113–2503. The maser components show a rapid variability on monthly scales (left), which is expected behavior of H_2O masers in WF

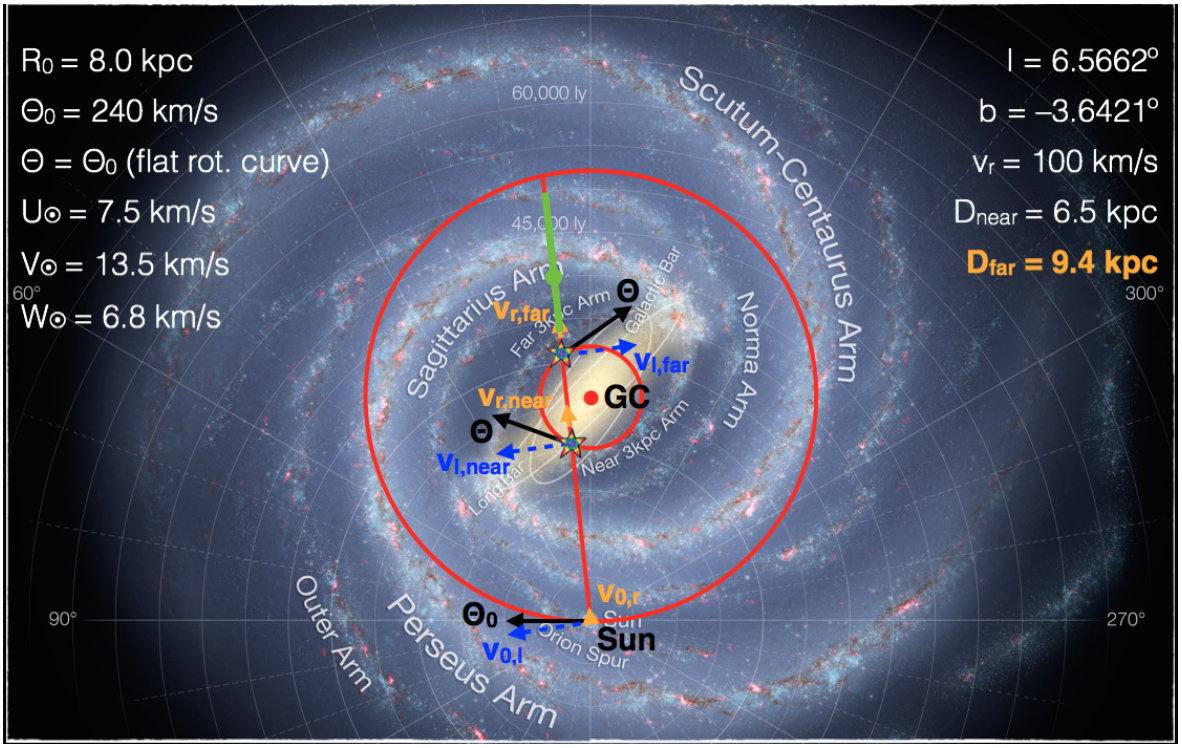

Figure 5.3. Kinematic (orange) vs trigonometric (green) distance of IRAS 18113–2503, with the quoted Galactic parameters from (Francis & Anderson, 2009). Red circles show the circular Galactic orbits and GC marks the Galactic center. The 1σ uncertainty in the trigonometric distance is also shown in green.

jets and makes tracing them difficult, but their integrated maser intensity also varies on a longer scale (right). In order to find out what is happening with the H_2O masers, we started a single-dish monitoring campaign of IRAS 18113–2503. However at the moment, it is still not clear whether this is the fading of the source or a recurring event from, e.g., discontinuous mass loss.

5.2 Astrometry of water masers around IRAS 18043–2116

IRAS 18043–2116, also known as OH 009.1–0.4, was first noted by Sevenster et al. (1997) as a young post-AGB star showing H_2O maser emission in a velocity range over several hundreds of kilometers, far exceeding the range defined by OH maser lines. It was also noted as the only known post-AGB star hosting 1720 MHz OH maser emission, which is thought to arise in shocked regions in the AGB winds (Sevenster & Chapman, 2001). Walsh et al. (2009) later confirmed it as a bona fide WF, by mapping the 22 GHz H_2O maser using ATCA over a velocity range of ~400 km s^{-1}, and finding a bipolar maser distribution with an outflow axis aligned close with the line-of-sight. However, in order to map the structure of the maser region and measure the velocity of the outflow, high-resolution VLBI observations is needed. Such data was taken in 2008–2009 with the VLBA, but never analyzed. The source is also of additional interest, as Tafoya et al. (2014) found using single-dish measurements, that IRAS18043–2116 hosts water masers at 321 GHz. The authors propose that these high-frequency water masers arise in the same regions as their 22 GHz counterpart, and might be indicators of multiple jet launching events. As such, mapping the 22 GHz H_2O maser region is the first step to derive the

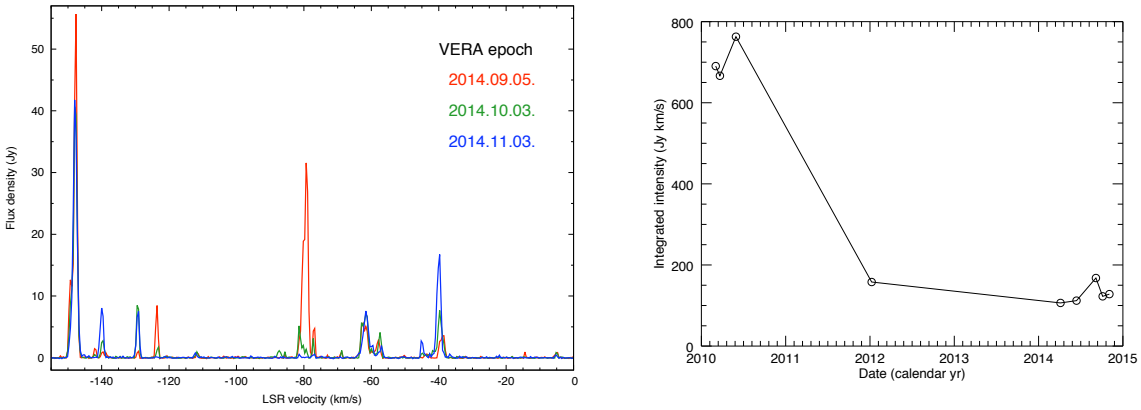

Figure 5.4. *Left:* Spectrum of three consecutive epochs from our VERA parallax measurement of IRAS 18113–2503 (2014 Sept–Nov). Components in the spectrum rapidly change on monthly scales. *Right:* The 5-year long temporal evolution of the integrated H_2O maser intensity in the blueshifted lobe of IRAS 18113–2503. The source is consistently weaker in later epochs. Data is from GBT (Suárez et al., 2009), VLA (Gómez et al., 2011), KVN single dish (Yoon et al., 2014) and VERA, in this order.

jet structure, which can then be compared to future ALMA observations of 321 GHz masers.

High spatial resolution H_2O maser data taken towards the WF IRAS 18113–2503 was retrieved from the NRAO VLBA archive (Project code: BP150). The data included in this work corresponds to the first two epochs of observations (out of a total of six) which were carried out on 2008 October 26 and 2009 January 25 in ∼5 h sessions (with an on-source time of 1 h and sufficient u-v coverage). Left-handed circular polarization signals were recorded with 128 Mbps using 4 contiguous intermediate frequency (IF) bands, each with a bandwidth of 8 MHz. The IFs were separated into 512 channels, which resulted in a spectral resolution of 15.63 kHz (0.21 km s^{-1}) and a velocity coverage from −130 km s^{-1} to 245 km s^{-1} for the 22 GHz H_2O maser source. Besides the target, the calibrator sources of J1755–2232, J1807–2506 and J1924–2914 were also observed every 100 sec, 20 min and 2 h, respectively. The phase tracking center for IRAS 18113–2503 was set to $(\alpha, \delta)_{J2000.0}$=(18:07:20.86, −21:16:10.9), about 1′ North of the detected maser emission.

Data was reduced using the NRAO AIPS package and a standard self-calibration approach. Flux calibration was performed using system temperatures and gain information recorded at each station. J1807–2506 and J1924–2914 were used for determining the group delays and bandpass characteristics. Finally, phase solutions obtained from the reference maser channel were also applied to all other maser channels, achieving an average rms noise value of ∼20 mJy $beam^{-1}$ for both epochs.

Maser maps were produced by applying the CLEAN procedure (Högbom, 1974) to emission peaks registered at a signal-to-noise cutoff of 7, with typical beam sizes of 1.2 × 0.3 mas at P.A.∼346°. Following common nomenclature, a maser ‘spot’ refers to an individual maser brightness peak imaged in one spectral channel, and a maser ‘feature’ refers to a group of spots which are considered to relate to the same physical maser cloud, thus a maser feature typically comprises of several maser spots. Maser spots are categorized into features when they are part of the same spectral feature and spatially are within the $\sim 1\sigma$ error (about 1 mas in our case) of another spot in that feature. Wherever possible, we define the nominal astrometric position of a maser feature by determining the flux weighted average of the brightest three spots in the feature.

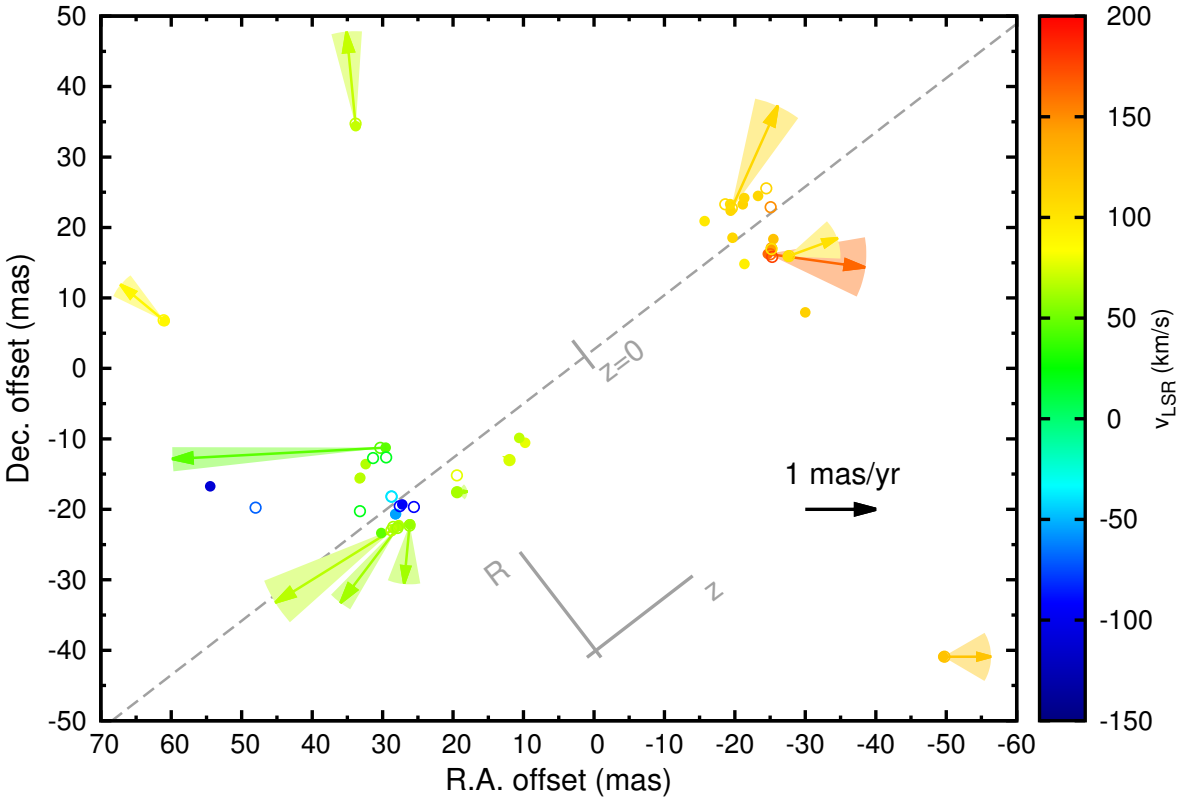

Figure 5.5. Spatial distribution and internal motions of 22 GHz H_2O maser features from VLBA measurements towards IRAS 18113–2503, with the shaded sectors representing the uncertainty in the proper motion measurement. Coordinates are given respective to the centroid of the arc shaped outflows. The dashed line traces the axis of the outflow with PA≈308°, and is used to define the z-R coordinate system. Filled and empty circles indicate the feature locations on October 26, 2008 and January 25, 2009.

As the VLBA maser detections are initial unpublished results, no coordinates are shown. To summarize, 12 maser features could be traced between the two epochs, with an additional ∼20 individual features cataloged at each epoch. Average astrometric errors were 0.02 mas in R.A. and 0.04 mas in Dec. The derived VLBI maser maps are shown in Fig. 5.5. Features can be separated into two distinct arc-shaped groups arising from regions of 30 × 30 mas that are spatially offset along the geometric axis of the system with a P.A.∼308°. They are blue- and redshifted compared to the systemic velocity of the source of V_{LSR}=87 km s^{-1} (Deacon et al., 2004) and most likely trace a bipolar outflow. We also found three compact features that are spatially well removed from the bipolar structure.

In the blueshifted lobe, the masers span velocities from −111 km s^{-1} to 78 km s^{-1}, with the slower masers closer to the source velocity tracing an arc and the faster masers located mainly inside this structure. The redshifted lobe ranges from 94 km s^{-1} to 176 km s^{-1}, tracing a less well defined arc-like structure. Unfortunately at the time of the VLBA observations the true velocity extent of the source was not yet known (published only later in Walsh et al., 2009), so the most redshifted masers above 245 km s^{-1} weren't observed. However, the observations cover partly the velocities of the very bright redshifted cluster seen in the ATCA map around 250 km s^{-1}, but no emission was detected in that region with VLBI.

The two VLBA image cubes were registered together by setting the geometric center of the

maser features found in the outflows and identified in both epochs as a common reference point (Chong et al., 2015). Thus the proper motions are calculated by assuming that the sum of the equally weighted average proper motion vectors in the red- and blueshifted outflows are zero, i.e. the masers trace a symmetric bipolar outflow originating from between the two arc-shaped regions. Astrometric errors are dominated by the thermal noise and are calculated to be $(\sigma_{\Delta\alpha\cos\delta}, \sigma_{\Delta\delta}) \sim (20, 40)$ μas on average, depending on the dynamic range of the maser feature.

Although it is difficult to analyze maser kinematics from only two epochs, we can derive some rough estimates based on the average value of the measured proper motion vectors in the outflows. Based on our previous assumptions, the expansion rate of the outflow is ~1 mas yr^{-1}, the average separation of the two lobes is ~63 mas. From this, the dynamic age of the outflow is estimated to be $t_{\rm jet} \lesssim 30$ yr. Assuming that the source is at the far kinematic distance and taking into account the full velocity spread of the masers seen in our ATCA maps, the inclination angle and one-sided 3D expansion velocities are $i_{\rm jet}$~75 deg and $V_{\rm jet,3D}$~200 km s^{-1}. We note that the inclination angle would increase for a closer distance and that the quoted value is probably a lower estimate. Also $\Delta V_{\rm los} > \Delta V_{\rm sky}$, meaning that the 3D velocities are dominated by the line-of-sight velocities and are not very dependent on the distance. A more detailed astrometric analysis will be possible based on the phase-referenced results of all six available epochs.

Based on the VLBI maser structure and proper motion measurements, we can conclude that the masers trace a high-velocity bipolar outflow that is propagating mainly in the line-of sight direction. The arc-shaped structures in Fig. 5.5 suggest shock fronts from an ejection event, which is consistent with mass-loss scenarios in other water fountain sources (e.g. Boboltz & Marvel, 2007; Day et al., 2010; Chong et al., 2015). In order to gain more insight into the physical nature of the outflow, we compared its maser distribution and proper motions to the models found in the joint papers of Ostriker et al. (2001) and Lee et al. (2001). Their models and simulations were originally constructed to study jet- and wind-driven protostellar outflows and have been applied successfully in several cases to star forming regions (e.g. Sanna et al., 2012; Burns et al., 2016). However, apart from the launching mechanisms and energies involved, evolved stellar environments (and especially water fountain sources) are very similar to star forming regions showing outflows, so the mentioned models can also be fitted to our observations to study the shocked shells at the boundary between the outflowing and ambient material.

Figure 5.6 shows the measured velocity profiles of the relevant masers perpendicular and parallel to the outflow axis. The black lines are the predicted proper motions from a ballistic bow shock model, based on Equations 18–21 in (Ostriker et al., 2001) and adopting the following parameters: the isothermal sound speed c_s=8 km s^{-1} (as in the original paper), the ratio of the velocity of material being ejected from the jet surface to the velocity of the propagating bow shock $\beta c_s/v_s$=0.2 (fitted to our data based on possible values from the original paper), and the radius of the jet R_j=3 mas (measured from Fig. 5.5 as shown by the original paper's Fig. 1). The model predicts the largest spread in proper motions (both transverse and longitudinal) around the head of the jet, along the working surface of the hot shocked material. Opposed to the bow-shock jet model, the grey lines show a wind-driven outflow model, as described in Section 4.3 in Lee et al. (2001), that predicts linearly increasing proper motions along the jet and the largest transverse motions around the middle sections of the jet.

By setting the tip of the bow shock at the maximum maser projection along z, we find that the measured proper motions agree with the ballistic jet model much better than with the wind scenario. The outlier points (mainly in the red-shifted lobe) might be explained by the driving

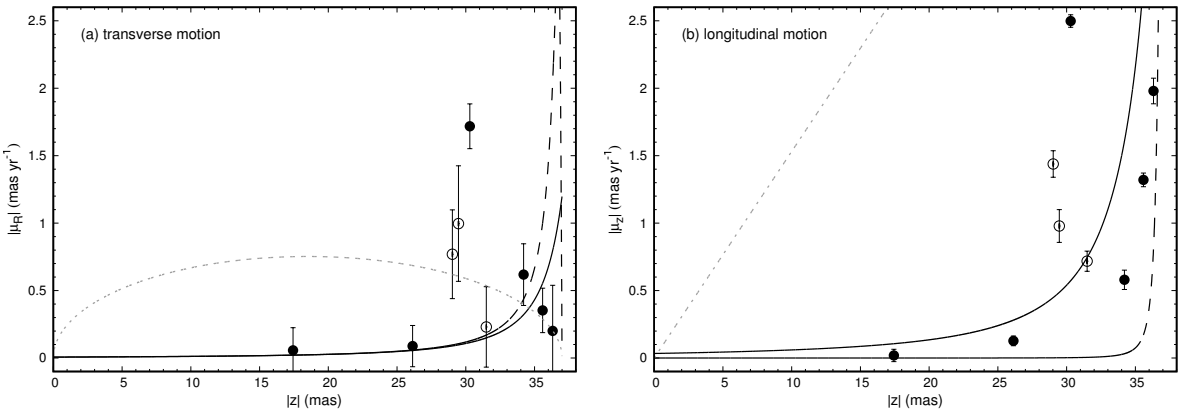

Figure 5.6. Proper motion profiles of the maser features shown in Fig. 5.5, (a) perpendicular and (b) parallel to the outflow axis. Filled and empty circles are masers in the blue- and redshifted lobes, respectively. The origin of the outflow is at z=0. The solid and dashed lines represent the newly swept up material by the propagating jet and the average motion of the jet's outer shell, respectively, as described by the ballistic bow shock model of Ostriker et al. (2001). For comparison, the grey dotted line shows the profile from a momentum-driven shell model (cf. Lee et al., 2001).

source not being halfway between the two masering regions (which is possible due to the incomplete velocity coverage of the observations) and there also might be some errors in maser identification as only 2 epochs were used to measure the proper motions. However, the general agreement means that the masers trace shocked material on the boundary between the high-velocity water fountain jet and the slowly moving circumstellar shell of IRAS 18113–2503. We can also see from Fig. 5.6 that the measured dynamic age of $t_{\rm jet}$=30 yr is an upper limit, as the core jet moves faster than the shocked shell traced by the masers (see also Fig. 1 of Ostriker et al., 2001).

Our bow-shock results support the "cavity model" scenario in water fountains as opposed to the "traditional precessing jet model", where the masers are excited along the enhanced wall of a previously evacuated volume in the circumstellar shell as opposed to an extremely collimated jet precessing about the axis of symmetry and exciting masers at its tip as it drives through the ambient material (see Chong et al., 2015, and references therein). The VLBI results also support the explanations for the observed 321 GHz H_2O masers (Tafoya et al., 2014).

6 | Summary

Astrometry provides the foundation on which many other branches of astronomy are based. In this thesis, I have discussed the importance of maser astrometry in order to derive essential parameters for stellar evolution studies. A special emphasis was put on the technical side of astrometric measurements, as radio astrometry is a technique oriented field relying on skills in VLBI observing and data analysis. The interpretation of the observables are then done by other specialists, but precise observations are always the start of every forward step in science. Models and theories always come and go, but observations, if done right, are for eternity.

As we have seen, astrometry can provide accurate distances to evolved stars, thus helping to derive accurate stellar parameters that can put constraints on evolutionary models. It also provides high-resolution maps of the maser structures found in the circumstellar envelope, tracing various physical phenomena. Masers are superb tracers of these environments, but if we want to use VLBI astrometry to its fullest, it is essential to deal with the technical background precisely. Therefore, the main focus of my thesis was to investigate astrometric techniques at frequencies below 2 GHz, and experiment with 1612 MHz OH maser astrometry to aid studies in stellar evolution, and prepare techniques and ideas for next-generation radio telescopes, such as the SKA. Measurements using H_2O masers were also conducted in an effort to further the study of water fountains.

Four separate experiments were presented in this thesis. The first experiment (Sect. 3.2) focused on developing and demonstrating a new astrometric technique for VLBI, intended for mitigating systematic effects showing a spatial function. It is especially useful for low frequencies (below ~8 GHz) where residual errors from the dispersive ionosphere have been the biggest limitation of accurate astrometry in the past. We saw that our new technique, called MultiView, provided complete ionospheric mitigation regardless of the weather conditions at L-band frequencies. Therefore, MultiView is a crucial step in utilizing radio sources below 2 GHz for high-precision astrometry, by making the results not dominated by systematic errors.

The second experiment (Sect. 4.1) focused on investigating in-beam phase referencing, presently the most widespread VLBI astrometric technique to deal with spatial systematic errors in L-band. A new analysis technique was introduced to identify and study the systematic error residuals in the astrometry. Using this new technique, coupled with in-beam phase referencing, we were able to derive the annual parallax of the long period variable OH/IR star OH138.0+7.2, which at 0.52±0.09 mas is the smallest and most precise OH maser parallax to date. We could also see the effects of other systematic errors in the astrometry, e.g. intrinsic velocity structures in the maser features, which only made it possible to derive a lower limit for the OH maser annual parallax of our other target, the OH/IR star WX Psc. We briefly introduced a possible case study where OH maser astrometry can have a huge impact, that is the study of the period–

luminosity relation and connection of Mira variables and OH/IR stars, and generally very long period AGB variables.

The third and fourth experiment focused on water fountain stars, mapping sources and providing some insight into stellar evolution past the AGB phase, mainly focusing on the possible shaping scenarios of PNe. Experiment three (Sect. 5.1) involved the annual parallax measurement of IRAS 18043–2116 using 22 GHz H_2O maser measurements with VERA, the Japanese VLBI array designed specifically for astrometry at 22 GHz and 43 GHz. This resulted in one of the smallest ever measured Galactic parallaxes at 0.082 ± 0.016 mas, which is near the astrometric limit of present day VLBI arrays and techniques. Experiment four (Sect. 5.2) used archive astrometric data to map and derive the spatio-kinematic structure of another water fountain star, IRAS 18043–2116. An important result was that the observed maser motions in the bipolar high-velocity jets could be explained by a jet-driven ballistic bow shock model developed to explain the jets of young stellar objects. In both water fountains, the observed morphology of the H_2O masers showed bow-shock like structures that can be used to test PNe shaping scenarios.

The results of this PhD thesis – a new observing technique, an OH maser parallax, a H_2O maser parallax and a H_2O maser spatio-kinematic analysis – are only loosely connected, however they all have several implications towards the future. As a next step, it is important to try to use MultiView and derive an OH maser parallax, and in general test the technique in a wide range of possible scenarios, especially where present techniques have failed to provide good astrometry. One possible avenue is to try to adopt the technique for pulsar and other weak continuum astrometric studies, focusing on steep-spectrum sources near the Galactic plane. Another route is to measure a larger number of OH maser parallaxes towards OH/IR stars, hopefully pushing out the parallax distance limit to $\sim$10 kpc in the process. These studies would provide a good synergy with Gaia astrometry and also lay down strong foundations for large-scale SKA projects, e.g. mapping the dynamics of the Milky Way using OH masers. As far as water fountain research is concerned, the next step would be to try and connect the observed high-resolution spatio-kinematic structures of various water fountains, e.g. using the ballistic bow shock model used in the present thesis. It is important to increase the limited number of VLBI measurements and study water fountain sources together, in the framework of other post-AGB stars and PNe.

Bibliography

Alef, W. 1988, in IAU Symposium, Vol. 129, The Impact of VLBI on Astrophysics and Geophysics, ed. M. J. Reid & J. M. Moran, 523

Amiri, N. 2011, PhD Thesis, Leiden University

Andrae, R., Schulze-Hartung, T., & Melchior, P. 2010, ArXiv e-prints

Asaki, Y., Deguchi, S., Imai, H., et al. 2010, ApJ, 721, 267

Asaki, Y., Sudou, H., Kono, Y., et al. 2007, PASJ, 59, 397

Bailer-Jones, C. A. L. 2015, PASP, 127, 994

Balick, B., & Frank, A. 2002, ARA&A, 40, 439

Boboltz, D. A., & Marvel, K. B. 2007, ApJ, 665, 680

Brisken, W. F., Benson, J. M., Beasley, A. J., et al. 2000, ApJ, 541, 959

Brisken, W. F., Benson, J. M., Goss, W. M., & Thorsett, S. E. 2002, ApJ, 571, 906

Bristow, W. A., & Greenwald, R. A. 1997, Journal of Geophysical Research, 102, 11585

Burns, R. A. 2016, PhD Thesis, Kagoshima University

Burns, R. A., Handa, T., Nagayama, T., Sunada, K., & Omodaka, T. 2016, MNRAS, 460, 283

Burns, R. A., Imai, H., Handa, T., et al. 2015, MNRAS, 453, 3163

Burns, R. A., Yamaguchi, Y., Handa, T., et al. 2014, PASJ, 66, 102

Chatterjee, S., Cordes, J. M., Lazio, T. J. W., et al. 2001, ApJ, 550, 287

Chatterjee, S., Brisken, W. F., Vlemmings, W. H. T., et al. 2009, ApJ, 698, 250

Cheng, J. 2009, The Principles of Astronomical Telescope Design, New York:Springer, ISBN 9780387887913 (Springer)

Chibueze, J. O., Miyahara, T., Omodaka, T., et al. 2016, ApJ, 817, 115

Chong, S.-N., Imai, H., & Diamond, P. J. 2015, ApJ, 805, 53

Clayton, G. C., Wolff, M. J., Sofia, U. J., Gordon, K. D., & Misselt, K. A. 2003, ApJ, 588, 871

Cotton, W. D. 1995, in Astronomical Society of the Pacific Conference Series, Vol. 82, Very Long Baseline Interferometry and the VLBA, ed. J. A. Zensus, P. J. Diamond, & P. J. Napier, 189

Day, F. M., Pihlström, Y. M., Claussen, M. J., & Sahai, R. 2010, ApJ, 713, 986

Deacon, R. M., Chapman, J. M., & Green, A. J. 2004, ApJS, 155, 595

Deller, A. T., Boyles, J., Lorimer, D. R., et al. 2013, ApJ, 770, 145

Deller, A. T., Tingay, S. J., Bailes, M., & West, C. 2007, PASP, 119, 318

Deller, A. T., Brisken, W. F., Phillips, C. J., et al. 2011, PASP, 123, 275

Deller, A. T., Vigeland, S. J., Kaplan, D. L., et al. 2016, ApJ, 828, 8

Dodson, R., Rioja, M., Asaki, Y., et al. 2013, AJ, 145, 147

Dodson, R., Rioja, M. J., Molina, S. N., & Gómez, J. L. 2017, ApJ, 834, 177

Doi, A., Fujisawa, K., Habe, A., et al. 2006, PASJ, 58, 777

Elitzur, M. 1992, Astrophysics and Space Science Library, Vol. 170, Astronomical masers, Dordrecht:Kluwer Academic Publishers, ISBN 0792312171, ed. M. Elitzur

Elitzur, M., & Ivezić, Ž. 2001, MNRAS, 327, 403

Engels, D., & Bunzel, F. 2015, A&A, 582, A68

Engels, D., Etoka, S., Gérard, E., & Richards, A. 2015, in , 473

Epchtein, N., Guibert, J., Nguyen-Quang-Rieu, Turon, P., & Wamsteker, W. 1980, A&A, 85, L1

Etoka, S., & Diamond, P. J. 2010, MNRAS, 406, 2218

Etoka, S., Engels, D., Gerard, E., & Richards, A. M. S. 2014, in Proceedings of the 12th European VLBI Network Symposium and Users Meeting (EVN 2014), id.59, 59

Etoka, S., & Le Squeren, A. M. 2000, A&AS, 146, 179

Feast, M. W. 2013, Galactic Distance Scales, ed. T. D. Oswalt & G. Gilmore, 829

Fey, A. L., Gordon, D., Jacobs, C. S., et al. 2015, AJ, 150, 58

Fomalont, E. B., Goss, W. M., Beasley, A. J., & Chatterjee, S. 1999, AJ, 117, 3025

Fomalont, E. B., & Kopeikin, S. 2002, in Proceedings of the 6th EVN Symposium, ed. E. Ros, R. W. Porcas, A. P. Lobanov, & J. A. Zensus, 53

Francis, C., & Anderson, E. 2009, New Astronomy, 14, 615

Godfrey, L., Bignall, H., & Tingay, S. 2011, Very High Angular Resolution Science with the SKA, Tech. rep., Curtain University, Australia

Goldman, S. R., van Loon, J. T., Zijlstra, A. A., et al. 2017, MNRAS, 465, 403

Gómez, J. F., Rizzo, J. R., Suárez, O., et al. 2011, ApJL, 739, L14

Gray, M. 2012, Maser sources in Astrophysics, UK:Cambridge University Press, ISBN 9780521879804

Green, J., Van Langevelde, H. J., Brunthaler, A., et al. 2015, Advancing Astrophysics with the Square Kilometre Array (AASKA14), 119

Greisen, E. W. 2003, Information Handling in Astronomy - Historical Vistas, 285, 109

Habing, H. J. 1996, The Astronomy and Astrophysics Review, 7, 97

Herman, J., & Habing, H. J. 1985, Physics Report, 124, 257

Ho, C. M., Wilson, B. D., Mannucci, A. J., Lindqwister, U. J., & Yuan, D. N. 1997, Radio Science, 32, 1499

Högbom, J. A. 1974, A&AS, 15, 417

Honma, M., Tamura, Y., & Reid, M. J. 2008a, PASJ, 60, 951

Honma, M., Kijima, M., Suda, H., et al. 2008b, PASJ, 60, 935

Honma, M., Nagayama, T., Ando, K., et al. 2012, PASJ, 64, 136

Hu, J. Y., Slijkhuis, S., de Jong, T., & Jiang, B. W. 1993, A&AS, 100, 413

Imai, H., Burns, R. A., Yamada, Y., et al. 2016, ArXiv e-prints

Imai, H., Deguchi, S., Nakashima, J.-i., Kwok, S., & Diamond, P. J. 2013a, ApJ, 773, 182

Imai, H., Deguchi, S., & Sasao, T. 2002, ApJ, 567, 971

Imai, H., Kurayama, T., Honma, M., & Miyaji, T. 2013b, PASJ, 65, 28

Imai, H., Sakai, N., Nakanishi, H., et al. 2012, PASJ, 64, 142

Imai, H., Tafoya, D., Honma, M., Hirota, T., & Miyaji, T. 2011, PASJ, 63, 81

Ishihara, D., Onaka, T., Kataza, H., et al. 2010, A&A, 514, A1

Ita, Y., & Matsunaga, N. 2011, MNRAS, 412, 2345

Ita, Y., Tanabé, T., Matsunaga, N., et al. 2004, MNRAS, 353, 705

Jimenez-Monferrer, S., Rioja, M. J., Dodson, R., Smirnov, O., & Guirado, J. C. 2010, in 10th European VLBI Network Symposium and EVN Users Meeting, Vol. 125, 84

Johnson, H. L. 1966, ARA&A, 4, 193

Kaplan, G. H. 1998, AJ, 115, 361

Karakas, A. I. 2010, MNRAS, 403, 1413

Keimpema, A., Kettenis, M. M., Pogrebenko, S. V., et al. 2015, Experimental Astronomy, 39, 259

Kirsten, F., Vlemmings, W., Campbell, R. M., Kramer, M., & Chatterjee, S. 2015, A&A, 577, A111

Kohoutek, L. 2001, A&A, 378, 843

Kovalevsky, J., & Seidelmann, P. K. 2004, Fundamentals of Astrometry, UK:Cambridge University Press, 1st edition, ISBN 0521642167

Krishnan, V., Ellingsen, S. P., Reid, M. J., et al. 2015, ApJ, 805, 129

Lee, C.-F., Stone, J. M., Ostriker, E. C., & Mundy, L. G. 2001, ApJ, 557, 429

Lindegren, L., Lammers, U., Bastian, U., et al. 2016, A&A, 595, A4

Linfield, R. P. 1986, AJ, 92, 213

Lonsdale, C. 2004, in LFD Memo, 015

Marigo, P., Bressan, A., Nanni, A., Girardi, L., & Pumo, M. L. 2013, MNRAS, 434, 488

Marigo, P., Girardi, L., Bressan, A., et al. 2017, ApJ, 835, 77

Mathis, J. S., Rumpl, W., & Nordsieck, K. H. 1977, ApJ, 217, 425

Middelberg, E., Deller, A. T., Norris, R. P., et al. 2013, A&A, 551, A97

Min, C., Matsumoto, N., Kim, M. K., et al. 2014, PASJ, 66, 38

Murakami, H., Baba, H., Barthel, P., et al. 2007, PASJ, 59, S369

Nakagawa, A., Kurayama, T., Matsui, M., et al. 2016, PASJ, 68, 78

Nakagawa, A., Omodaka, T., Handa, T., et al. 2014, PASJ, 66, 101

Neugebauer, G., Habing, H. J., van Duinen, R., et al. 1984, ApJL, 278, L1

Ochsenbein, F., Bauer, P., & Marcout, J. 2000, A&AS, 143, 23

Orosz, G., Rioja, M. J., Dodson, R., Imai, H., & Frey, S. 2017a, Proceedings of the 13th EVN Symposium, in press

Orosz, G., Imai, H., Dodson, R., et al. 2017b, AJ, accepted, arXiv:1701.05101

Ossenkopf, V., Henning, T., & Mathis, J. S. 1992, A&A, 261, 567

Ostriker, E. C., Lee, C.-F., Stone, J. M., & Mundy, L. G. 2001, ApJ, 557, 443

Paragi, Z., Godfrey, L., Reynolds, C., et al. 2015, Advancing Astrophysics with the Square Kilometre Array (AASKA14), 143

Peterson, W. M., Mutel, R. L., Lestrade, J.-F., Güdel, M., & Goss, W. M. 2011, ApJ, 737, 104

Petrov, L., & Kovalev, Y. Y. 2016, MNRAS, accepted, arXiv: 1611.02630

Porcas, R. W. 2009, A&A, 505, L1

Porcas, R. W., & Rioja, M. J. 2002, in Proceedings of the 6th EVN Symposium, ed. E. Ros, R. W. Porcas, A. P. Lobanov, & J. A. Zensus, 65

Porcas, R. W., Rioja, M. J., Machalski, J., & Hirabayashi, H. 2000, in Astrophysical Phenomena Revealed by Space VLBI, ed. H. Hirabayashi, P. G. Edwards, & D. W. Murphy, 245–252

Preite-Martinez, A. 1988, A&AS, 76, 317

Qiao, H.-H., Walsh, A. J., Green, J. A., et al. 2016, ApJS, 227, 26

Ramstedt, S., Schöier, F. L., Olofsson, H., & Lundgren, A. A. 2008, A&A, 487, 645

Reid, M. J., & Brunthaler, A. 2004, ApJ, 616, 872

Reid, M. J., Dame, T. M., Menten, K. M., & Brunthaler, A. 2016, ApJ, 823, 77

Reid, M. J., & Honma, M. 2014, ARAA, 52, 339

Reid, M. J., Menten, K. M., Brunthaler, A., et al. 2009, ApJ, 693, 397

Reid, M. J., Readhead, A. C. S., Vermeulen, R. C., & Treuhaft, R. N. 1999, ApJ, 524, 816

Reid, M. J., Menten, K. M., Brunthaler, A., et al. 2014, ApJ, 783, 130

Richards, A. M. S. 2012, in Cosmic Masers - from OH to H0

Richards, A. M. S., Etoka, S., Gray, M. D., et al. 2012, A&A

Rieke, G. H., & Lebofsky, M. J. 1985, ApJ, 288, 618

Rioja, M., & Dodson, R. 2011, AJ, 141, 114

Rioja, M., Dodson, R., Porcas, R. W., et al. 2009, in 8th International e-VLBI Workshop, 14

Rioja, M. J., Dodson, R., Orosz, G., Imai, H., & Frey, S. 2017, AJ, 153, 105

Rioja, M. J., Porcas, R. W., Desmurs, J.-F., et al. 2002, in Proceedings of the 6th EVN Symposium, ed. E. Ros, R. W. Porcas, A. P. Lobanov, & J. A. Zensus, 57

Rioja, M. J., Stevens, E., Gurvits, L., et al. 1997, Vistas in Astronomy, 41, 213

Sanna, A., Reid, M. J., Carrasco-González, C., et al. 2012, ApJ, 745, 191

Sekido, M., & Fukushima, T. 2006, Journal of Geodesy, 80, 137

Sevenster, M. N., & Chapman, J. M. 2001, ApJL, 546, L119

Sevenster, M. N., Chapman, J. M., Habing, H. J., Killeen, N. E. B., & Lindqvist, M. 1997, A&AS, 122

Shepherd, M. C. 1997, in Astronomical Society of the Pacific Conference Series, Vol. 125, Astronomical Data Analysis Software and Systems VI, ed. G. Hunt & H. Payne, 77

Shintani, M., Imai, H., Ando, K., et al. 2008, PASJ, 60, 1077

Skrutskie, M. F., Cutri, R. M., Stiening, R., et al. 2006, AJ, 131, 1163

Sloan, G. C., Matsuura, M., Lagadec, E., et al. 2012, ApJ, 752, 140

Suárez, O., Gómez, J. F., Miranda, L. F., et al. 2009, A&A, 505, 217

Szczerba, R., Siódmiak, N., Stasińska, G., & Borkowski, J. 2007, A&A, 469, 799

Tafoya, D., Franco-Hernández, R., Vlemmings, W. H. T., Pérez-Sánchez, A. F., & Garay, G. 2014, A&A, 562, L9

Tafoya, D., Imai, H., Gomez, Y., et al. 2011, PASJ, 63, 71

Thompson, A. R., Moran, J. M., & Swenson, Jr., G. W. 2004, Interferometry and Synthesis in Radio Astronomy, New York:Wiley, 2nd edition, ISBN 0471254924

van Langevelde, H. J., van der Heiden, R., & van Schooneveld, C. 1990, A&A, 239, 193

van Langevelde, H. J., Vlemmings, W., Diamond, P. J., Baudry, A., & Beasley, A. J. 2000, A&A, 357, 945

van Loon, J. T. 2000, A&A, 354, 125

Vlemmings, W. H. T., & van Langevelde, H. J. 2007, A&A, 472, 547

Vlemmings, W. H. T., van Langevelde, H. J., Diamond, P. J., Habing, H. J., & Schilizzi, R. T. 2003, A&A, 407, 213

Walsh, A. J., Breen, S. L., Bains, I., & Vlemmings, W. H. T. 2009, MNRAS, 394, L70

Wenger, M., Ochsenbein, F., Egret, D., et al. 2000, A&AS, 143, 9

Whitelock, P. A. 2012, Ap&SS, 341, 123

Whitelock, P. A., Feast, M. W., & van Leeuwen, F. 2008, MNRAS, 386, 313

Whitney, A. R. 2000, in IVS 2000 General Meeting Proceedings, ed. F. Takahashi, 187–205

Whittet, D. C. B. 2003, Dust in the Galactic Environment, Bristol:IOP Publishing Ltd, 2nd edition, ISBN 0750306246

Wilson, T. L., Rohlfs, K., & Hüttemeister, S. 2009, Tools of Radio Astronomy, Berlin:Springer-Verlag, 5th edition, ISBN 9783540851219 (Springer-Verlag)

Wood, P. R. 2000, PASA, 17, 18

Wright, E. L., Eisenhardt, P. R. M., Mainzer, A. K., et al. 2010, AJ, 140, 1868

Wright, M. 2001, PhD Thesis, University of Bristol

Wrobel, J., Walker, R., Benson, J., & A.., B. 2000, VLBA Scientific Memorandum n. 24: Strategies for Phase Referencing with the VLBA, Tech. rep., NRAO

Yamashita, S. 2016, MSc Thesis, Kagoshima University (in Japanese)

Yoon, D.-H., Cho, S.-H., Kim, J., Yun, Y. j., & Park, Y.-S. 2014, ApJS, 211, 15

Yung, B. H. K., Nakashima, J.-i., Hsia, C.-H., & Imai, H. 2017, MNRAS, 465, 4482

Yung, B. H. K., Nakashima, J.-i., Imai, H., et al. 2011, ApJ, 741, 94

Publications

Refereed publications

Related to PhD thesis: [1] [2]

1. **Orosz, G.**, Imai, H., Dodson, R., Rioja, M. J., Frey, S., Burns, R. A., Etoka, S., Nakagawa, A., Nakanishi, H., Asaki, Y., Goldman, S., & Tafoya, D.
Astrometry of OH/IR stars using 1612 MHz hydroxyl masers. I. Annual parallaxes of WX Psc and OH138.0+7.2
2017, AJ, in press, arXiv:1701.05101

2. Rioja, M. J., Dodson, R., **Orosz, G.**, Imai, H., & Frey, S.
MultiView high precision VLBI astrometry at low frequencies
2017, AJ, 153, 105

3. **Orosz, G.**, & Frey, S.
Optical–radio positional offsets for active galactic nuclei
2013, A&A, 553, A13

4. Braunmuller, P., & **Orosz, G.**
The basis of synthetic aperture radar interferometry in Hungary
2013, Geocarto International 28, 37

Conference proceedings and other printed publications

Related to PhD thesis: [1] [3]

1. **Orosz, G.**, Rioja, M. J., Dodson, R., Imai, H., & Frey, S.
MultiView phase corrections at low frequencies for precise astrometry
2017, Proc. of 13th EVN Symp., in press

2. Oyadomari, M., Imai, H., Cho, S-H., Asaki, Y., Choi, Y-K., Kim, J., Yun, Y.,Matsumoto, N., Min, C-H., Oyama, T., Yoon, S-C., Yoon, D-H., Kim, D-J., Dodson, R., Rioja, M.J., Burns, R.A., **Orosz, G.**, Nakagawa, A., Chibueze J.O., Nakashima, J., & Sobolev, A.
KaVA ESTEMA project
2016, JPCS, 728, 072006

3. Imai, H., Burns, R. A., Yamada, Y., Goda, N., Yano, T., **Orosz, G.**, Niinuma, K., & Bekki, K.
Radio Astrometry towards the Nearby Universe with the SKA
2016, eprint, arXiv:1603.02042

4. **Orosz, G.**, & Frey, S.
Radio-optical outlier quasars – a case study with ICRF2 and SDSS
2012, MmSAI 83, 990

Papers in preparation

Related to PhD thesis: [1] [2] [3]

1. **Orosz, G.**, Imai, H., Gomez, J. F., Suarez, O., Rizzo, J. R., Nakagawa, A., & Burns, R. A.
Trigonometric distance of the fastest water fountain source IRAS 18113–2503
PASJ, in prep.

2. **Orosz, G.**, Tafoya, D., Imai, H., & Burns, R. A.
Maser kinematics of IRAS 18043–2116: bow shocks in a water fountain jet
MNRAS, in prep.

3. **Orosz, G.**, Imai, H., Nakagawa, A., Engels, D., Etoka, S., Goldman, S., Nanni, A., Marigo, P., Tafoya, D., Dodson, R., Rioja, M. J., Frey, S., Burns, R. A., Nakanishi, H., & Asaki, Y.
Astrometry of OH/IR stars using 1612 MHz hydroxyl masers. II. Probing stellar evolution and Galactic dynamics
ApJ, in prep.